The catchment area of groomed jets at NNLL

Aditya Pathak

School of Physics and Astronomy, University of Manchester,
Manchester, M13 9PL, United Kingdom
Deutsches Elektronen-Synchrotron DESY,
Notkestr. 85, 22607 Hamburg, Germany

E-mail: aditya.pathak@desy.de

ABSTRACT: Groomed jet observables have a dynamical catchment area which plays a key role in determining the leading nonperturbative power corrections and the impact of the underlying event. Based on field-theoretic arguments, certain moments of the groomed jet radius R_g capture the entirety of the kinematic and grooming parameter dependence of these effects. These moments can be computed perturbatively in the soft drop operator expansion region where these corrections are small, but yet significant to be relevant for precision physics. A precise determination of these moments is thus crucial to faithfully isolate the universal contributions of hadronization and the underlying event. Building on a previously developed effective field theory framework for the doubly differential soft drop groomed jet mass and groomed jet radius measurement, we present here a calculation of these moments at next-to-next-to-leading-logarithmic (NNLL) accuracy including matching into the plain jet mass region. We compare our predictions for these moments against parton-shower Monte Carlo simulations and find good agreement. These results have applications for precision physics with soft drop jet mass such as determination of the strong coupling constant and the top quark mass and for improving hadronization models.

Contents

1   Introduction

The nonperturbative effects of quantum chromodynamics (QCD) encompass a wide array of rich phenomena ranging from low energy nuclear physics, the spectrum of hadrons, the structure of energetic protons described by parton densities, the physics of hadronization, the formation and evolution of the quark gluon plasma, and much more, each contributing to the richness of the QCD phase-diagram. These nonperturbative effects can be probed in different experimental setups and studied via an appropriate effective field theory of QCD. Among these, the physics of hadronization is one such complex phenomenon that has so far remained largely elusive to first principle calculations. Studies of jets and jet substructure in high energy collisions have offered us invaluable insights about hadronization. On the other hand, jets are also unique tools that allow us to probe fundamental aspects of QCD and in searching for physics beyond the Standard Model [1, 2]. Hadronization impacts measurements of jet substructure observables relative to a reference parton level computation in a way that is partly unique to the observable and partly universal [3–9]. Because the effects of hadronization cannot be predicted from first principle calculations, the effort has been to seek ways to eliminate or minimize hadronization corrections, such that perturbative calculations can be reliably compared to collider data.

Typically, the dominant effects of hadronization arise in the soft wide angle physics, which is challenging to bring under theoretical control even in perturbation theory. Moreover, at the Large Hadron Collider (LHC), the underlying event and pile-up also make a contribution of similar nature. With the introduction of grooming algorithms [10–17] it has been possible to make first principle predictions for jet substructure observables at the LHC due to their effectiveness in removing soft wide angle contamination in the complex LHC environment and thus suppressing hadronization, underlying event and pile-up effects. These grooming techniques were initially designed as a taggers to suppress effects of QCD in searches of multiprong decays originating from electroweak and potentially new physics, but over the recent years they have come to be seen as tools with strong potential for applications in precision physics.[1]

Among various variants, the soft drop (SD) groomer [14] (including the modified Mass Drop Tagger [13, 15] as a special case), has been extensively studied and all-orders factorization formulae have been established [24–26]. Among an impressive list of phenomenological applications, examples of application of soft drop grooming include measurement of the QCD splitting functions [27, 28], study of fragmentation structure [29, 30], isolation of the soft-sensitive dynamics [31–33], and quantification of medium modifications [34–38]. The algorithm of jet grooming is intimately tied to sequential recombination jet algorithms that pair-wise cluster particles/subjets into subjets, to eventually form a jet. The criteria for soft drop is given by a sequential test between pairs of subjets i and j found by de-clustering a Cambridge-Achen clustered tree (based solely on angular separation) of particles in a jet:

$$\frac{\min(p_{T_i}, p_{T_j})}{p_{T_i} + p_{T_j}} > z_{\text{cut}} \left(\frac{\Delta R_{ij}}{R_0}\right)^{\beta}. \tag{1.1}$$

If the pair collectively fails this criteria then the softer of the two (say i with $p_{T_i} < p_{T_j}$) is removed and the next pair obtained by de-clustering the harder subjet (j) is tested for this condition. The pair that eventually satisfies this condition terminates the groomer, and the remaining particles in either of the subjets in the pair constitute the groomed jet. The parameters z_{cut} and β control the strength of the groomer and are typically chosen to be $z_{\text{cut}} \sim 0.1$ and $\beta \sim 1$. The careful formulation of the soft drop condition in eq. (1.1) ensures that IRC-safe observables measured on jets remain calculable in perturbation theory even after grooming.

A classic observable studied extensively at the LHC is the jet mass. For instance, both ungroomed and groomed jet substructure measurements have been measured by ALICE [39], ATLAS [40–44], and CMS [45–48] collaborations. The groomed jet angularities (a generalization of the jet mass) and other groomed jet substructure observables have also recently been measured by the ALICE [49], CMS [46, 50] and ATLAS [51] collaborations. Soft drop jet mass has been explored for applications such as precision top quark mass [26, 52, 53] and strong coupling constant [54, 55] measurements. State-of-the-art perturbative calculations for soft drop jet mass have reached high accuracy of next-to-next-to-next-to-leading logarithmic accuracy (N³LL) matched to next-to-next-to-leading order (NNLO)

---

[1]Somewhat recently, there has also been a lot of exciting progress in developing a completely complementary approach of employing energy-energy correlators (EEC) for precision collider physics [18–23].

predictions for groomed jets in the $e^+e^- \to q\bar{q}$ process [56], and next-to-next-to-leading-logarithmic (NNLL) accuracy [24, 55] for jets at the LHC.

To make these calculations useful for precision phenomenology, it is crucial to describe nonperturbative power corrections in the jet mass spectrum. In the region where soft drop is effective in removing soft-wide angle radiation and where perturbation theory is dominant, the nonperturbative power corrections can be as large as $\sim 10\%$. As was shown in a recent analysis in ref. [55], these power corrections thus start to become relevant already at NNLL accuracy. For instance, we showed in ref. [55] that the unconstrained effects of hadronization respectively contribute about 3% and 8% irreducible uncertainty for quark and gluon jets groomed with $z_{\rm cut} = 0.1$ and $\beta = 1$. Understanding these effects is also crucial for top quark mass determination using soft drop jet mass — in ref. [26], leveraging on the resilience of soft drop against underlying event, soft drop jet mass was proposed as a candidate for precision top mass measurement, and followed up by a MC top mass calibration in `Pythia8+Powheg` by the ATLAS collaboration [53]. By directly comparing the theory prediction against the unfolded LHC data, a determination of the top quark mass in a short distance scheme can be envisaged. However, the peak of the distribution where the dominant sensitivity to the top mass lies, receives significant hadronization corrections which are important to account for in order to formulate a consistent hadron level prediction.

One of the most common method to account for non-perturbative (NP) corrections is to use hadronization models, such as those provided with event generators such as `Pythia` [57], `Sherpa` [58], and `Herwig` [59], see for example ref. [60]. These hadronization models are extremely useful tools in guiding our intuition and allow us to study nonperturbative effects on any arbitrarily complicated observable. In a more recent work in ref. [61], this approach was employed to delve deeper into the interaction between parton showers and hadronization corrections, and account for the impact of event migration across $p_{T,\rm jet}$ bins resulting from hadronization and underlying event. However, it is crucial to note that these models are designed to be compatible with the respective parton showers that are less precise than the aforementioned analytical calculations at NNLL and beyond, and hence are not ideal for describing NP power corrections in high precision analytical calculations. Moreover, the parameters of event generators are tuned to a broad range of measurements that are distinct from the target observables, thereby claiming universality. However, understanding the underlying physics described by these models from a field theory perspective remains challenging. Due to the intricate nature of these models, which offer multiple adjustable parameters, it is unclear how to associate an intrinsic uncertainty with their predictions.

Another approach utilized to incorporate nonperturbative corrections involves the application of an analytical model for hadronization [8, 13, 54, 62]. This model is based on the dispersive representation of the strong coupling constant [63], allowing for efficient analysis of power corrections in a wide range of observables using Feynman diagrams with 'probe nonperturbative gluons'. The dispersive approach has established a systematic framework for investigating power corrections, addressing various limitations encountered with hadronization models in precision phenomenology. In a first approximation, a single probe gluon is often sufficient to capture the broad-scale kinematic features of the power corrections. For non-inclusive observables like the jet mass, where the computation of power

corrections may differ depending on whether one or multiple probe gluons are considered, the introduction of the 'Milan factor' [64, 65] allows for universality features within this approach to be preserved. The Milan factor has been computed for a wide range of e^+e^--event shapes, and studies in refs. [66, 67] have explored the variations in the correction factor arising from different jet clustering procedures. Finally, in ref. [68] has shown how naive estimates within the dispersive framework can be further corrected to account for hadron mass effects. To additionally account for underlying event effects, extensions have been made to this model in refs. [8, 62].

However, it is important to note that the dispersive model assumes that the effective coupling constant $\alpha_{\text{eff}}(\mu^2)/\pi$, when extrapolated into the nonperturbative regime, remains numerically small and that higher-order effects in powers of the effective coupling do not significantly alter the estimation of power corrections. Despite the considerable phenomenological success of the dispersive approach, a rigorous proof of the universality of the infrared coupling constant and its smallness for an expansion in the number of probe gluons is still lacking, and hence the approach fundamentally relies on a model. To enhance the robustness and reliability of the dispersive approach, it is important to thoroughly investigate the behavior of the effective coupling constant in the nonperturbative regime. Such a positive proof would allow the results obtained within this framework to be regarded as entirely model-independent, providing more confidence in their interpretation and applicability to high-precision phenomenology.

1.1 A field-theoretic formalism for nonperturbative corrections

For precision studies we need a first principles, field-theoretic paradigm for describing these nonperturbative power corrections [3–7, 9] that can be systematically improved and can be combined with perturbative calculations independent of their accuracy, beyond those achievable with parton showers. This has been made possible thanks to rigorous QCD factorization theorems [69–73], combined with the powerful machinery of soft-collinear effective field theory (SCET) [74–78]. These methods have enabled a field theoretically consistent study of NP power corrections. Although this approach cannot be applied generally to any arbitrary observable, by systematically analyzing a variety of jet substructure observables and event shapes, we have been able to draw universal and model-independent conclusions about the precise way in which NP corrections enter in these observables. By exploiting the universal properties of soft QCD, this approach allows us to identify the kinematic dependence of these NP corrections in a variety of jet observables, allowing them to be parameterized in terms of a few (a lot fewer than parameters in a hadronization model), universal $\mathcal{O}(\Lambda_{\text{QCD}})$ constants. For example, an analysis along these lines reveals that nonperturbative corrections to the jet mass and jet p_T take the following form [8, 9],

$$\delta m_J^2 = p_T(R\,\Omega_\kappa^{(1)} + R^3\Omega_\kappa^{(3)} + \dots)\,, \qquad \delta p_T = \frac{1}{R}\Upsilon_\kappa^{(-1)} + R\Upsilon_\kappa^{(1)} + \dots. \qquad (1.2)$$

Here $\Omega_\kappa^{(i)}$ and $\Upsilon_\kappa^{(i)}$ are unknown $\mathcal{O}(\Lambda_{\text{QCD}})$ parameters which only depend on the flavor $\kappa = q, g$ of the parton initiating the jet, and R is the jet radius. The specific scaling of these corrections with p_T and the dependence on the jet radius is a model-independent statement

that can be derived on general arguments of factorization of the soft physics. Here the leading terms with the smallest power of R correspond to the leading hadronization effect in each of these cases. The subleading terms (including ones not shown in eq. (1.2)) arise due to contributions from the initial state radiation (ISR) and the underlying event. Although not obtainable from a first-principle calculations, these nonperturbative parameters can be determined by making a comparison with experimental data.[2] These field theory predictions also clearly demarcate the kinematic region of validity of the proposed NP corrections as well as allow for precisely estimating the associated theory uncertainty (for example in terms of the size of higher order power corrections) and the experimental uncertainty (related to the statistics and the fitting procedure). This approach was pursued in determination of the strong coupling constant from the LEP data in refs. [79–81].

In this paper we focus on a factorization-based approach for analyzing the nonperturbative power corrections to groomed observables. Based on recent advancement in the understanding of the nonperturbative structure of the soft drop jet mass in refs. [82, 83], the power corrections in this case can be similarly encoded into universal, $\mathcal{O}(\Lambda_{\rm QCD})$ constants as in eq. (1.2). These power corrections in the groomed case in fact constitute a very non-trivial extension and a combination of those in eq. (1.2) for ungroomed jet mass shift and ungroomed jet p_T. More specifically, it was shown in ref. [82] that, in the region where soft drop is *active* and where a perturbative description is valid, the leading corrections from hadronization take the following form:

$$\frac{1}{\sigma_\kappa}\frac{\mathrm{d}\sigma_\kappa}{\mathrm{d}m_J^2} = \frac{1}{\hat{\sigma}_\kappa}\frac{\mathrm{d}\hat{\sigma}_\kappa}{\mathrm{d}m_J^2} - Q\Omega_{1\kappa}^{\circledcirc}\frac{\mathrm{d}}{\mathrm{d}m_J^2}\left(\frac{1}{\hat{\sigma}_\kappa}\frac{\mathrm{d}\hat{\sigma}_\kappa^{\circledcirc}}{\mathrm{d}m_J^2}\right) + \frac{\Upsilon_{1,0\kappa}^{\circledcirc} + \beta\Upsilon_{1,1\kappa}^{\circledcirc}}{Q}\frac{1}{\hat{\sigma}_\kappa}\frac{\mathrm{d}\hat{\sigma}_\kappa^{\circledcirc}}{\mathrm{d}m_J^2} + \cdots, \qquad (1.3)$$

where the left hand side denotes the hadron-level soft drop jet mass cross section initiated by a parton $\kappa = $ quark/gluon and Q is the hard scale characterizing the jet. The first term on the right hand side with a hat, $\mathrm{d}\hat{\sigma}^\kappa$ is the perturbative parton level soft drop jet mass cross-section. The $1/\hat{\sigma}_\kappa$ factor is included to consider normalized cross section. In the region of small jet masses that we are interested in, these functions can be unambiguously defined as jet mass distributions of jets with a specific quark or gluon flavor. See ref. [55] for more details on how these objects can be systematically defined in the context of inclusive or exclusive jet measurements. The remaining pieces in eq. (1.3) are the nonperturbative corrections parameterized in terms of the three $\mathcal{O}(\Lambda_{\rm QCD})$ universal nonperturbative (NP) constants $\Omega_{1\kappa}^{\circledcirc}$, $\Upsilon_{1,0\kappa}^{\circledcirc}$ and $\Upsilon_{1,1\kappa}^{\circledcirc}$. They appear with certain jet mass dependent functions that we describe below.

The form of NP power corrections in eq. (1.3) holds for jet masses that satisfy the criteria

$$\frac{Q\Lambda_{\rm QCD}}{m_J^2}\left(\frac{m_J^2}{QQ_{\rm cut}}\right)^{\frac{1}{2+\beta}} \ll 1, \qquad \text{(soft drop stopping emission is perturbative)}, \quad (1.4)$$

$$m_J^2 < QQ_{\rm cut}, \quad \text{(soft drop is active)}.$$

---

[2]Further assumptions about the hadronization physics in the dispersive approach [8] can be used to reduce them down to a single parameter (which also reveals that the leading hadronization correction to the jet p_T, $\Upsilon_1^{(-1)} < 0$).
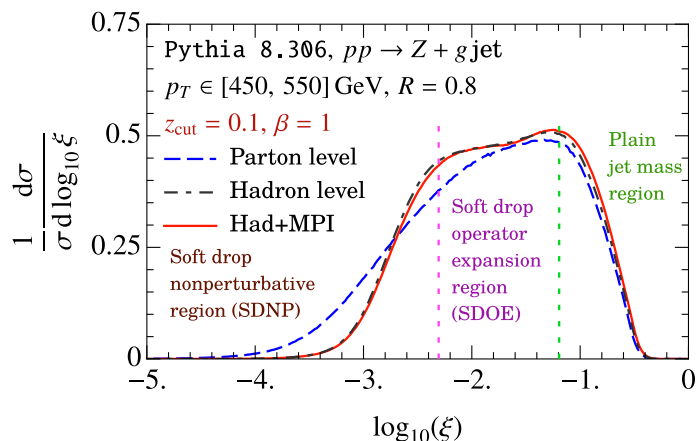
Figure 1. Various regions of the soft drop jet mass spectrum that are differently affected by nonperturbative corrections. This work focuses on the middle, soft drop operator expansion region, where the hadronization corrections, while significant, can be described in a systematic expansion. Here $\xi = m_J^2/(p_T R)^2$.

Here $Q_{\text{cut}} \sim Q z_{\text{cut}}$ is the energy scale associated with soft drop and is precisely defined below. This region is referred to as the soft drop operator expansion (SDOE) region and is shown in figure 1. The first condition ensures that the subjet that stops the soft drop is typically perturbative, such that soft drop spectrum can be calculated in perturbation theory. This need not always be the case, but the cases where the stopping subjet is nonperturbative are power suppressed. The second condition constraints the softer of the stopping pair to be also collinear to the jet, such that the radiation at wider angles is groomed away. For larger jet masses, the groomer can stop at wider angles and the distribution consequently looks very similar to the ungroomed jet mass spectrum,

$$m_J^2 \gtrsim Q Q_{\text{cut}} \,, \qquad \text{(plain jet mass resummation region)} \,. \qquad (1.5)$$

Interestingly, it is only with the LHC kinematics with jets of transverse momenta $\sim 500\,\text{GeV}$ that this OPE region opens up and becomes accessible.[3] We also note that in eq. (1.3) we have ignored the impact of hadronization on the hard scale Q. This is justified because the spectrum in the SDOE region for large Q values ($p_T \gtrsim 400\,\text{GeV}$) is largely independent of the jet p_T, and while hadronization and underlying event impacts the relative statistics in different jet p_T bins, the impact on normalized cross section shown in figure 1 is expected to be sub-dominant. This was also shown to be the case in ref. [61] where a transfer matrix approach was employed to investigate the effect of migration across p_T bins due to hadronization and UE.

The three parameters are grouped in two terms which have distinct physical meanings associated with them. The first term proportional to $\Omega_{1\kappa}^{\oplus}$ is the "shift correction" analogous

---

[3]Soft drop jet mass distributions (and soft drop angularities) have been measured in the legacy ALEPH data in ref. [84]. However, at LEP energies the above conditions cannot be satisfied and almost the entire soft drop jet mass spectrum (including even the cusp region) is fully nonperturbative.

to eq. (1.2) that captures a shift to the groomed jet mass, coming from the NP particles[4] that survive grooming. The second term proportional to $\Upsilon_{1,0\kappa}^{\circledcirc}$ and $\Upsilon_{1,1\kappa}^{\circledcirc}$ is referred to as the "boundary correction" that describes how the outcome of the soft drop test (with respect to a reference parton level configuration) is altered due to hadronization. The parameter $\Upsilon_{1,0\kappa}^{\circledcirc}$ is exactly analogous to $\Upsilon_{\kappa}^{(-1)}$ in eq. (1.2) but now refers to the p_T of the dynamically determined collinear-soft (c-soft) subjet that is found at the last stage of the soft drop groomer. The term proportional to β is related to the change in direction of this c-soft subjet relative to the collinear core due to hadronization. Thus, an interesting implication of jet grooming is that both types of hadronization corrections appear in the same groomed observable.

We pause to note that '...' in eq. (1.3) refer to two types of subleading power corrections. The first kind are those that are suppressed by higher powers of $\Lambda_{\rm QCD}$. These power corrections grow as the groomed jet mass is reduced and become $\mathcal{O}(1)$ for small jet masses beyond the SDOE region. The second type corresponds to those where the radiation pattern of the groomed jet is more complicated than a simplest possible "two-pronged configuration" of a collinear and c-soft subjet. The second type of correction is a next-to-leading logarithmic (NLL) effect, as at leading-logarithmic accuracy, strong ordering of angles between the perturbative soft radiation off the jet can be assumed, such that any further radiation beyond the c-soft subjet must lie at hierarchically small angles within the collinear jet, resulting in a dipole-configuration that governs the hadronization corrections. Equivalently, eq. (1.3) can be seen as an expansion in number of identified and ordered soft subjets, analogous to the dressed gluon expansion employed in non-global logarithms (NGL) resummation [85] and more recently for resummation of jet mass close to the cusp [86]. With this interpretation, the leading terms in eq. (1.3) represent the leading single-subjet piece. The dominance of the two-prong configuration was crucial in ref. [82] for identifying universal NP constants in eq. (1.3).

Because these corrections necessarily involve kinematic properties of the c-soft subjet that cannot be unambiguously identified via the jet mass measurement, these corrections appear with certain jet mass dependent perturbative weights $\mathrm{d}\hat{\sigma}_{\kappa}^{\circledcirc,\circledcirc}$ that capture this dynamical effect. Furthermore, in the SDOE region specified by eq. (1.4), these weights are perturbatively calculable and hence indicated with a hat. These weights are related to moments of the groomed jet radius, R_g, the angular separation between the soft drop-stopping pair, at a given jet mass m_J^2.[5] They are given in terms of cross sections that are differential in these kinematic properties of the c-soft subjet in addition to the jet mass:

$$\frac{1}{\hat{\sigma}_\kappa}\frac{\mathrm{d}\hat{\sigma}_\kappa^{\circledcirc}}{\mathrm{d}m_J^2} \equiv \int \mathrm{d}r_g\, r_g \frac{1}{\hat{\sigma}_\kappa}\frac{\mathrm{d}^2\hat{\sigma}_\kappa}{\mathrm{d}m_J^2\mathrm{d}r_g}\,, \tag{1.6}$$

$$\frac{1}{\hat{\sigma}_\kappa}\frac{\mathrm{d}\hat{\sigma}_\kappa^{\circledcirc}}{\mathrm{d}m_J^2} \equiv \int \frac{\mathrm{d}r_g\mathrm{d}z_g\, \delta\big(z_g - z_{\rm cut}r_g^\beta\big)}{r_g}\frac{1}{\hat{\sigma}_\kappa}\frac{\mathrm{d}^3\hat{\sigma}_\kappa}{\mathrm{d}m_J^2\mathrm{d}r_g\mathrm{d}z_g}\,. \tag{1.7}$$

---

[4]We will often refer to hadrons produced at the last stage of hadronization (for example, subsequent to a parton shower in an event generator) as "nonperturbative particles". In the language of SCET, these corresponds to distinct modes in the effective theory that have significantly lower virtuality $\sim \Lambda_{\rm QCD}$ compared to other perturbative modes.

[5]Unlike ref. [87], we do not normalize the groomed jet radius R_g by the original jet radius R. However, for sake of simplifying calculations we will consider a normalized variant r_g defined in eq. (2.16) below.

We have expressed here the groomed jet radius R_g in terms of $r_g = R_g/R$, which we also generalize below in eq. (2.16) to include jets in e^+e^- collisions. Here, z_g is the energy (or p_T) fraction of the c-soft subjet. These moments in fact appear in precisely the same fashion as the factor of jet radius R does in the leading NP power correction in the ungroomed jet mass and jet p_T in eq. (1.2). For the shift correction, the groomed jet mass shift is given by

$$m^2_{J,\mathrm{sd}} = \hat{m}^2_{J,\mathrm{sd}} + p_T R_g \Omega^{\circledcirc}_{1\kappa} . \tag{1.8}$$

Here $\hat{m}_{J,\mathrm{sd}}$ is the jet mass of a reference parton level configuration. Here we are implicitly considering inclusively identified jets, where, as we will discuss below, the hard scale $Q = p_T R$. Normalizing the jet mass squared by Q^2 we find that the shift $\delta m^2_{J,\mathrm{sd}} = r_g \Omega^{\circledcirc}_{1\kappa}/Q$. Thus, eq. (1.6) indicates that r_g must be averaged over all possible values allowed for a given jet mass measurement m_J. Lastly, because this shifts the value of the jet mass, the corresponding shift upon Taylor-expanding appears as a derivative as shown in eq. (1.3).

The term in eq. (1.7) apperaing with a $1/r_g$ factor is analogous to $1/R$ factor with the leading hadronization effect associated with the jet p_T in eq. (1.2). Instead of a shift in the jet mass, this effect modifies the normalization of the cross section. It is analogous to how the normalization of the jet mass spectrum changes from parton-level to hadron-level due to migration of events across p_T bins. Just as this effect predominantly affects the events that are at the boundary of the p_T-bin, the analogous correction in eq. (1.7) appears in groomed jet mass when there are c-soft subjets near the "boundary" of passing/failing the soft drop condition, i.e. when $z_g \approx z_{\mathrm{cut}} r_g^\beta$, such that effects of hadronization can lead to different outcomes at parton and hadron levels. Hence, in eq. (1.7) an additional δ-function for soft drop boundary is included. The factor of $1/r_g$ can be understood by noting that the parton level values $\hat{z}_g$ and $\hat{r}_g$ upon hadronization are modified as

$$z_g = \hat{z}_g + \frac{1}{r_g} \frac{\Upsilon^{\circledcirc}_{1,0\kappa}}{Q} , \qquad\qquad r_g = \hat{r}_g - \frac{\Upsilon^{\circledcirc}_{1,1\kappa}}{Q} . \tag{1.9}$$

The two $\mathcal{O}(\Lambda_{\mathrm{QCD}})$ constants $\Upsilon^{\circledcirc}_{1,0\kappa}$ and $\Upsilon^{\circledcirc}_{1,1\kappa}$ respectively encode the shift in the c-soft subjet p_T and the groomed jet radius. When combined together, along with the factor of β resulting from differentiation of r_g^β, we arrive at the boundary correction in eq. (1.3). Finally, as a technical remark, while eq. (1.7) is more intuitive to understand when expressed in terms of z_g, in practice, we will find it simpler to compute this correction by varying the soft drop condition itself in the doubly differential cross section in eq. (1.6), allowing us to recycle the calculations for the shift correction.

Next, while typical values of the grooming parameters lead to strong suppression of underlying event (UE) and ISR effects, there are situations where less aggressive grooming is desirable. For example, in the case of groomed boosted top quark jets [26], a strong 10%-level grooming invalidates a simple inclusive description of the top decay, and instead a light grooming of 1%-level is desired. Likewise, for exclusively studying soft radiation and quark gluon discrimination using the collinear-drop [31, 33], combinations of light and more aggressive soft drop is employed. In such scenarios the effect of underlying event on the jet mass spectrum is no longer negligible. We show in figure 2 the spectrum for
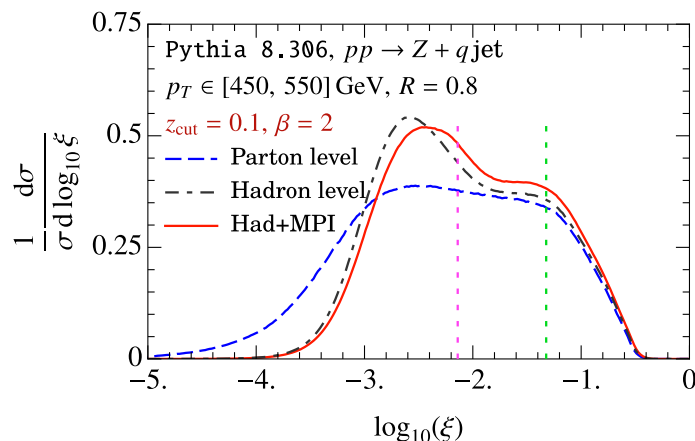
Figure 2. For certain values of soft drop parameters, such as $\beta = 2$, the underlying event effects can be significant. Here $\xi = m_J^2/(p_T R)^2$.

$z_{\text{cut}} = 0.1$ and $\beta = 2$. In the SDOE region the impact of UE is even somewhat larger than hadronization. While it is impossible to predict the effects of UE from first principles, we can nevertheless attempt to phenomenologically describe these effects by making certain reasonable assumptions. The UE distribution is to a good approximation uniform in rapidity and independent of the hard scattering, such that it makes a contribution proportional to the jet area [88]. Under these assumptions, in ref. [89] we show that effects of ISR and UE appear as corrections associated with higher powers of groomed jet radius:

$$\frac{1}{\sigma_\kappa}\frac{\mathrm{d}\sigma_\kappa^{\text{had}+\text{UE}}}{\mathrm{d}m_J^2} = \frac{1}{\sigma_\kappa}\frac{\mathrm{d}\sigma_\kappa}{\mathrm{d}m_J^2} - Q\Omega_{\text{UE}}^{\circledcirc}\frac{\mathrm{d}}{\mathrm{d}m_J^2}\left(\frac{C_{1\kappa}^{(4)}(m_J^2)}{\sigma_\kappa}\frac{\mathrm{d}\sigma_\kappa}{\mathrm{d}m_J^2}\right) \tag{1.10}$$
$$+ \frac{\Upsilon_{0\text{UE}}^{\circledcirc} + \beta\Upsilon_{1\text{UE}}^{\circledcirc}}{Q}\frac{C_{2\kappa}^{(2)}(m_J^2)}{\sigma_\kappa}\frac{\mathrm{d}\sigma_\kappa}{\mathrm{d}m_J^2} + \cdots,$$

where $\mathrm{d}\sigma_\kappa$ (without a hat) is the hadron level cross section and the left hand side, $\mathrm{d}\sigma_\kappa^{\text{had}+\text{UE}}$ is the hadron+UE level cross section. The jet mass dependent coefficients $C_{1,2\kappa}^{(n)}(m_J^2)$ are parton level r_g-moments of the doubly differential soft drop and boundary soft drop cross sections:

$$\frac{1}{\hat{\sigma}_\kappa}\frac{\mathrm{d}\hat{\sigma}_\kappa}{\mathrm{d}m_J^2}C_{1\kappa}^{(n)}(m_J^2) \equiv \int \mathrm{d}r_g\, r_g^n\, \frac{1}{\hat{\sigma}_\kappa}\frac{\mathrm{d}^2\hat{\sigma}_\kappa}{\mathrm{d}m_J^2 \mathrm{d}r_g}, \tag{1.11}$$
$$\frac{1}{\hat{\sigma}_\kappa}\frac{\mathrm{d}\hat{\sigma}}{\mathrm{d}m_J^2}C_{2\kappa}^{(n)}(m_J^2) \equiv \int \mathrm{d}r_g \mathrm{d}z_g\, \delta(z_g - z_{\text{cut}}r_g^\beta)\, r_g^n\, \frac{1}{\hat{\sigma}_\kappa}\frac{\mathrm{d}^3\hat{\sigma}_\kappa}{\mathrm{d}m_J^2 \mathrm{d}r_g \mathrm{d}z_g}.$$

The appearance of $n = 4$ for the shift correction and $n = 2$ for the boundary correction is analogous to the jet radius scaling of the impact of ISR and underlying event on the jet mass and jet p_T distribution respectively [8].

1.2 Precisely computing the perturbative weights of nonperturbative moments

We thus see that eq. (1.3) significantly constrains the form of the leading nonperturbative corrections, which can be parameterized for a given flavor of jet in terms of 3 constants. However, for eq. (1.3) to be useful in precision physics with soft drop jet mass, we are required to accurately calculate the jet mass dependent weights in perturbation theory. The accuracy with which these weights can be determined in turn determines the extent to which the NP parameters can be extracted or constrained in an analysis with real world collider data. In ref. [82], a straightforward calculation of these weights at LL accuracy in the coherent branching formalism was presented. The factorization in eq. (1.3) was tested by performing a comparison between parton and hadron level jet mass spectra in the $e^+e^- \to q\bar{q}$ process in the dijet region simulated in the MC event generators using the LL-accurate predictions of the weights. However, while a good agreement with the predictions of factorization was found, there was no clear procedure to ascertain the perturbative uncertainty in the LL calculations.

To enable more precise predictions of these weights, it was in ref. [83] where their computation was first recast as moments of a multi-differential soft drop cross section. By dissecting the kinematic phase space of r_g and the m_J, ref. [83] identified the relevant set of effective field theories that are required for a precise computation of the doubly differential cross section in the SDOE region.[6] The boundary correction in eq. (1.7) was computed by considering variations in the soft drop condition in the doubly differential $\frac{\mathrm{d}^2\hat{\sigma}_\kappa}{\mathrm{d}m_J^2\mathrm{d}r_g}$ cross section. The EFT formalism enabled a systematic improvement in the computation of these weights. In ref. [83] these moments were computed with NLL resummation including $\mathcal{O}(\alpha_s)$ singular matrix elements to achieve NLL$'$ accuracy in the SDOE region. At the same time, the framework also enabled a systematic estimate of the perturbative uncertainty associated with these weights that was previously lacking in the LL calculations in the coherent branching framework.

In this work, with the goal of providing necessary perturbative input for eq. (1.3) for precision phenomenology, we further improve the prediction of these jet mass dependent perturbative weights. A straightforward improvement comes from employing relatively recently calculated two-loop non-cusp anomalous dimensions of certain factorization functions associated with soft drop from ref. [91] to extend the resummation of global logarithms in the doubly differential cross section to NNLL accuracy. More crucially, we extend the calculation by matching the doubly differential cross section in the SDOE region in eq. (1.4) to the ungroomed region for $m_J^2 \gtrsim QQ_{\mathrm{cut}}$ which involves calculating new contributions previously not considered in ref. [83]. There the power corrections of the form $\left(m_J^2/(QQ_{\mathrm{cut}})\right)^{2/(2+\beta)}$ were systematically dropped, which become significant close to the soft drop cusp for $m_J^2 \lesssim QQ_{\mathrm{cut}}$. They also impact the location of the soft drop cusp which differs between NLL and NNLL estimates. Thus, it is essential to include these power corrections in order to provide the necessary perturbative input for precision phenomenology consistent with the NNLL soft drop jet mass prediction.

---

[6]See also [27, 32, 90] for applications of doubly differential cross sections in the context of other groomed jet observables.

In ref. [55], the matching of the single differential jet mass spectrum $\mathrm{d}\sigma/\mathrm{d}m_J^2$ between soft drop and plain jet mass resummation regions was derived from demanding consistency with the doubly differential cross section $\mathrm{d}\Sigma(r_g)/\mathrm{d}m_J^2$ that in the limit $r_g = r_g^{\max}(m_J^2) \leq 1$ (applied as a cumulative measurement of r_g) reduces to the jet mass distribution, $\mathrm{d}\Sigma(r_g^{\max}(m_J^2))/\mathrm{d}m_J^2 = \mathrm{d}\sigma/\mathrm{d}m_J^2$. As discussed in ref. [83], the calculation of the doubly differential cross section involves consideration of three different EFTs depending on whether the groomed jet radius is close to the minimum $r_g \gtrsim r_g^{\min}(m_J^2)$ ("min-R_g") or maximum kinematic bound $r_g \lesssim r_g^{\max}(m_J^2)$ imposed by jet mass measurement ("max-R_g"), or in an intermediate region within these bounds $r_g^{\min}(m_J^2) \ll r_g \ll r_g^{\max}(m_J^2)$ ("int-R_g"). The regions of validity of these three EFTs are nontrivial patches in the m_J^2-r_g plane. Consequently, the transition for the doubly differential cross section between the soft drop and plain jet mass resummation regions can be expected to be significantly more intricate than $\mathrm{d}\sigma/\mathrm{d}m_J^2$ due to nontrivial interplay of various power expansion that determine the two-dimensional region in the m_J^2-r_g plane for the three EFTs; see figure 3.

Fortunately, as we show in this paper, the results in the min-R_g and int-R_g regimes can be smoothly continued into the plain jet mass region. On the other hand, the max-R_g regime (of which the single differential distribution $\mathrm{d}\sigma/\mathrm{d}m_J^2$ is a component) transitions *discontinuously* between the soft drop and plain jet mass resummation region. This is because, different from soft drop resummation region where $r_g \leq r_g^{\max} \ll 1$, in the plain jet mass region the r_g is close to the jet radius boundary $r_g = 1$ and the mode structure of the soft sector in the EFT changes. However, the mode and resummation structure of this EFT is identical to that of single differential jet mass (in either regions), and the dependence on r_g in this EFT can be incorporated via fixed order calculations. This allows us to employ similar strategy as in ref. [55] to compute this matching. To achieve a smooth transition between various patches in the entire m_J^2-r_g plane demarcating the EFTs we expand the toolbox of ref. [83] including new resummation kernels, generalizations of profile functions and weight functions described below. Finally, we also compute here the $\mathcal{O}(\alpha_s)$ non-singular pieces that capture $\mathcal{O}(z_{\mathrm{cut}})$ power corrections for the doubly differential cross section that were previously not taken into account.

As above, the computation of the boundary soft drop cross section and its moments in eq. (1.7) is also similarly extended into the plain jet mass region. In fact, we will find that including the matching to the plain jet mass region significantly impacts the $C_{2\kappa}^{(n)}$ moment defined in eq. (1.11) in the cusp region relative to $C_{1\kappa}^{(n)}$ because this moment sharply drops to zero past the soft drop cusp. Furthermore, as shown in ref. [92], the dominant uncertainty in the determination of nonperturbative parameters results from that of the $C_{2\kappa}^{(-1)}$ moment because in the case of $C_{1\kappa}$, the uncertainties in the single and doubly differential cross sections are highly correlated and cancel in the ratio. The computation of $C_{2\kappa}$ is also more challenging as the tree-level result is $\mathcal{O}(\alpha_s)$ and effects of resummation start at $\mathcal{O}(\alpha_s^2)$ captured through cross terms of various one-loop pieces. When extending to the plain jet mass resummation region, we find that new additional $\mathcal{O}(\alpha_s^2)$ cross terms arise. As a result, while conceptually straightforward, the computation of the boundary cross section quickly becomes unwieldy due to appearance of several resummation kernels associated with these new pieces in the plain jet mass region and $\mathcal{O}(\alpha_s^2)$ cross terms, exhibiting intricate

cancellations as we transition from groomed to ungroomed region. We overcome this and simultaneously achieve an efficient numerical implementation of these resummation kernels by recasting them as certain "integral transforms" involving nested plus-functions. We find a significantly faster implementation of the boundary cross section compared to ref. [83] where these kernels were instead expressed in terms of incomplete beta functions and their integrals.

The results of this work are used in complementary applications of eqs. (1.3) and (1.10) and discussed in companion papers: firstly, as already mentioned above, in ref. [55] the NNLL results are employed for estimating impact of the nonperturbative corrections on α_s-determination in a completely model-independent approach. Secondly, in ref. [92] these results are used for a precise calibration of MC hadronization models in event generators, investigating their interplay with parton showers, and rigorously testing the universality predictions of eq. (1.3). Analysis of ref. [92] confirms that indeed with precise calculations of the perturbative weights with reliable uncertainty estimates, a determination of these parameters with LHC data is foreseeable. Finally, in ref. [89] the calculations of the moments relevant for UE and ISR are used for an analogous calibration of underlying event contribution in simulations. An interesting extension of this approach will be to consider nonperturbative corrections to groomed angularities. We expect the dependence the angularity exponent to be captured by more general perturbative weights. However, since hadron mass effects impact jet mass and angularities (when measured in their usual scheme) differently, care must be taken in relating the associated nonperturbative parameters.

The organization of the paper is as follows: in section 2 we discuss the effective field theories required for a complete prediction of the doubly differential groomed cross section and identify the relevant EFT modes for extension into the plain jet mass resummation region. Before describing in detail the factorization formulae associated with each of these regions, we will find it advantageous to first review $\mathcal{O}(\alpha_s)$ computation of various factorization functions in section 3. In section 4 we describe how the results for these functions are incorporated into the factorization formulae. The cross sections in various regions are eventually combined together in section 5 where we also describe the procedure for obtaining perturbative uncertainty. The analogous calculation for the boundary correction is described in section 6. Having discussed the complete calculation of the perturbative weights, in section 7 we compare the results of this work with the previous calculation in ref. [83] as well as their impact on the jet mass spectrum and on the calibration of MC hadronization models in terms of soft drop nonperturbative moments. In section 8 we show a comparison of the NNLL resummed results and parton shower simulations for various moments of r_g, for both shift and boundary cross sections. We conclude in section 9. In the appendices we consolidate some of the technical details.

2 Effective theory regions and modes

In this section we review the relevant results of previous work from refs. [55, 83] and discuss the mode structure of the doubly differential cross section in the plain jet mass region. We first review in section 2.1 the measurement and kinematics of inclusive jets and the various energy scales associated with the groomed jet mass measurement. In sections 2.2 and 2.3

we summarize the various effective field theory regions and modes derived in ref. [83] and the new cases from extension into the plain jet mass region.

2.1 Measurement and kinematics

For concreteness, our starting point is the inclusive jet measurement in hadron colliders. However, we will shortly generalize our notation to also simultaneously describe exclusive jets in pp and inclusive jets in e^+e^- collisions. In the formal limit of jet radius $R/2 \ll 1$ the cross section for the process $pp \to \mathrm{jet} + X$, where X includes any radiation we are inclusive over factorizes as [93–95]

$$\frac{\mathrm{d}^3\Sigma(R_g)}{\mathrm{d}p_T \mathrm{d}\eta_J \mathrm{d}m_J^2} = \sum_{abc} \int \frac{\mathrm{d}x_a \mathrm{d}x_b \mathrm{d}z}{x_a x_b z} f_a(x_a,\mu) f_b(x_b,\mu) H_{ab}^c\Big(x_a, x_b, \eta_J, \frac{p_T}{z}, \mu\Big) \mathcal{G}_c(z, m_J^2, R_g, p_T, R, \mu).$$
(2.1)

Here $f_{a,b}$ are parton distribution functions which when combined with inclusive hard function H_{ab}^c account for the hard process leading to production of parton c. This can also be generalized to describe processes with an additional vector boson V, such as $pp \to \mathrm{jet} + V + X$. The subsequent branching of the parton c to form a jet is described via the inclusive jet function $\mathcal{G}_c$. In addition to the jet p_T and pseudorapidity η_J, $\mathcal{G}_c$ depends on z, the momentum fraction of original parton retained in the reconstructed jet as well as (groomed) jet mass. Finally $\mathrm{d}\Sigma(r_g)$ refers to the cross section that is differential in the jet kinematics and the jet mass with an additional upper bound of R_g as the groomed jet radius.

In the small jet mass limit $m_J^2 \ll p_T^2 R^2$, the radiation in the jet is constrained to be predominantly soft and collinear, such that the inclusive jet function factorizes as

$$\mathcal{G}_c^{\mathrm{fact.}}(z, m_J^2, R_g, p_T, R, \mu) = \sum_i \mathcal{H}_{c \to i}(z, p_T R, \mu) \mathcal{J}_i(m_J^2, R_g, p_T, \eta_J, R, \mu) \left[1 + \mathcal{O}\left(\frac{m_J^2}{p_T^2 R^2}\right)\right].$$
(2.2)

The factorization involves separation of hard collinear modes at scales $p_T R$ described by $\mathcal{H}_{c \to i}$, and soft and collinear modes in a multiscale function $\mathcal{J}_i$. As discussed in ref. [55], in this region, the normalized cross section can be expressed as

$$\frac{1}{\sigma_{\mathrm{incl}}(p_T, \eta_J)} \frac{\mathrm{d}^3\Sigma(R_g)}{\mathrm{d}m_J^2 \mathrm{d}p_T \mathrm{d}\eta_J}$$
$$= x_q(p_T R, \eta_J, \mu) \, \tilde{\mathcal{G}}_q(m_J^2, R_g, p_T R, \mu) + x_g(p_T R, \eta_J, \mu) \tilde{\mathcal{G}}_g(m_J^2, R_g, p_T R, \mu).$$
(2.3)

where $x_{q,g}$ are quark/gluon fractions that are theoretically well defined, but renormalization scale μ-dependent objects. These fractions depend on the underlying hard process and being normalized quantities are only mildly dependent on the parton distribution functions. Our focus will be on computing the piece that captures the jet mass and groomed jet radius dependence $\tilde{\mathcal{G}}_\kappa$, which is interpreted as the normalized cross section for parton κ:

$$\tilde{\mathcal{G}}_\kappa(m_J^2, R_g, p_T R, \mu) \equiv \frac{1}{\sigma_\kappa^{\mathrm{incl}}} \frac{\mathrm{d}\Sigma_\kappa(R_g)}{\mathrm{d}m_J^2} = N_{\mathrm{incl}}^\kappa(p_T R, \mu) \mathcal{J}_\kappa(m_J^2, p_T, \eta_J, R, \mu).$$
(2.4)

Here the normalization factor $N_{\mathrm{incl}}^{\kappa}$ arises from factoring out the piece of $\mathcal{H}_{c \to i}$ that describes the Sudakov double-logarithmic part connected with the soft-collinear factorization of $\mathcal{G}_c$ in eq. (2.2). The product of $N_{\mathrm{incl}}^{\kappa}$ and $\mathcal{J}_{\kappa}$ lead to an RG-invariant combination that can be independently studied. When considering different measurements involving groomed jet mass and groomed jet radius, only the function $\mathcal{J}_{\kappa}$ will be modified. We will state the all-orders factorization formulae below in terms of $\mathcal{G}_c$ in eq. (2.2), and employ eq. (2.4) for numerical implementation.

2.1.1 Hard kinematics

The above formulation in terms of the normalized inclusive cross section $\tilde{\mathcal{G}}_{\kappa}$ and quark/gluon fractions can be extended to exclusive, fixed number of jets with a jet veto on additional radiation, or jets in e^+e^- collisions. Apart from different definitions of the quark gluon fractions, this involves straightforward substitutions of the hard scales and kinematic and grooming parameters. Thus, it will prove worthwhile to develop a unified notation to simultaneously treat all these cases. We first define the hard scale for the following scenarios:

$$Q_{\mathrm{incl}}^{pp} \equiv p_T R\,, \qquad Q_{\mathrm{excl}}^{pp} \equiv 2 p_T \cosh \eta_J\,, \qquad Q_{\mathrm{incl}}^{e^+e^-} \equiv 2 E_J \tan \frac{R}{2}\,, \tag{2.5}$$

where the subscript 'incl' ('excl') indicates that the jets are identified inclusively (exclusively) and the superscript for the incoming partons involved. This way, the function $N_{\mathrm{incl}}^{\kappa}$ only depends on the scale Q. We now define a dimensionless variable ξ as a substitute for the jet mass:

$$\xi \equiv \frac{m_J^2}{Q^2}\,. \tag{2.6}$$

We have suppressed the superscripts and subscripts on Q, and will generally follow this convention, such that the above definition of ξ can be adjusted for the three situations in eq. (2.5).

Next, to describe dynamics of the soft and collinear radiation we will work with light cone coordinates defined via the light-like vectors

$$n^{\mu} \equiv \zeta^{-1}\big(1, \vec{n}\big)\,, \qquad \bar{n}^{\mu} \equiv \zeta\big(1, -\vec{n}\big)\,, \tag{2.7}$$

where the parameter ζ encodes a large boost in the jet direction given by:

$$\zeta_{\mathrm{incl}}^{pp} \equiv \frac{R}{2 \cosh \eta_J}\,, \qquad \zeta_{\mathrm{excl}}^{pp} \equiv 1\,, \qquad \zeta_{\mathrm{incl}}^{e^+e^-} \equiv \tan \frac{R}{2}\,. \tag{2.8}$$

Including the boost factors in the reference light-like vectors will allow us to work with hemisphere-like coordinates and eliminate several intermediate factors involving jet radius. In terms of these light-like vectors, we will follow the following light-cone decomposition of momentum q^{μ}:

$$q^{\mu} = q^+ \frac{\bar{n}^{\mu}}{2} + q^- \frac{n^{\mu}}{2} + q_{\perp}^{\mu}\,, \qquad q^+ \equiv n \cdot q\,, \qquad q^- \equiv \bar{n} \cdot q\,. \tag{2.9}$$

2.1.2 Soft drop kinematics

Next we define some useful variables associated with soft drop. The criteria for soft drop differs between e^+e^- and pp cases and is given by

$$\frac{\min(E_i, E_j)}{E_i + E_j} > z_{\mathrm{cut}} \left(\sqrt{2} \frac{\sin(\theta_{ij}/2)}{\sin(R_0^{e^+e^-}/2)} \right)^\beta, \qquad (e^+e^- \text{ case}), \qquad (2.10)$$

$$\frac{\min(p_{T_i}, p_{T_j})}{p_{T_i} + p_{T_j}} > z_{\mathrm{cut}} \left(\frac{\Delta R_{ij}}{R_0^{pp}} \right)^\beta, \qquad (pp \text{ case}),$$

Application of soft drop introduces an additional scale Q_{cut} that plays a role in distinguishing the radiation that is groomed away from the radiation that is not, which is given by

$$Q_{\mathrm{cut,\,incl}}^{pp} \equiv z_{\mathrm{cut}} Q_{\mathrm{incl}}^{pp} \left(\frac{R}{R_0^{pp}} \right)^\beta, \qquad Q_{\mathrm{cut,\,excl}}^{pp} \equiv z_{\mathrm{cut}} Q_{\mathrm{excl}}^{pp} \left(\frac{2\cosh\eta_J}{R_0^{pp}} \right)^\beta, \qquad (2.11)$$

$$Q_{\mathrm{cut,\,incl}}^{e^+e^-} \equiv z_{\mathrm{cut}} Q_{\mathrm{incl}}^{e^+e^-} \left(\sqrt{2} \frac{\tan\frac{R}{2}}{\sin\frac{R_0^{e^+e^-}}{2}} \right)^\beta.$$

As we probe jets with smaller masses, the emissions at wider angles become progressively softer and are groomed away. Using the scale Q_{cut} we can identify the jet mass transition point below which soft drop becomes active. This is simply given by

$$\xi_0 \equiv \frac{Q_{\mathrm{cut}}}{Q}. \qquad (2.12)$$

This point roughly defines the location of the distinct soft drop cusp, and for the reasons that will become clear below, is referred to as the "soft-collinear transition point". Higher order corrections slightly modify this value. We will see below that at $\mathcal{O}(\alpha_s)$, the transition point appears at the location

$$\xi_0' \equiv \frac{\xi_0}{\left(1 + \zeta^2\right)^{\frac{2+\beta}{2}}}. \qquad (2.13)$$

We will refer to ξ_0' as the soft wide-angle transition point. ξ_0' corresponds to the location of the cusp for the NNLL resummed groomed jet mass spectrum. For later use we also define

$$Q'_{\mathrm{cut}} \equiv Q\xi_0' = \frac{Q_{\mathrm{cut}}}{\left(1 + \zeta^2\right)^{\frac{2+\beta}{2}}}. \qquad (2.14)$$

Finally, the of validity of perturbative calculations is specified by eq. (1.4), which demarcates the extent of the SDOE region. In terms of ξ, we define the lower end of the perturbative region by

$$\xi_{\mathrm{SDOE}} \equiv \xi_0 \left(\frac{\rho \Lambda_{\mathrm{QCD}}}{Q\xi_0} \right)^{\frac{2+\beta}{1+\beta}}, \qquad (2.15)$$

where the factor $\rho > 1$ is included to approximate the strong inequality in eq. (1.4). Below we will take $\rho = 5$.

Finally, we now specify our choice of normalization for the groomed jet radius. We refer to R_g as the groomed jet radius which can stand for rapidity invariant angular distance in pp collisions or physical angular distance in e^+e^- collisions. For simplicity, we will work with a normalized version of R_g to simultaneously treat these two cases defined by

$$r_g^{pp} \equiv \frac{R_g}{R} \,, \qquad r_g^{e^+e^-} \equiv \frac{\tan \frac{R_g}{2}}{\tan \frac{R}{2}} \,. \tag{2.16}$$

Here the same definitions apply for both inclusive and exclusive cases in pp. In this normalization, r_g can at most be 1, which corresponds to scenario where grooming does not eliminate any radiation from the jet.

As detailed in ref. [83], the measurement of jet mass m_J^2, or equivalently ξ, puts kinematic bounds on the groomed jet radius, such that

Simultaneous ξ, r_g measurement: $\qquad r_g^{\min}(\xi) \leq r_g \leq r_g^{\max}(\xi) \,, \tag{2.17}$

where

$$r_g^{\min}(\xi) = \sqrt{\xi} \,, \qquad r_g^{\max}(\xi) \approx \min \left\{ \left(\frac{\xi}{\xi_0} \right)^{\frac{1}{2+\beta}}, 1 \right\} . \tag{2.18}$$

The $r_g^{\min}$ arises from the kinematic bound imposed by the jet mass measurement: for a given jet mass ξ, it is impossible to squeeze the radiation into a jet of radius smaller than $r_g^{\min}(\xi)$. The maximum bound has two terms. For $\xi < \xi_0$, we are in the region where grooming is active. Here the combination of the groomed jet mass measurement and requirement that the radiation pass grooming leads to the first of the two upper bounds shown. For $\xi > \xi_0$, the radiation can be close to the jet boundary and still pass the groomer, and hence the upper bound $r_g^{\max}(\xi)$ saturates to 1. Here we have stated an approximate version of $r_g^{\max}$ that was derived in ref. [83] in the limit $\xi \ll \xi_0$. We provide the formula compatible with the NNLL transition point below in eq. (2.18). We also see that for $\xi < 1$, $r_g^{\min}(\xi) < r_g^{\max}(\xi)$.

2.2 Effective theory regions

The measurement of jet mass, groomed jet radius and application of soft drop introduce several energy scales which can become hierarchical in certain regions of the ξ-r_g phase space and consequently induce logarithmic singularities. We now list down the various regions that require a specialized effective field theory based treatment.

We first consider the single differential groomed jet mass measurement and enumerate the various factorization regimes that are relevant.

1. *Fixed order region*: This corresponds to the region when $\xi \lesssim 1$. Here the fixed order treatment of the (groomed) jet mass differential cross section suffices.

2. *Plain jet mass resummation region*: This is the region where $\xi_0 < \xi \ll 1$. Here $\xi \ll 1$ implies that the jet mass m_J is hierarchically smaller than the hard scale Q. This results in dominance of the soft-collinear modes leading to Sudakov double logarithms, $\alpha_s^n \ln^k \xi$, with $k \leq 2n$. This region can be described by the standard soft-collinear Sudakov factorization for plain jet mass. The condition that $\xi > \xi_0$ implies that effects of grooming alone can be treated in fixed order perturbation theory.

3. *Soft drop resummation region:* As we discussed above, the effects of grooming on the spectrum become visible for $\xi < \xi_0$. When we move to yet lower jet masses for $\xi \ll \xi_0$, additional logarithms related to soft drop involving the ratio ξ/ξ_0 become large and require resummation. This results in an additional factorization of the soft radiation beyond the one mentioned above in plain jet mass resummation.

Next, as discussed in ref. [83], three different effective theory regimes related to simultaneous measurement of r_g and ξ arise:[7]

1. *Max-R_g regime*: In this region the groomed jet radius is close to the maximum possible value, such that

$$\text{Max-}R_g \text{ regime:} \qquad r_g^{\min}(\xi) \ll r_g \lesssim r_g^{\max}(\xi) \,. \qquad (2.19)$$

As we will see below, the factorization in this regime is identical to that of the single differential groomed jet mass, and the additional measurement of r_g can be treated as a fixed order correction. Note that unlike ref. [83] we do not impose an additional constraint of $r_g^{\max}(\xi) \ll 1$ and also include the situation $r_g^{\max}(\xi) \lesssim 1$ which arises in the plain jet mass region.

We also note that this regime is also relevant for the leading hadronization corrections. Here the collinear-soft modes that pass grooming lie at maximal possible angular separation from the collinear core, and hence the leading two-pronged configurations relevant for eq. (1.3) arise specifically in this regime.

2. *Intermediate-R_g regime*: This regime is relevant when the groomed jet radius is hierarchically separated from both minimum and maximum kinematic bounds:

$$\text{Intermediate-}R_g \text{ regime:} \qquad r_g^{\min}(\xi) \ll r_g \ll r_g^{\max}(\xi) \,. \qquad (2.20)$$

Depending on the precise values of the hard scale and grooming parameters, this regime may or may not be relevant. However, because of the two hierarchies, describing this regime leads to the most factorized version of the doubly differential cross section. As a result, the intermediate regime cross section can be used as an efficient tool to subtract the singular pieces and define a stable prescription for incorporating fixed order power corrections in the entire double differential spectrum.

3. *Min-R_g regime:* This regime arises when the groomed jet radius is close to the lower bound:

$$\text{Min-}R_g \text{ regime:} \qquad r_g^{\min}(\xi) \lesssim r_g \ll r_g^{\max}(\xi) \,. \qquad (2.21)$$

This physically corresponds to a scenario where the jet is filled uniformly with hard collinear radiation, with a haze of soft radiation at the same angular scales. If we fix the r_g and vary the jet mass, this region in fact corresponds to the end-point of the jet

---

[7]In ref. [83] these regimes were respectively referred to as large-R_g, intermediate-R_g and small-R_g cases. We avoid using labels 'small' and 'large' to avoid any confusion related to numerical size of R_g.
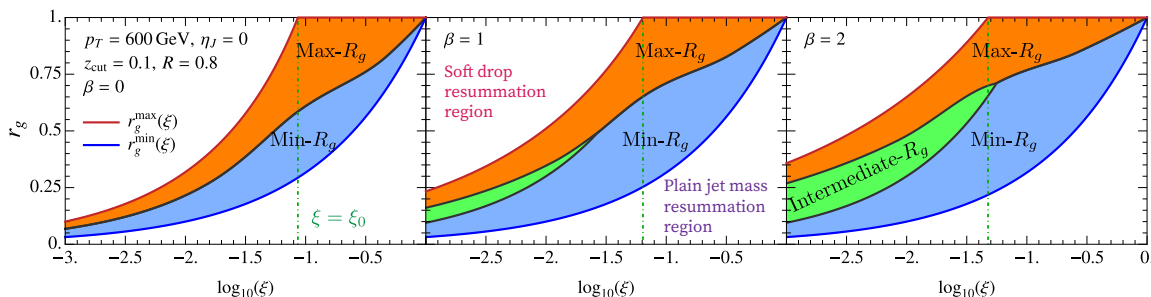
Figure 3. Three regimes relevant for doubly differential groomed jet radius and groomed jet mass measurement for $\beta = 0, 1, 2$. The region to the left of the vertical line $\xi = \xi_0$ is the soft drop resummation region, and to the right is the plain jet mass resummation region. The boundaries of the shaded region denote the kinematic bounds imposed on groomed jet radius by the jet mass measurement. Depending on the values of grooming parameters, a third intermediate-R_g regime can become relevant.

mass spectrum. For this reason, the factorization in this regime has resemblance with the fixed-order region of the singly differential jet mass spectrum. This feature of this regime was utilized in ref. [55] for incorporating jet mass related power corrections in the single differential jet mass spectrum.

We show the various regimes discussed above in figure 3 for jets with LHC kinematics and $\beta = 0$ and $\beta = 1$. The vertical line at $\xi = \xi_0$ separates the soft drop and plain jet mass resummation regions. The boundary of the colored region is the kinematic bound on r_g given in eq. (2.18). We see that for $\beta = 0$, the intermediate-R_g regime is absent whereas this regime covers a substantial phase space for $\beta = 2$ in the soft drop resummation region. The precise formulae for demarcating these regions are discussed in section 5 and appendix C.

2.3 Effective theory modes

From above discussion we learn that there are two jet mass regions and three regimes corresponding to groomed jet radius measurements that require resummation. It is instructive to represent the measurements and the modes in the (primary) Lund plane of a soft/collinear emission off the jet-initiating fast parton as shown in figure 4. Here z is the momentum fraction of the emission and θ is the angle it makes relative to the jet axis. The choice of axes in figure 4 implies that emissions to the right are increasingly collinear and those higher are increasingly softer. These schematic figures are extremely useful in identifying the relevant effective theory modes that appear at the intersections of various measurements and constraints imposed on the jet.

We first describe how various measurements are displayed in figure 4. The black vertical line labeled $\theta = R$ denotes the boundary of the jet and the gray region corresponds to radiation outside the jet. Emissions on the blue line with negative slope labeled $p^+ Q = m_J^2$ contribute (in combination with the fast massless jet-initiating parton) jet mass of m_J^2. Thus, increasing the jet mass corresponds to moving this line downwards. The soft drop condition is given by the dashed black line with positive slope. The groomed jet radius measurement is given by the orange vertical line labeled $\theta = R_g$. Emissions that are vetoed
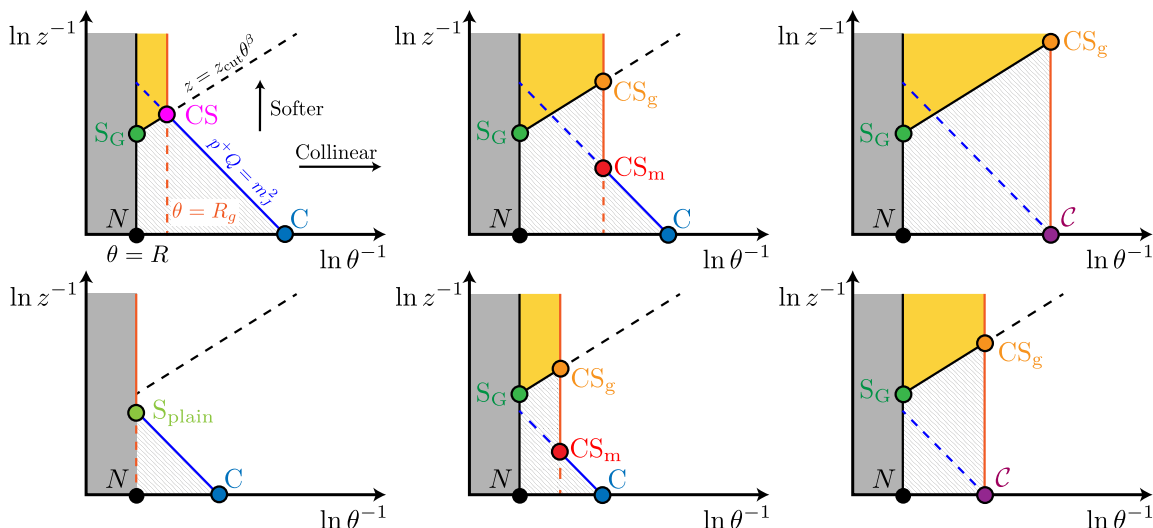
Figure 4. Effective theory modes appearing in various regimes for double differential measurement. The solid yellow shaded region is where radiation is groomed away. The rectangular gray region corresponds to radiation falling outside the jet. The hatched region is the radiation vetoed by combination of grooming, jet mass and groomed jet radius measurements. The top row corresponds to the jet masses in the soft drop resummation region where as the bottom row describes scenarios in the plain jet mass resummation region.

by soft drop are the ones that are encountered at angles larger than R_g and are shown in yellow shaded region. Hence, the columns from left to right correspond to max-R_g, intermediate-R_g and min-R_g regimes respectively. Finally, a given jet mass and groomed jet radius measurement (along with jet radius and soft drop constraints) excludes any emissions that are harder shown in the hatched region. The cases in the top row where the jet mass lies in the soft drop resummation region were already considered in ref. [83]. The cases in the bottom row are new and correspond to larger jet masses in the plain jet mass resummation region. In the bottom left plot we show the completely ungroomed case when the $R_g = R$. However, this plot also includes the scenario where $R_g \lesssim R$, and where the effects of soft drop do not require any further factorization.

We notice that the relevant EFT modes appear at the intersections of two or more measurement or veto conditions.

1. *Collinear modes*: Modes on the x-axis represent collinear radiation with $z \sim 1$ emitted by the fast parton at the core of the jet. In the scenarios there is a softer radiation at wider angles that stops the groomer, the jet mass measurement imposed on the collinear radiation at the center of the jet is essentially inclusive denoted by C. On the other hand, (hard-)collinear modes denoted by N and $\mathcal{C}$ respectively see the jet radius and groomed jet radius boundary.

2. *Wide-angle soft modes*: Modes at wider angles on the y-axis will naturally encounter the groomer first. For jet masses in the top row of figure 4, the radiation at the jet-boundary must necessarily be groomed away, else we would have found a larger

Mode	Description	Scaling
N	Hard-collinear mode at jet boundary	$Q(1, 1, 1)$
$\mathcal{C}$	Hard-collinear mode within R_g	$Qr_g(r_g, \frac{1}{r_g}, 1)$
C	Collinear mode for inclusive jet mass	$Q\sqrt{\xi}\left(\sqrt{\xi}, \frac{1}{\sqrt{\xi}}, 1\right)$
S_{plain}	Wide-angle soft	$Q\xi(1, 1, 1)$
S_G	Global soft	$Q_{\text{cut}}(1, 1, 1)$
CS_g	Collinear-soft mode for groomed jet radius	$Q_{\text{cut}}r_g^{1+\beta}(r_g, \frac{1}{r_g}, 1)$
CS_m	Collinear-soft mode for jet mass	$\frac{Q\xi}{r_g}(r_g, \frac{1}{r_g}, 1)$
CS	Collinear-soft mode at maximum R_g	$\frac{Q\xi}{r_g^{\text{max}}(\xi)}\left(r_g^{\text{max}}(\xi), \frac{1}{r_g^{\text{max}}(\xi)}, 1\right)$

Table 1. Scalings of various modes for soft drop double differential cross section following the light cone decomposition in eq. (2.9). Including jet radius related factors in the reference light cone vectors results in hemisphere-jets like kinematics. The third argument also indicates the virtuality of these modes.

value of the jet mass. The physics associated with this radiation can be factorized in the soft drop resummation region when $\xi \ll \xi_0$ described by the global soft mode S_G. On the other hand, in the plain jet mass region, for $r_g \lesssim 1$, the wide angle radiation is energetic enough to pass soft drop and thus we do not encounter this mode, as shown in the bottom left case. Here, the wide angle mode S_{plain} is the same as in the plain jet mass resummation. These two modes only differ in their relative energy and the combination of measurements and vetoes they see.

3. *Collinear-soft modes*: Finally, we have modes that have simultaneously $z \ll 1$ and $\theta \ll 1$. These collinear soft modes are distinguished from each other via the role they play in the entire measurement. The CS mode is the same as that appears in the single differential jet mass measurement in the soft drop resummation region. It has the largest possible angle and energies to saturate the soft drop condition. When $r_g < r_g^{\text{max}}(\xi)$, we denote the soft radiation that stops soft drop as CS_g. However, as we can see CS_g mode does not carry sufficient energy to result in the jet mass shown. Thus we include another mode CS_m which lies at similar angular scales but is more energetic as required by the jet mass measurement.

The momentum scaling of various modes in the light cone coordinates in eq. (2.9) are shown in table 1.

3 One-loop results of factorization functions

Before we state the factorization formulae for each of the cases discussed above, we first perform one-loop calculations of the corresponding soft and collinear factorization functions

to gain familiarity with the details of measurements associated with each of the modes in figure 4. We first set up a convenient notation to express one-loop phase space integrals in section 3.1 and review the known factorization functions results in section 3.2. In section 3.3 we describe computation of new factorization functions associated with modes in max-R_g and also compute the fixed order non-singular corrections.

3.1 Matrix elements and measurement functions

At $\mathcal{O}(\alpha_s)$, the jet initating parton i^* splits as $i^* \to jk$. It will prove useful parameterize the light cone coordinates in the decomposition in eq. (2.9) in terms of dimensionless numbers:

$$
\text{Soft functions :} \qquad y \equiv \frac{q_j^+}{Q}, \qquad x \equiv \frac{q_j^-}{Q}, \tag{3.1}
$$

$$
\text{Collinear functions :} \qquad y \equiv \frac{p_{i^*}^2}{Q^2}, \qquad x \equiv \frac{q_j^-}{Q},
$$

where j is the softer of the two final state partons. Here $p_{i^*}^2 = s = (p_j + p_k)^2$. All the soft functions associated with the wide-angle soft and collinear-soft modes involve the same eikonal matrix element with a single-particle phase space, whereas those associated with collinear modes involve the full splitting functions and two-particle phase space. For a generic observable $\mathcal{O}$ including any veto conditions Θ, the corresponding soft and collinear functions renormalized in $\overline{\text{MS}}$-scheme at $\mathcal{O}(\alpha_s)$ are then given by

$$
\mathcal{J}_\kappa^{[1]}(\mathcal{O}, \delta_\mathcal{O}, \mu) \equiv \frac{\alpha_s}{2\pi} \frac{e^{\epsilon \gamma_E}}{\Gamma(1-\epsilon)} \left(\frac{\mu^2}{Q^2} \right)^\epsilon \int_0^1 \frac{\mathrm{d}x\, \mathrm{d}y}{y^{1+\epsilon}[x(1-x)]^\epsilon} \delta_\mathcal{O}[\hat{\mathcal{O}}(x,y), \hat{\Theta}(x,y)] \sum_{\kappa'} \hat{P}_{\kappa'\kappa}(x),
$$

$$
\mathcal{S}_\kappa^{[1]}(\mathcal{O}, \delta_\mathcal{O}, \mu) \equiv \frac{\alpha_s C_\kappa}{\pi} \frac{e^{\epsilon \gamma_E}}{\Gamma(1-\epsilon)} \left(\frac{\mu^2}{Q^2} \right)^\epsilon \int_0^\infty \frac{\mathrm{d}x\, \mathrm{d}y}{(xy)^{1+\epsilon}} \delta_\mathcal{O}[\hat{\mathcal{O}}^{(s,cs)}(x,y), \hat{\Theta}^{(s,cs)}(x,y)], \tag{3.2}
$$

where $\delta_\mathcal{O}$ combines the measurement and veto conditions on the two parton system and also includes the virtual contribution. We have suppressed dependence on kinematic and grooming parameters for simplicity. The splitting functions are given by

$$
\hat{P}_{gq}(x) = C_F \left[\frac{1 + (1-x)^2}{x} - \epsilon x \right],
$$

$$
\hat{P}_{gg}(x) = C_A \left[\frac{x}{1-x} + \frac{1-x}{x} + x(1-x) \right],
$$

$$
\hat{P}_{qg}(x) = n_f T_F \left[x^2 + (1-x)^2 - 2\epsilon x(1-x) \right]. \tag{3.3}
$$

In the soft matrix elements, we additionally take soft or collinear-soft limit of the observable and the veto condition as indicated by the superscript (s, cs):

$$
\text{Soft limit :} \qquad x \to 0, \qquad x \sim y, \tag{3.4}
$$

$$
\text{Collinear-soft limit :} \qquad x \to 0, \qquad \frac{y}{x} \to 0.
$$

Thus, factorization functions associated with various modes differ only in the details of the measurement and veto conditions and some of the modes may only involve veto

conditions. For the cases we are interested in, we will only consider the jet mass measurement, which is the same for both collinear and soft matrix elements, and is simply given by

$$\hat{\xi}(x, y) = y .\tag{3.5}$$

Next, we have the jet radius, groomed jet radius and soft drop constraints. The jet radius constraint corresponds to the k_T clustering condition:

$$\hat{\Theta}_{k_T}(x, y) \equiv \Theta\big(x(1 - x) - y\big) .\tag{3.6}$$

Note that the jet radius does not explicitly appear in the above constraint as we have absorbed the factor ζ defined in eq. (2.8) in the definitions of the light cone coordinates. Similarly, it is easy to check the condition that the two partons are within the groomed jet radius is given by

$$\hat{\Theta}_{r_g}(x, y, r_g) \equiv \Theta\big(r_g^2 x(1 - x) - y\big) .\tag{3.7}$$

Finally, the full soft drop condition in eq. (2.10) in terms of the variables x and y is given by

$$\hat{\Theta}_{\rm sd}(x, y, \xi_0, \zeta) = \Theta\bigg(\frac{\min\{x_1, x_2\}}{x_1 + x_2} - \xi_0 \Big(\frac{y}{4 x_1 x_2} \Big)^{\frac{\beta}{2}} \bigg) ,\tag{3.8}$$

where

$$x_1(x, y) = \frac{xy\zeta^2}{2} + \frac{1 - x}{2} , \qquad x_2(x, y) = \frac{(1 - x)y\zeta^2}{2} + \frac{x}{2} ,\tag{3.9}$$

and we have suppressed dependence on β for simplicity.

The corresponding soft and collinear-soft limit of these results read:

soft particle clustered with the jet: $\qquad \hat{\Theta}_{k_T}^{(s,cs)}(x, y) \quad \equiv \Theta(x - y) ,$ (3.10)

soft emission at an angle $< r_g$: $\qquad \hat{\Theta}_{r_g}^{(s,cs)}(x, y, r_g) \equiv \Theta(r_g^2 x - y) ,$

collinear-soft emission passes soft drop: $\hat{\Theta}_{\rm sd}^{(cs)}(x, y, \xi_0) \quad \equiv \Theta\Big(x - y^{\frac{\beta}{2+\beta}} \xi_0^{\frac{2}{2+\beta}} \Big) .$

soft emission passes soft drop: $\qquad \hat{\Theta}_{\rm sd}^{(s)}(x, y, \xi_0, \zeta) \equiv \Theta\Big(x + y\zeta^2 - y^{\frac{\beta}{2+\beta}} \xi_0^{\frac{2}{2+\beta}} \Big) ,$

Having compiled the various measurement and veto functions, we now describe how they are combined in the functions $\delta_{\mathcal{O}}$ appearing in eq. (3.2).

3.2 Compilation of known results

We first review the known results of factorization functions.

3.2.1 Hard-collinear radiation outside the jet

We first state the normalization contribution of the hard-collinear near the boundary of the jet as calculated in refs. [55, 96]:

$$N_{\rm incl}^q(Q, \mu) = 1 + \frac{\alpha_s(\mu) C_F}{2\pi} \bigg\{ -\frac{1}{2} \ln^2 \frac{\mu^2}{Q^2} - \frac{3}{2} \ln \frac{\mu^2}{Q^2} - \frac{13}{2} + \frac{3\pi^2}{4} \bigg\} ,\tag{3.11}$$

$$N_{\rm incl}^g(Q, \mu) = 1 + \frac{\alpha_s(\mu)}{2\pi} \bigg\{ -\frac{C_A}{2} \ln^2 \frac{\mu^2}{Q^2} - \frac{\beta_0}{2} \ln \frac{\mu^2}{Q^2} + C_A \Big(-\frac{5}{12} + \frac{3\pi^2}{4} \Big) - \frac{23}{12} \beta_0 \bigg\} .$$

3.2.2 Inclusive jet mass measurement on collinear radiation

We now consider the simplest case of inclusive ungroomed jet mass, which is relevant for the collinear mode C in the max- and intermediate-R_g cases. Here the measurement function is given by

$$\delta_\xi^C(x, y) = \delta(\xi - y) - \delta(y) \,, \tag{3.12}$$

such that using eq. (3.2) the inclusive jet function at NLO is given by

$$J_\kappa^{[1]}(m_J^2, \mu) = \delta(m_J^2) + \frac{1}{Q^2} \mathcal{J}_\kappa^{[1]}\left(\xi = \frac{m_J^2}{Q^2}, \delta_\xi^C, \mu\right) + \mathcal{O}(\alpha_s^2) \,. \tag{3.13}$$

We have expressed the jet function in terms of its natural argument, and will do the same for all the factorization functions below. The results read [97, 98]

$$J_q(m_J^2, \mu) = \delta(m_J^2) + \frac{\alpha_s(\mu) C_F}{\pi} \left(\mathcal{L}_1(m_J^2, \mu^2) - \frac{6}{8} \mathcal{L}_0(m_J^2, \mu^2) - \frac{\delta(m_J^2)}{4}\left(\pi^2 - 7\right) \right) \,, \tag{3.14}$$

$$\begin{aligned} J_g(m_J^2, \mu) = \delta(m_J^2) + \frac{\alpha_s(\mu)}{\pi} \Bigg(&\frac{C_A}{\pi} \mathcal{L}_1(m_J^2, \mu^2) - \frac{\beta_0}{4} \mathcal{L}_0(m_J^2, \mu^2) \\ &+ \frac{\delta(m_J^2)}{36}\Big(C_A(67 - 9\pi^2) - 20 n_F T_R \Big) \Bigg) \,, \end{aligned}$$

where $\mathcal{L}_n$ is the standard plus function:

$$\mathcal{L}_n(\ell^+, \mu) \equiv \frac{1}{\mu} \mathcal{L}_n\left(\frac{\ell^+}{\mu}\right) \,. \tag{3.15}$$

For later use we also state the result for the Laplace transform defined by

$$\tilde{J}_\kappa(x, \mu) \equiv \int_0^\infty \mathrm{d}m_J^2 \, e^{-x m_J^2} \, J_\kappa(m_J^2, \mu) \,, \tag{3.16}$$

such that

$$\tilde{J}_q(x, \mu) = 1 + \frac{\alpha_s C_F}{\pi} \left[\frac{1}{2} \log^2\left(x \, \mu^2 e^{\gamma_E}\right) + \frac{3}{4} \log\left(x \, \mu^2 e^{\gamma_E}\right) + \frac{7}{4} - \frac{\pi^2}{6} \right] \,, \tag{3.17}$$

$$\tilde{J}_g(x, \mu) = 1 + \frac{\alpha_s}{\pi} \left[\frac{C_A}{2} \log^2\left(x \, \mu^2 e^{\gamma_E}\right) + \frac{\beta_0}{4} \log\left(x \mu^2 e^{\gamma_E}\right) + C_A\left(\frac{67}{36} - \frac{\pi^2}{6}\right) - n_F T_R \frac{5}{9} \right] \,.$$

3.2.3 Hard-collinear radiation within groomed jet radius

Next, we turn to the hard-collinear mode $\mathcal{C}$ which involves an additional constraint of groomed jet radius with jet mass measurement:

$$\delta_\xi^{\mathcal{C}}(x, y, r_g) \equiv \hat{\Theta}_{r_g}(x, y, r_g)\left[\delta(\xi - y) - \delta(\xi)\right] \,, \tag{3.18}$$

where $\hat{\Theta}_{r_g}$ was defined in eq. (3.7). The corresponding collinear function is then given by

$$\mathcal{C}^\kappa(\xi, r_g, Q, \mu) \equiv \frac{1}{r_g^2} \mathcal{C}^\kappa\left(\frac{\xi}{r_g^2}, Q r_g, \mu\right) = \delta(\xi) + \mathcal{J}_\kappa^{[1]}(\xi, \delta_\xi^{\mathcal{C}}, \mu) + \mathcal{O}(\alpha_s^2) \,, \tag{3.19}$$

with explicit expressions of the function with three arguments being [55, 83],

$$
\mathcal{C}^q(\xi, Q, \mu) = \delta(\xi) + \frac{\alpha_s(\mu) C_F}{\pi} \left\{ \delta(\xi) \left(\frac{1}{4} \ln^2 \frac{\mu^2}{Q^2} + \frac{3}{4} \ln \frac{\mu^2}{Q^2} + \frac{7}{4} - \frac{5\pi^2}{24} \right) \right.
$$
$$
\left. + \Theta(1 - 4\xi) \left[- \mathcal{L}_1(\xi) + \mathcal{L}_0(\xi) \left(2\ln \left(\frac{1 + \sqrt{1 - 4\xi}}{2} \right) - \frac{3}{4} \sqrt{1 - 4\xi} \right) \right] \right\},
$$

$$
\mathcal{C}^g(\xi, Q, \mu) = \delta(\xi) + \frac{\alpha_s(\mu)}{\pi} \left\{ \delta(\xi) \left(\frac{C_A}{4} \ln^2 \frac{\mu^2}{Q^2} + \frac{\beta_0}{4} \ln \frac{\mu^2}{Q^2} + C_A \left(\frac{67}{36} - \frac{5\pi^2}{24} \right) - \frac{5}{9} n_f T_F \right) \right.
$$
$$
+ \Theta(1 - 4\xi) \left[- C_A \mathcal{L}_1(\xi) + \mathcal{L}_0(\xi) \left(2C_A \log \left(\frac{1 + \sqrt{1 - 4\xi}}{2} \right) \right. \right.
$$
$$
\left. \left. \left. - \frac{\beta_0}{4} \sqrt{1 - 4\xi} + \frac{C_A - 2n_f T_F}{6} \xi \sqrt{1 - 4\xi} \right) \right] \right\}.
$$

3.2.4 Collinear-soft radiation within groomed jet radius

We now consider soft functions and consider the simplest case of CS_m mode with jet mass measurement and groomed jet radius boundary. The measurement function is simply a soft limit of the previous case and is defined as:

$$
\delta_\xi^{\mathrm{CS}_m}(x, y, r_g) \equiv \hat{\Theta}_{r_g}^{(cs)}(x, y, r_g) \left[\delta(x - y) - \delta(\xi) \right], \tag{3.21}
$$

with the corresponding function given by

$$
S_{c_m}^\kappa \left(\frac{\ell^+}{r_g}, \mu \right) = \delta \left(\frac{\ell^+}{r_g} \right) + \frac{1}{Q} \mathcal{S}_\kappa^{[1]} \left(\xi = \frac{\ell^+}{Q}, \delta_\xi^{\mathrm{CS}_m}, \mu \right) + \mathcal{O}(\alpha_s^2), \tag{3.22}
$$

which yields

$$
S_{c_m}^\kappa \left(\frac{\ell^+}{r_g}, \mu \right) = \delta \left(\frac{\ell^+}{r_g} \right) + \frac{\alpha_s C_\kappa}{2\pi} \left[-4\mathcal{L}_1 \left(\frac{\ell^+}{r_g}, \mu \right) + \frac{\pi^2}{12} \delta \left(\frac{\ell^+}{r_g} \right) \right]. \tag{3.23}
$$

We next define the Laplace transform:

$$
\tilde{S}_{c_m}(u, \mu) \equiv \int_0^\infty \mathrm{d}\ell^+ \, e^{-u\ell^+} S_{c_m}^\kappa(\ell^+, \mu), \tag{3.24}
$$

which yields

$$
\tilde{S}_{c_m}^\kappa [u, \mu] = 1 + \frac{\alpha_s C_\kappa}{\pi} \left[-\log^2 \left(u e^{\gamma_E} \mu \right) - \frac{\pi^2}{8} \right]. \tag{3.25}
$$

3.2.5 Wide-angle soft radiation failing soft drop

The next case we consider is the global soft modes S_G that fail soft drop. Here we only have a veto condition and no measurement:

$$
\hat{\Theta}^{S_G}(x, y, \xi_0, \zeta) \equiv \hat{\Theta}_{k_T}^{(s)}(x, y) \left(1 - \hat{\Theta}_{\mathrm{sd}}^{(s)}(x, y, \xi_0, \zeta) \right), \tag{3.26}
$$

such that

$$S_G^\kappa(Q_{\rm cut}, \zeta, \beta, \mu) = 1 + \mathcal{S}_\kappa^{[1]}(\,\cdot\,, \hat{\Theta}^{S_G}, \mu) + \mathcal{O}(\alpha_s^2)\,. \tag{3.27}$$

Here the empty slot in the first argument simply denotes that the function has no differential measurement applied on it and only contributes to the normalization. At one-loop the result reads [24, 95]

$$S_G^\kappa(Q_{\rm cut}, \zeta, \beta, \mu) = 1 + \frac{\alpha_s(\mu) C_\kappa}{\pi}\left[\frac{1}{(1+\beta)}\log^2\left(\frac{\mu}{Q_{\rm cut}}\right) - \frac{\pi^2}{24}\left(\frac{1}{1+\beta}\right) \right.$$
$$\left. - \frac{(2+\beta)}{4}\left(2{\rm Li}_2\left[\frac{\zeta^2}{1+\zeta^2}\right] + \log^2\left[1+\zeta^2\right]\right)\right]\,. \tag{3.28}$$

Note that the above global soft function is really only valid for inclusive jets measurement. For exclusive measurements, one additionally needs to include contributions from the beam region and other trigger jets. However, as detailed in ref. [55], the above result is nevertheless useful in the case of exclusive jets with an appropriate treatment of the quark-gluon fractions.

3.2.6 Collinear-soft radiation at intermediate groomed jet radius

Analogous to above, we consider the case of CS_g modes that pass soft drop and are within the required groomed jet radius, but do not contribute to the jet mass measurement:

$$\hat{\Theta}^{CS_g}(x, y, r_g, \xi_0) \equiv \hat{\Theta}_{r_g}^{(cs)}(x, y, r_g)\hat{\Theta}_{\rm sd}^{(cs)}(x, y, \xi_0)\,. \tag{3.29}$$

The corresponding function being

$$S_{c_g}^\kappa(Q_{\rm cut} r_g^{1+\beta}, \beta) = 1 + \mathcal{S}_\kappa^{[1]}(\,\cdot\,, \hat{\Theta}^{CS_g}, \mu) + \mathcal{O}(\alpha_s^2)\,. \tag{3.30}$$

While formally in eq. (3.29) we are required to take the collinear-soft limit of the soft drop constraint, we will also find it useful to employ the results of intermediate-R_g regime for implementing fixed-order subtractions. To this end, it is helpful to evaluate the above function in the soft-wide angle limit, for which we can directly recycle the computation of the previous result of global soft function (while being careful about minus signs):

$$S_{c_g}^\kappa(Q_{\rm cut} r_g^{1+\beta}, \zeta_g, \beta) = 1 - \frac{\alpha_s(\mu) C_\kappa}{\pi}\left[\frac{1}{(1+\beta)}\log^2\left(\frac{\mu}{Q_{\rm cut} r_g^{1+\beta}}\right) - \frac{\pi^2}{24}\left(\frac{1}{1+\beta}\right)\right.$$
$$\left. - \frac{(2+\beta)}{4}\left(2{\rm Li}_2\left[\frac{\zeta_g^2}{1+\zeta_g^2}\right] + \log^2\left[1+\zeta_g^2\right]\right)\right]\,. \tag{3.31}$$

Here we have defined a variable ζ_g analogous to ζ defined above in eq. (2.8)

$$\zeta_{g,{\rm incl}}^{pp} \equiv \frac{R_g}{2\cosh\eta_J}\,, \qquad \zeta_{g,{\rm excl}}^{pp} \equiv 1\,, \qquad \zeta_{g,{\rm incl}}^{e^+e^-} \equiv \tan\frac{R_g}{2}\,. \tag{3.32}$$

3.3 One-loop results in max-R_g and fixed-order regime

We now state results for the remaining functions that are relevant for max-R_g regimes. Some of the results below have already been calculated elsewhere but only after expanding in $r_g \ll 1$ limit, and we reinstate the full r_g dependence at $\mathcal{O}(\alpha_s)$.

3.3.1 Widest angle collinear soft radiation passing soft drop

We consider the CS mode that saturates the kinematic constraints imposed by jet mass measurement and soft drop passing condition. Here we have

$$\delta_\xi^{\mathrm{CS}}(x,y,r_g,\xi_0) \equiv \hat{\Theta}_{\mathrm{sd}}^{(cs)}(x,y,\xi_0)\big[\hat{\Theta}_{r_g}^{(cs)}(x,y,r_g)\delta(\xi-y) - \delta(\xi)\big] \tag{3.33}$$

This condition can be straightforwardly obtained by demanding that modes that pass soft drop are also required to satisfy the groomed jet radius constraint. On the other hand, modes that fail soft drop and the virtual piece, however, do not see this constraint. The collinear-soft function is then given by

$$S_c^\kappa(\tilde{k},r_g,Q_{\mathrm{cut}},\beta,\mu) \equiv \delta(\tilde{k}) + \frac{1}{QQ_{\mathrm{cut}}^{\frac{1}{1+\beta}}}\mathcal{S}_\kappa^{[1]}\left(\xi=\frac{\tilde{k}}{QQ_{\mathrm{cut}}^{\frac{1}{1+\beta}}},\delta_\xi^{\mathrm{CS}},\mu\right) + \mathcal{O}(\alpha_s^2). \tag{3.34}$$

Note that we have made use of a $\frac{2+\beta}{1+\beta}$ dimensional variable which appears as the natural argument for this function. It will be helpful to split the measurement in eq. (3.33) as

$$\delta_\xi^{\mathrm{CS}}(x,y,r_g,\xi_0) = \hat{\Theta}_{\mathrm{sd}}^{(cs)}(x,y,\xi_0)\big[\delta(\xi-y) - \delta(\xi)\big] + \Delta\delta_{\xi,r_g}^{\mathrm{CS}}(x,y,r_g,\xi_0), \tag{3.35}$$

where

$$\Delta\delta_{\xi,r_g}^{\mathrm{CS}}(x,y,r_g,\xi_0) \equiv -(1-\hat{\Theta}_{r_g}^{(cs)}(x,y,r_g))\hat{\Theta}_{\mathrm{sd}}^{(cs)}(x,y,\xi_0)\delta(\xi-y), \tag{3.36}$$

such that the first term simply results in the standard collinear-soft function for single differential jet mass, and the second piece in a finite fixed order correction:

$$S_c^\kappa(\tilde{k},r_g,Q_{\mathrm{cut}},\beta,\mu) = S_c^\kappa(\tilde{k},\beta,\mu) + \Delta S_{r_g}^\kappa(\tilde{k},r_g,Q_{\mathrm{cut}},\beta,\alpha_s(\mu)), \tag{3.37}$$

where [24] (see also ref. [55])

$$S_c^\kappa(\tilde{k},\beta,\mu) = \delta(\tilde{k}) + \frac{\alpha_s C_\kappa}{\pi}\left[\frac{-2(1+\beta)}{2+\beta}\mathcal{L}_1\left(\tilde{k},\mu^{\frac{2+\beta}{1+\beta}}\right) + \frac{\pi^2}{24}\frac{2+\beta}{1+\beta}\delta(\tilde{k})\right]. \tag{3.38}$$

Here the dependence on Q_{cut} drops out as it is a high scale from the perspective of low energy collinear-soft modes. The Laplace transform is defined by

$$\tilde{S}_c^\kappa(s,\beta,\mu) \equiv \int \mathrm{d}\tilde{k}\,e^{-s\tilde{k}}S_c^\kappa(\tilde{k},\beta,\mu), \tag{3.39}$$

such that

$$\tilde{S}_c^\kappa(s) = 1 + \frac{\alpha_s C_\kappa}{\pi}\left[-\left(\frac{1+\beta}{2+\beta}\right)\log^2\left(se^{\gamma_E}\mu^{\frac{2+\beta}{1+\beta}}\right) - \frac{\pi^2}{24}\frac{\beta(3\beta+4)}{(1+\beta)(2+\beta)}\right]. \tag{3.40}$$

Next we turn to the finite correction $\Delta S_{r_g}^\kappa$ that describes fixed-order corrections due to r_g measurement and re-introduces dependence on $Q_{\rm cut}$. This correction was evaluated in ref. [83] in the $r_g \ll 1$ limit. Since we are also interested in covering the region close to the soft drop cusp, where $r_g \lesssim 1$, we will find it helpful for the purposes of matching to include the full jet radius dependence by employing the soft-wide angle limit of the soft drop constraint $\hat{\Theta}_{\rm sd}^{(s)}$ in eq. (3.33) and including jet radius constraint $\hat{\Theta}_{k_T}^{(s)}$, such that we use in eq. (3.35)

$$\Delta\delta_{\xi,r_g}^{\rm CS,full}(x,y,r_g,\xi_0,\zeta) \equiv -\hat{\Theta}_{k_T}^{(s)}(x,y)\big(1-\hat{\Theta}_{r_g}^{(s)}(x,y,r_g)\big)\hat{\Theta}_{\rm sd}^{(s)}(x,y,\xi_0,\zeta)\delta(\xi-y)\,, \quad (3.41)$$

which yields the correction piece

$$Q_{\rm cut}^{\frac{1}{1+\beta}}\Delta S_{r_g}^\kappa\Big(\ell^+ Q_{\rm cut}^{\frac{1}{1+\beta}},r_g,Q_{\rm cut},\zeta,\beta,\alpha_s(\mu)\Big) = \frac{1}{Q}\mathcal{S}_\kappa^{[1]}\Big(\xi=\frac{\ell^+}{Q},\Delta\delta_{\xi,r_g}^{\rm CS,full},\mu\Big) \qquad (3.42)$$

$$= \frac{\alpha_s C_\kappa}{\pi}\frac{\Theta(\ell^+ - Q_{\rm cut}'v(r_g))}{\ell^+}\left[\ln(r_g^2) + \Theta(Q_{\rm cut}'-\ell^+)\ln\bigg(\Big(\frac{Q_{\rm cut}}{\ell^+}\Big)^{\frac{2}{2+\beta}}-\zeta^2\Big)\right]\,,$$

where we have defined

$$v(r_g) \equiv \left(\frac{1+\zeta^2}{\frac{1}{r_g^2}+\zeta^2}\right)^{\frac{2+\beta}{2}}\,, \qquad (3.43)$$

and have expressed the result in terms of $\ell^+ Q_{\rm cut}^{\frac{1}{1+\beta}}$ due to explicit $Q_{\rm cut}$ dependence from constraining r_g. We had defined $Q_{\rm cut}'$ in eq. (2.14). We can check that by setting ζ to zero, we recover the result in the soft drop resummation region ($\xi < \xi_0$) calculated in ref. [83]:

$$Q_{\rm cut}^{\frac{1}{1+\beta}}\Delta S_{r_g}^\kappa\Big(\ell^+ Q_{\rm cut}^{\frac{1}{1+\beta}} < Q_{\rm cut}^{\frac{2+\beta}{1+\beta}},r_g,Q_{\rm cut},\zeta=0,\beta,\alpha_s(\mu)\Big) \qquad (3.44)$$

$$= \frac{-2}{2+\beta}\frac{\alpha_s C_\kappa}{\pi}\Theta\left(\frac{\ell^+}{Q_{\rm cut}}-r_g^{2+\beta}\right)\frac{1}{\ell^+}\log\left(\frac{\ell^+}{Q_{\rm cut}r_g^{2+\beta}}\right)\,.$$

We thus see that including soft-wide angle effects modify the transition point from $Q_{\rm cut}$ to $Q_{\rm cut}'$.

3.3.2 Wide-angle soft radiation in plain jet mass region

We now consider the final case where the wide-angle soft mode $S_{\rm plain}$ is tested for soft drop, jet radius constraints with jet mass measurement. This is relevant for the max-R_g regime in the plain jet mass resummation region. The measurement function is given by

$$\delta_\xi^{S_{\rm plain}}(x,y,r_g,\xi_0,\zeta) \equiv \hat{\Theta}_{k_T}^{(s)}(x,y)\hat{\Theta}_{\rm sd}^{(s)}(x,y,\xi_0,\zeta)\big[\hat{\Theta}_{r_g}^{(s)}(x,y,r_g)\delta(\xi-y)-\delta(\xi)\big] \qquad (3.45)$$

This expression is a simple extension of eq. (3.33) where we have also included the jet radius constraint. We will find it helpful to split the measurement into chunks that we have already encountered:

$$\delta_\xi^{S_{\rm plain}}(x,y,r_g,\xi_0,\zeta) = \delta_\xi^{{\rm CS}_m}(x,y,1) + \Delta\delta_{\xi,r_g}^{\rm CS,full}(x,y,r_g,\xi_0,\zeta) + \Delta\delta_{\xi,\rm sd}^{S_{\rm plain}}(x,y,\xi_0,\zeta)\,.$$

$$(3.46)$$

In the first term on the right hand side, setting $r_g = 1$ in eq. (3.21) results in the same jet radius constraint, and hence is simply the familiar ungroomed soft function. The second piece accounts for the cumulative measurement of groomed jet radius using eq. (3.41). Finally, the new piece accounts for effects of soft drop on wide-angle soft modes:

$$\Delta\delta_{\xi,\,\mathrm{sd}}^{S_{\mathrm{plain}}}(x,y,\xi_0,\zeta) = -\hat{\Theta}_{k_T}^{(s)}(x,y)\big(1 - \hat{\Theta}_{\mathrm{sd}}^{(s)}(x,y,\xi_0,\zeta)\big)\big[\delta(\xi - y) - \delta(\xi)\big]. \qquad (3.47)$$

Hence, the soft function in the plain jet mass region is given by

$$S_{\mathrm{plain}}^{\kappa}(\ell^+, r_g, Q_{\mathrm{cut}}, \zeta, \beta, \mu) = \delta(\ell^+) + \frac{1}{Q}\mathcal{S}_\kappa^{[1]}\bigg(\xi = \frac{\ell^+}{Q}, \delta_\xi^{S_{\mathrm{plain}}}, \mu\bigg) + \mathcal{O}(\alpha_s^2) \qquad (3.48)$$

$$= S_{c_m}^{\kappa}(\ell^+, \mu) + Q_{\mathrm{cut}}^{\frac{1}{1+\beta}}\Delta S_{r_g}^{\kappa}\bigg(\ell^+ Q_{\mathrm{cut}}^{\frac{1}{1+\beta}}, r_g, Q_{\mathrm{cut}}, \zeta, \beta, \alpha_s(\mu)\bigg) + \Delta S_{\mathrm{sd}}^{\kappa}(\ell^+, Q_{\mathrm{cut}}, \beta, \zeta, \alpha_s(\mu)),$$

where we have written the result in terms of previous results in eqs. (3.23) and (3.42) and a new piece given by [55]

$$\Delta S_{\mathrm{sd}}^{\kappa}(\ell^+, Q_{\mathrm{cut}}, \zeta, \beta, \alpha_s(\mu)) = \frac{1}{Q}\mathcal{S}_\kappa^{[1]}\bigg(\xi = \frac{\ell^+}{Q}, \Delta\delta_{\xi,\,\mathrm{sd}}^{S_{\mathrm{plain}}}, \mu\bigg) \qquad (3.49)$$

$$= -\frac{\alpha_s(\mu)C_\kappa}{\pi}\left[\frac{\Theta(\ell^+)\Theta(Q'_{\mathrm{cut}} - \ell^+)}{\ell^+}\ln\bigg(\Big(\frac{Q_{\mathrm{cut}}}{\ell^+}\Big)^{\frac{2}{2+\beta}} - \zeta^2\bigg)\right]_+^{[Q'_{\mathrm{cut}}]}.$$

Here the plus-function with a non-standard boundary condition is defined as

$$[\Theta(x)q(x)]_+^{[x_0]} \equiv \lim_{\epsilon \to 0}\bigg(\Theta(x - \epsilon)q(x) - \delta(x - \epsilon)\int_\epsilon^{x_0}\mathrm{d}x'\,q(x')\bigg). \qquad (3.50)$$

We also note that for functions satisfying $q(x) = \lambda^\alpha g(\lambda^{-1}x)$ we have,

$$[\Theta(x)q(x)]_+^{[x_0]} = \lambda^\alpha\big[\Theta(\lambda^{-1}x)g(\lambda^{-1}x)\big]_+^{[\lambda^{-1}x_0]}. \qquad (3.51)$$

This property proves useful in simplifying expressions involving integrals of such plus-functions.

3.3.3 Fixed-order cross section

We now turn to the fixed order cross section. Here the measurement function is same as eq. (3.45) without any expansions:

$$\delta_\xi^{\mathrm{FO}}(x,y,r_g,\xi_0,\zeta) \equiv \hat{\Theta}_{k_T}(x,y)\hat{\Theta}_{\mathrm{sd}}(x,y,\xi_0,\zeta)\big[\hat{\Theta}_{r_g}(x,y,r_g)\delta(\xi - y) - \delta(\xi)\big], \qquad (3.52)$$

and the fixed order cross section is given by

$$\mathcal{G}_{\kappa,\mathrm{sd}}^{\mathrm{FO}}(\xi, r_g, \xi_0, \zeta, \alpha_s(\mu)) = \mathcal{J}^{[1]}(\xi, \delta_\xi^{\mathrm{FO}}, \mu) + \mathcal{O}(\alpha_s^2). \qquad (3.53)$$

Because of the complicated form of the full soft drop condition in eq. (3.8) we will evaluate this numerically. To this end, we define a subtraction term with the measurement function,

$$\delta_\xi^{\mathrm{FO}(0)}(x,y,r_g,\xi_0,\zeta) \equiv \hat{\Theta}_{k_T}(x,y)\hat{\Theta}_{\mathrm{sd}}^{(s)}(x,y,\xi_0,\zeta)\big[\hat{\Theta}_{r_g}(x,y,r_g)\delta(\xi - y) - \delta(\xi)\big], \qquad (3.54)$$

where we have now replaced full soft drop constraint by its soft limit in eq. (3.10), and evaluate the following function numerically by implementing subtraction at the level of the integrand:

$$\Delta\mathcal{G}_{\kappa,\mathrm{sd}}^{\mathrm{FO}[1]}(\xi, r_g, \xi_0, \zeta, \alpha_s(\mu)) = \mathcal{G}_{\kappa,\mathrm{sd}}^{\mathrm{FO}}(\xi, r_g, \xi_0, \zeta, \alpha_s(\mu)) - \mathcal{G}_{\kappa,\mathrm{sd}}^{\mathrm{FO}(0)}(\xi, r_g, \xi_0, \zeta, \alpha_s(\mu)). \quad (3.55)$$

The soft matrix element corresponding to this measurement is given by

$$\tilde{\mathcal{G}}_{\kappa,\mathrm{sd}}^{\mathrm{FO}(0)}(\xi, r_g, \xi_0, \zeta, \alpha_s(\mu)) \equiv \mathcal{S}_\kappa^{[1]}(\xi, \delta_\xi^{\mathrm{FO}(0)}, \mu) + \mathcal{O}(\alpha_s^2), \quad (3.56)$$

such that we have

$$\xi\tilde{\mathcal{G}}_{q,\mathrm{sd}}^{\mathrm{FO}(0)}(\xi, r_g, \xi_0, \zeta, \alpha_s(\mu)) = \frac{\alpha_s(\mu)C_F}{\pi}\ln\left(\frac{\frac{1}{2}\left(1 + \sqrt{1 + 4\xi/r_g^2}\right)}{\max\left\{\frac{1}{2}\left(1 - \sqrt{1 + 4\xi/r_g^2}\right), \xi_0^{\frac{2}{2+\beta}} y^{\frac{\beta}{2+\beta}} - y\zeta^2\right\}}\right),$$

$$\xi\tilde{\mathcal{G}}_{g,\mathrm{sd}}^{\mathrm{FO}(0)}(\xi, r_g, \xi_0, \zeta, \alpha_s(\mu)) = \frac{\alpha_s(\mu)C_A}{\pi}\ln\left(\frac{1/2}{\max\left\{\frac{1}{2}\left(1 - \sqrt{1 + 4\xi/r_g^2}\right), \xi_0^{\frac{2}{2+\beta}} y^{\frac{\beta}{2+\beta}} - y\zeta^2\right\}}\right).$$

$$(3.57)$$

Since we are interested in the differential cross section we can restrict to $\xi > 0$ by multiplying by ξ and avoid considering the zero-bin terms.

4 Factorization and resummation

Having discussed the mode structure, we now state the factorization formulae for the three regimes discussed here [83]. In section 4.1 we describe the factorization formula for max-R_g regime, and review min and intermediate R_g regimes in section 4.2.

4.1 Max-R_g regime

We first consider the max-R_g regime in the plain jet mass region and identify the resummation kernels associated with the one-loop results calculated in section 3.3.

4.1.1 Max-R_g in plain jet mass resummation region

We recall the discussion in section 2.1 where in eq. (2.2) we showed how in the small jet mass region the inclusive jet function factorizes, which can be formulated in terms of an RG invariant jet mass distribution for a jet flavor κ in eq. (2.4). We will see that the various cases we consider below for $\xi \ll 1$ will differ only in the details of the multi-scale $\mathcal{J}_\kappa$ function describing soft collinear dynamics. We will treat the non-global logarithms at NLL accuracy where they can be factorized. Next, in the ungroomed region the soft drop condition and measurement of the groomed jet radius are accounted for via fixed order corrections, and hence the factorization and resummation proceeds precisely the same way as the ungroomed jet mass case. This is given by the bottom left scenario in figure 4

involving the hard collinear modes N, the (inclusive) collinear modes C and the wide angle soft modes S_{plain}. The factorized cross section is given by

$$\mathcal{G}_{\kappa}^{\text{plain}}(z,\xi,r_g,\mu) = \sum_{\kappa'} \mathcal{H}_{\kappa'\to\kappa}(z,Q,\mu)\frac{\text{d}}{\text{d}\xi}\left[\mathcal{S}_{\text{NGL}}^{\kappa}(t[\xi Q,Q])\Sigma_{\text{plain}}^{\kappa}(\xi,r_g,Q,Q_{\text{cut}},\zeta,\mu)\right], \quad (4.1)$$

where we have suppressed dependence on kinematic and grooming parameters in $\mathcal{G}_{\kappa}^{\text{plain}}$. As shown in eq. (2.2), this factorization involves the same hard collinear function $\mathcal{H}_{\kappa'\to\kappa}$. The jet mass measurement with cumulative r_g cut off is described by the derivative of the cumulative cross section:

$$\Sigma_{\text{plain}}^{\kappa}(\xi,r_g,Q,Q_{\text{cut}},\zeta,\mu) = \int_0^{\infty} \text{d}s\,\text{d}\ell_c^+ \, J_{\kappa}(s,\mu)\mathcal{S}_{\text{plain}}^{\kappa}(\ell_c^+,r_g,Q_{\text{cut}},\zeta,\beta,\mu)\delta\left(\xi-\frac{s}{Q^2}-\frac{\ell_c^+}{Q}\right), \tag{4.2}$$

where $\mathcal{S}_{\text{plain}}^{\kappa}$ is the cumulative version of the wide-angle soft function in eq. (3.48).

$$\mathcal{S}_{\text{plain}}^{\kappa}(\ell_c^+,r_g,Q_{\text{cut}},\zeta,\beta,\mu) \equiv \int_0^{\ell_c^+} \text{d}\ell^+ \, S_{\text{plain}}^{\kappa}(\ell^+,r_g,Q_{\text{cut}},\zeta,\beta,\mu). \tag{4.3}$$

The $\mathcal{S}_{\text{NGL}}^{\kappa}$ accounts for non-global logarithms up to NLL accuracy, and the argument is defined as

$$t[\mu_0,\mu_1] \equiv \frac{1}{2\pi} \int_{\mu_0}^{\mu_1} \frac{d\mu'}{\mu'} \, \alpha_s(\mu'). \tag{4.4}$$

From eq. (4.2) we see that the NGLs depend on the integral of running coupling between wide-angle soft and hard-collinear scales.

Finally, we point out that factorizing the cross section in eq. (4.2) amounts to dropping the following power corrections:

$$\mathcal{G}_{\kappa}(z,\xi,r_g,\alpha_s(\mu)) = \mathcal{G}_{\kappa}^{\text{plain}}(z,\xi,r_g,\mu)\Big(1+\mathcal{O}(\xi_0,\xi)\Big), \tag{4.5}$$

where the left hand side is the full QCD cross section which only depends on running coupling at a single scale μ. In the resummed version of the factorized cross section we will employ separate jet mass and groomed jet radius dependent profile scales for each of the factorization functions. In addition to the $\mathcal{O}(\xi)$ jet mass power corrections mentioned above, we have also dropped the finite-z_{cut} terms of $\mathcal{O}(\xi_0)$.

We now describe the resummation using the renormalization group evolution of the functions appearing in factorization formula above. We will consider the normalized cross section $\tilde{\mathcal{G}}_{\kappa}^{\text{plain}}$ defined in eq. (2.4) after stripping off the DGLAP evolution. We will find it helpful to isolate the fixed-order corrections in $S_{\text{plain}}^{\kappa}$ in eq. (3.48) and decompose $\tilde{\mathcal{G}}_{\kappa}^{\text{plain}}$ as

$$\tilde{\mathcal{G}}_{\kappa}^{\text{plain}}(\xi,r_g,Q,Q_{\text{cut}},\zeta,\mu_{\text{plain}}) = \tilde{\mathcal{G}}_{\kappa,\text{no sd}}^{\text{plain}}(\xi,Q,\mu_{\text{plain}}) + \Delta\tilde{\mathcal{G}}_{\kappa}^{\text{plain}}(\xi,r_g,Q,Q_{\text{cut}},\zeta,\mu_{\text{plain}}). \tag{4.6}$$

Instead of a single scale μ, we employ here a set of scales μ_{plain} for plain jet mass resummation that minimize the logs in each factorization function:

$$\mu_{\text{plain}} \equiv \{\mu_N, \mu_J(\xi), \mu_s(\xi)\}. \tag{4.7}$$

Precise implementation of these scales was discussed extensively in refs. [55, 83]. We summarize the formulae for these scales and their variations in appendix B.

The first of these is the resummed ungroomed cross section given by

$$\tilde{\mathcal{G}}^{\text{plain}}_{\kappa,\text{no sd}}(\xi, Q, \mu_{\text{plain}}) = N^\kappa_{\text{incl}}(Q, \mu_N) e^{K_N} \Big(\frac{\mu_N}{Q}\Big)^{\omega_N} \mathcal{J}^{\text{plain}}_{\kappa,\text{no sd}}(\xi, Q, \mu_{\text{plain}}), \qquad (4.8)$$

where K_N and ω_N are resummation kernels associated with the hard collinear function N^κ_{incl}. We follow a shorthand throughout this paper

$$K_\mathcal{F} \equiv j_\mathcal{F} K\big(\Gamma_\mathcal{F}[\alpha_s], \mu, \mu_\mathcal{F}\big) + \eta\big(\gamma_\mathcal{F}[\alpha_s], \mu, \mu_\mathcal{F}\big), \qquad \omega_\mathcal{F} \equiv \eta(\Gamma_\mathcal{F}[\alpha_s], \mu, \mu_\mathcal{F}), \qquad (4.9)$$

where $K_\mathcal{F}$ and $\omega_\mathcal{F}$ are resummation kernels associated with any factorization function $\mathcal{F}$, $j_\mathcal{F}$ is the dimension of the argument of the function such as $m_J^2 (j_\mathcal{F} = 2)$, $\ell^+ (j_\mathcal{F} = 1)$, $\tilde{k}(j_\mathcal{F} = \frac{2+\beta}{1+\beta})$, $\mu_\mathcal{F}$ is the choice of scale used to minimize the logs and μ is the final scale up to which the function is RG evolved (which we will leave unspecified). The functions $K(\Gamma, \mu, \mu_\mathcal{F})$ and $\eta(\Gamma, \mu, \mu_\mathcal{F})$ are responsible for implementing single and double logarithmic resummation associated with cusp $\Gamma_\mathcal{F}$ and non-cusp $\gamma_\mathcal{F}$ anomalous dimensions of the functions. The formulae for these kernels were described in detail in appendix A of ref. [83]. In appendix A we state the anomalous dimensions required for NNLL resummation.

The function $\mathcal{J}^{\text{plain}}_{\kappa,\text{no sd}}$ accounts for the remaining soft and collinear pieces:

$$\mathcal{J}^{\text{plain}}_{\kappa,\text{no sd}}(\xi, Q, \mu_{\text{plain}}) = \frac{\text{d}}{\text{d}\xi}\Big(\mathcal{S}^\kappa_{\text{NGL}}(t[Q\xi, Q]) \, \Sigma^\kappa_{\text{no sd}}(\xi, Q, \mu_{\text{plain}})\Big), \qquad (4.10)$$

where $\Sigma^\kappa_{\text{no sd}}$ is defined analogously to Σ_{plain} in eq. (4.2):

$$\Sigma^\kappa_{\text{no sd}}(\xi, Q, \mu) = \int \text{d}s \int \text{d}\ell^+_c \, J_\kappa(s, \mu) \, \mathcal{S}^\kappa_{c_m}(\ell^+_c, \mu) \, \delta\Big(\xi - \frac{s}{Q^2} - \frac{\ell^+}{Q}\Big), \qquad (4.11)$$

and similar to eq. (4.3), $\mathcal{S}^\kappa_{c_m}$ is the cumulative version of the S_{c_m} soft function defined in eq. (3.22). Making the RG evolution in eq. (4.10) explicit, we have

$$\mathcal{J}^{\text{plain}}_{\kappa,\text{no sd}}(\xi, Q, \mu_{\text{plain}}) = \Bigg(\mathcal{S}^\kappa_{\text{NGL}}(t[Q\xi, Q]) \mathcal{J}^{\text{plain}}_\kappa[\partial_\Omega; \xi, Q, \mu_{\text{plain}}] \frac{e^{\gamma_E \Omega}}{\Gamma(-\Omega)} \qquad (4.12)$$

$$+ \Big(\frac{\text{d}}{\text{d}\ln\xi} \mathcal{S}^\kappa_{\text{NGL}}(t[Q\xi, Q])\Big) \mathcal{J}^\kappa_{\text{plain}}[\partial_\Omega; \xi, Q, \mu_{\text{plain}}] \frac{e^{\gamma_E \Omega}}{\Gamma(1-\Omega)} \Bigg)\Bigg|_{\Omega = \tilde{\omega}_{cs_m}(\mu_s, \mu_J)},$$

where Ω is evaluated at

$$\tilde{\omega}_{cs_m}(\mu_s, \mu_J) \equiv \omega_{cs_m}(\mu, \mu_s) + \omega_J(\mu, \mu_J), \qquad (4.13)$$

and the function of the derivative operator is given by

$$\mathcal{J}^{\text{plain}}_\kappa[\partial_\Omega; \xi, Q, \mu_{\text{plain}}] \equiv \frac{1}{\xi} e^{K_J + K_s} \frac{(Q\mu_s)^{\omega_s}(\mu_J^2)^{\omega_J}}{(\xi Q^2)^\Omega}$$

$$\times \tilde{J}_\kappa\Big[\partial_\Omega + \log\Big(\frac{\mu_J^2}{Q^2 \xi}\Big), \alpha_s(\mu_J)\Big] \tilde{S}^\kappa_{c_m}\Big[\partial_\Omega + \log\Big(\frac{\mu_s}{Q\xi}\Big), \alpha_s(\mu_s)\Big]. \quad (4.14)$$

Here $\tilde{J}_\kappa$ and $\tilde{S}^\kappa_{c_m}$ are the Laplace transforms of the jet and ungroomed soft function, and we have written them in a notation that makes the logarithms explicit:

$$\tilde{J}_\kappa\big[\log(e^{\gamma_E}x\mu_J^2), \alpha_s(\mu_J)\big] \equiv \tilde{J}_\kappa(x, \mu_J)\,, \tag{4.15}$$

$$\tilde{S}^\kappa_{c_m}\Big[\log\big(u e^{\gamma_E}\mu_s\big), \alpha(\mu_s)\Big] \equiv \tilde{S}^\kappa_{c_m}(u, \mu_s)\,.$$

We now turn to the remaining piece in eq. (4.6). Since this term involves fixed order terms that are not related to a boundary condition of the RG evolution, they have to be treated differently, and result in the formula

$$\Delta\tilde{\mathcal{G}}^{\text{plain}}_\kappa(\xi, r_g, Q, Q_{\text{cut}}, \zeta, \mu_{\text{plain}}) = N^\kappa_{\text{incl}}(Q, \mu_N) e^{K_N}\Big(\frac{\mu_N}{Q}\Big)^{\omega_N} \tag{4.16}$$

$$\times \Bigg(\mathcal{S}^\kappa_{\text{NGL}}(t[Q\xi, Q])\, \mathcal{J}^{\text{plain}}_\kappa[\partial_\Omega; \xi, Q, \mu_{\text{plain}}]\, \mathcal{Q}^{\text{plain}}_\kappa(\Omega, \xi, r_g, \alpha_s(\mu_s))$$

$$+ \Big(\frac{\mathrm{d}}{\mathrm{dln}\xi}\mathcal{S}^\kappa_{\text{NGL}}(t[Q\xi, Q])\Big)\mathcal{J}^{\text{plain}}_\kappa[\partial_\Omega; \xi, Q, \mu_{\text{plain}}]\,\mathcal{Q}^{\text{plain}}_\kappa(\Omega-1, \xi, r_g, \alpha_s(\mu_s))\Bigg)\Bigg|_{\Omega=\tilde{\omega}(\mu_s,\mu_J)}.$$

where the kernel $\mathcal{Q}^{\text{plain}}_\kappa$ is defined as Laplace transform of the fixed order soft function terms and convolved with RG resummation kernels:

$$\mathcal{Q}^{\text{plain}}_\kappa \equiv \mathcal{Q}^{\text{sd}}_\kappa(\Omega, \xi, \alpha_s(\mu)) + \mathcal{Q}^{r_g}_\kappa(\Omega, \xi, r_g, \alpha_s(\mu); a^{\text{max}}_{20}) + \mathcal{Q}^{(\text{sd}, r_g)}_\kappa(\Omega, \xi, r_g, \alpha_s(\mu))\,. \tag{4.17}$$

The first two terms in eq. (4.17) involve the $\mathcal{O}(\alpha_s)$ soft function pieces in eqs. (3.42) and (3.49):

$$\mathcal{Q}^{\text{sd}}_\kappa(\Omega, \xi, \alpha_s(\mu)) \equiv \frac{e^{\gamma_E\Omega}}{\Gamma(-\Omega)}\int_0^\infty \mathrm{d}\ell^+\,\mathcal{L}^{-\Omega}_0\Big(1-\frac{\ell^+}{Q\xi}\Big)\Delta S^\kappa_{\text{sd}}(\ell^+, Q_{\text{cut}}, \zeta, \beta, \alpha_s(\mu))\,,$$

$$\mathcal{Q}^{r_g}_\kappa(\Omega, \xi, r_g, \alpha_s(\mu); a^{\text{max}}_{20}) \equiv \frac{e^{\gamma_E\Omega}}{\Gamma(-\Omega)}\int_0^\infty \mathrm{d}\ell^+\,\mathcal{L}^{-\Omega}_0\Big(1-\frac{\ell^+}{Q\xi}\Big)\Big(1+\frac{\alpha_s(\mu_{cs})}{\pi}a^{\text{max}}_{20}\Big)$$

$$\times Q^{\frac{1}{1+\beta}}_{\text{cut}}\Delta S^\kappa_{r_g}\Big(Q^{\frac{1}{1+\beta}}_{\text{cut}}\ell^+, r_g, Q_{\text{cut}}, \zeta, \beta, \alpha_s(\mu)\Big)\,, \tag{4.18}$$

and the third is an $\mathcal{O}(\alpha_s^2)$ cross term:

$$\mathcal{Q}^{(\text{sd}, r_g)}_\kappa(\Omega, \xi, r_g, Q_{\text{cut}}, \zeta, \beta, \alpha_s(\mu)) \equiv \frac{e^{\gamma_E\Omega}}{\Gamma(-\Omega)}\int_0^\infty \mathrm{d}\ell^+_1\,\mathrm{d}\ell^+_2\,\mathcal{L}^{-\Omega}_0\Big(1-\frac{\ell^+_1+\ell^+_2}{Q\xi}\Big) \tag{4.19}$$

$$\times \Delta S^\kappa_{\text{sd}}(\ell^+_1, Q_{\text{cut}}, \zeta, \beta, \alpha_s(\mu))\, Q^{\frac{1}{1+\beta}}_{\text{cut}}\Delta S^\kappa_{r_g}\Big(Q^{\frac{1}{1+\beta}}_{\text{cut}}\ell^+_2, r_g, Q_{\text{cut}}, \zeta, \beta, \alpha_s(\mu)\Big)\,.$$

Here we have defined

$$\mathcal{L}^a_0(x) \equiv \mathcal{L}^a(x) + \frac{1}{a}\delta(x)\,, \qquad \mathcal{L}^a(x) \equiv \Big[\frac{\Theta(x)}{x^{1-a}}\Big]_+\,, \qquad a \neq 0\,, \tag{4.20}$$

and case with $\Omega = 0$ corresponds to turning off resummation:

$$\lim_{\Omega\to 0}\frac{e^{\gamma_E\Omega}}{\Gamma(-\Omega)}\mathcal{L}^{-\Omega}_0(x) = \delta(x)\,. \tag{4.21}$$

We note that the r_g-dependence in the cross section in the plain jet mass region arises at $\mathcal{O}(\alpha_s)$ through the fixed order correction $\Delta S^\kappa_{r_g}$ in eq. (3.42). However, as mentioned above, $\Delta S^\kappa_{r_g}$ itself cannot provide the $\mathcal{O}(\alpha_s)$ boundary condition for NLL evolution (and for NNLL accuracy). Hence, as discussed in ref. [83], we are required to consider cross terms with between $\mathcal{O}(\alpha_s)$ pieces in $\mathcal{J}^{\text{plain}}_\kappa$ and the normalization factor N^κ_{incl}, and the r_g-dependent piece in eq. (3.42). We will see that the same applies to the cross section in the soft drop resummation region. On the other hand, the role of the piece $\Delta S^\kappa_{\text{sd}}$ in eq. (3.49) is to account for effects of grooming on the soft drop jet mass which factorize into global-soft and collinear-soft pieces in the soft drop resummation region. As we will see below, we are required to include the cross term $\mathcal{Q}^{(\text{sd},r_g)}_\kappa$ in eq. (4.19) in order to ensure that the $\mathcal{O}(\alpha_s^2)$ terms in the plain jet mass region consistently match with $\mathcal{O}(\alpha_s^2)$ pieces in the soft drop resummation region. Finally, the computation of these kernels and others below is detailed in section 6.4.

We note that unlike ref. [83], we have chosen not to include additional $\mathcal{O}(\alpha_s^2)$ terms proportional to β_0 in order to cancel running coupling effects in these kernels and render them μ-independent. We have retained for simplicity only the minimal set of $\mathcal{O}(\alpha_s^2)$ terms required to achieve NNLL accuracy, and parameterized uncertainty due to the missing $\mathcal{O}(\alpha_s^2)$ corrections in terms of the nuisance parameter a^{max}_{20} in eq. (4.18). We assume that the missing two-loop pieces in eq. (4.17) have the same functional form as the one-loop kernels with an unknown normalization parameterized by $a^{\text{max}}_{20} \in [-2\pi, 2\pi]$. Additionally, we will separately consider below the effects of two-loop logarithmic terms that arise from RG evolution.

4.1.2 Max-R_g in soft drop resummation region

In the soft drop resummation region, the relevant modes are shown in the top left case in figure 4. The factorized cross section reads

$$\mathcal{G}^{\text{sd res.}}_\kappa(z, \xi, r_g, \mu) = \sum_{\kappa'} \mathcal{H}_{\kappa' \to \kappa}(z, Q, \mu) S^\kappa_G(Q_{\text{cut}}, \zeta, \beta, \mu) \mathcal{S}^\kappa_{\text{NGL}}(t[Q_{\text{cut}}, Q]) \tag{4.22}$$

$$\times \int \mathrm{d}\tilde{k} \int \mathrm{d}s\, J_\kappa(s, \mu) S^\kappa_c(\tilde{k}, r_g, Q_{\text{cut}}, \beta, \mu) \delta\left(\xi - \frac{s}{Q^2} - \frac{\tilde{k}(Q_{\text{cut}})^{\frac{-1}{1+\beta}}}{Q}\right).$$

This involves the global-soft and c-soft functions we discussed above in eqs. (3.27) and (3.34). The NGLs are now independent of jet mass involving constant scales Q_{cut} and Q, such that we are able to write it directly as differential in groomed jet mass. The power corrections associated with this factorization are given by

$$\mathcal{G}_\kappa(z, \xi, r_g, \alpha_s(\mu)) = \mathcal{G}^{\text{sd res.}}_\kappa(z, \xi, r_g, \mu)\left[1 + \mathcal{O}\left(\xi_0, \frac{\xi}{r_g^2}, \left(\frac{\xi}{\xi_0}\right)^{\frac{2}{2+\beta}}\right)\right]. \tag{4.23}$$

We see that the jet mass related $\mathcal{O}(\xi)$ power corrections in the plain jet mass region are now replaced by $\mathcal{O}(\xi/r_g^2)$, due to modification of the effective jet radius seen by collinear modes. In the plain jet mass region with $r_g = 1$, these corrections match with those in eq. (4.5).

Additionally, we have new power corrections related to soft drop that have resulted in the factorization of the wide-angle soft mode into a global soft and c-soft mode.

Next we state the resummed formula for this regime for the jet mass dependent part of $\mathcal{G}_\kappa$:

$$\tilde{\mathcal{G}}_\kappa^{\text{sd res.}}(\xi, r_g, Q, Q_{\text{cut}}, \zeta, \beta, \mu_{\text{sd}}) = N_\kappa^{\text{evol}}(\mu_N, \mu_{gs}, Q, Q_{\text{cut}}, \zeta, \beta)\mathcal{S}_{\text{NGL}}^\kappa(t[Q_{\text{cut}}, Q]) \tag{4.24}$$

$$\times \mathcal{J}_\kappa^{\text{sd res}}[\partial_\Omega; \xi, Q, Q_{\text{cut}}, \mu_{\text{sd}}]\left(\frac{e^{\gamma_E \Omega}}{\Gamma(-\Omega)} + \mathcal{Q}_\kappa^{r_g}(\Omega, \xi, r_g, \alpha_s(\mu_{cs}); a_{20}^{\max})\right)\Bigg|_{\Omega = \tilde{\omega}_{cs}(\mu_{cs}, \mu_J)}.$$

Here μ_{sd} stands for the set of scales in the max-R_g regime in the soft drop resummation region:

$$\mu_{\text{sd}}(\xi) \equiv \{\mu_N, \mu_{gs}, \mu_J(\xi), \mu_{cs}(\xi)\}. \tag{4.25}$$

The normalization factor N_κ^{evol} includes resummation of logarithms between the hard-collinear and global-soft scales:

$$N_\kappa^{\text{evol}}(\mu_N, \mu_{gs}, Q, Q_{\text{cut}}, \zeta, \beta) \equiv N_{\text{incl}}^\kappa(Q, \mu_N)S_G^\kappa(Q_{\text{cut}}, \zeta, \beta, \mu_{gs}) \tag{4.26}$$

$$\times e^{\left[K_N + K_{gs}\right]}\left(\frac{\mu_N}{Q}\right)^{\omega_N}\left(\frac{\mu_{gs}}{Q_{\text{cut}}}\right)^{\omega_{gs}}.$$

The function of the derivative operator is given by

$$\mathcal{J}_\kappa^{\text{sd res}}[\partial_\Omega; \xi, Q, Q_{\text{cut}}, \mu_{\text{sd}}] \equiv \frac{1}{\xi}\,e^{K_{cs}+K_J}\frac{(\mu_J^2)^{\omega_J}(Q\mu_{cs})^{\omega_{cs}}}{(\xi Q^2)^\Omega}\left(\left(\frac{\mu_{cs}}{Q_{\text{cut}}}\right)^{\frac{1}{1+\beta}}\right)^{\omega_{cs}} \tag{4.27}$$

$$\times \tilde{J}_\kappa\left[\partial_\Omega + \log\left(\frac{\mu_J^2}{Q^2\xi}\right), \alpha_s(\mu_J)\right]\tilde{S}_c^\kappa\left[\partial_\Omega + \log\left(\frac{\mu_{cs}}{Q\xi}\left(\frac{\mu_{cs}}{Q_{\text{cut}}}\right)^{\frac{1}{1+\beta}}\right), \alpha_s(\mu_{cs})\right],$$

where the Laplace transforms are written analogously to eq. (4.15). Similar to eq. (4.13), the derivatives are evaluated at $\tilde{\omega}_{cs}(\mu_{cs}, \mu_J)$ defined as

$$\tilde{\omega}_{cs}(\mu_{cs}, \mu_J) \equiv \omega_{cs}(\mu, \mu_{cs}) + \omega_J(\mu, \mu_J). \tag{4.28}$$

Finally, as in eq. (4.16), we expand the above equation to $\mathcal{O}(\alpha_s^2)$ including cross terms between $\mathcal{J}_\kappa^{\text{sd res}}$ and the same kernel $\mathcal{Q}_\kappa^{r_g}$ defined in eq. (4.18) required for NNLL accuracy.

4.2 Min and intermediate R_g regimes

For completeness we review the factorization formulae for the remaining min and intermediate R_g regimes derived in ref. [83].

4.2.1 Min-R_g regime

We now turn to the min-R_g regime. As seen in the rightmost column in figure 4, the cross section in the min-R_g regime involves combination of the hard collinear $\mathcal{C}$ mode, the collinear soft mode CS_g and the global soft mode S_G, and is given by

$$\mathcal{G}_\kappa^{\min}(z, \xi, r_g, \mu) = \sum_{\kappa'}\mathcal{H}_{\kappa' \to \kappa}(z, Q, \mu)S_G^\kappa(Q_{\text{cut}}, \zeta, \beta, \mu)\mathcal{S}_{\text{NGL}}^\kappa(t[Q_{\text{cut}}, Q]) \tag{4.29}$$

$$\times S_{c_g}^\kappa(Q_{\text{cut}}r_g^{1+\beta}, \beta, \mu)\mathcal{S}_{\text{NGL}}^\kappa\left(t[Q_{\text{cut}}r_g^{1+\beta}, Qr_g]\right)\frac{1}{r_g^2}\mathcal{C}^\kappa\left(\frac{\xi}{r_g^2}, Qr_g, \mu\right).$$

Here we notice appearance of new NGLs between the scales associate with CS_g and $\mathcal{C}$ modes due to an additional boundary of the groomed jet radius. The power corrections that are dropped in this formula are given by

$$\mathcal{G}_\kappa\big(z,\xi,r_g,\alpha_s(\mu)\big) = \mathcal{G}_\kappa^{\min}(z,\xi,r_g,\mu)\left[1 + \mathcal{O}\left(\xi_0, \left(\frac{\xi}{\xi_0}\right)^{\frac{2}{2+\beta}}, r_g^{2+\beta}\frac{\xi_0}{\xi}\right)\right]. \qquad (4.30)$$

As before, the soft drop factorization proceeds by dropping the $\mathcal{O}((\xi/\xi_0)^{\frac{2}{2+\beta}})$ power corrections. In contrast with the max-R_g regime in eqs. (4.5) and (4.23) collinear function now includes the $\mathcal{O}(\xi/r_g^2)$ terms which become $\mathcal{O}(1)$ in this regime. However, in order to resum logarithms between scales associated with CS_g and $\mathcal{C}$ modes, the power corrections of the form $r_g^{2+\beta}\frac{\xi_0}{\xi}$ are dropped.

The resummed result for the normalized cross section is given by

$$\tilde{\mathcal{G}}_\kappa^{\min}(\xi,r_g,Q,Q_{\text{cut}},\zeta,\beta,\mu_{\min}) = N_\kappa^{\text{evol}}\big(\mu_N,\mu_{gs},Q,Q_{\text{cut}},\zeta,\beta\big)\mathcal{S}_{\text{NGL}}^\kappa\big(t[Q_{\text{cut}},Q]\big) \qquad (4.31)$$

$$\times \mathcal{S}_{\text{NGL}}^\kappa\Big(t[Q_{\text{cut}}r_g^{1+\beta},Qr_g]\Big)e^{K_\mathcal{C}+K_{cs_g}}\left(\frac{\mu_{gs}}{Q_{\text{cut}}r_g^{1+\beta}}\right)^{\omega_{cs_g}}\left(\frac{\mu_\mathcal{C}}{Qr_g}\right)^{\omega_\mathcal{C}}$$

$$\times S_{c_g}^\kappa(Q_{\text{cut}}r_g^{1+\beta},\beta,\mu_{cs_g})\frac{1}{r_g^2}\mathcal{C}^\kappa\left(\frac{\xi}{r_g^2},Qr_g,\mu_\mathcal{C};a_{20}^{\min}\right),$$

with the set of profiles for this regimes being:

$$\mu_{\min}(r_g) \equiv \{\mu_N, \mu_{gs}, \mu_\mathcal{C}(r_g), \mu_{cs_g}(r_g)\}. \qquad (4.32)$$

Here we have included additional $\mathcal{O}(\alpha_s^2)$ terms in the collinear function precisely as described in ref. [83]:

$$\frac{\xi}{r_g^2}\mathcal{C}^q\left(\frac{\xi}{r_g^2},Qr_g,\mu;a_{20}^{\min}\right) = \frac{\alpha_s}{\pi}a_{10}^{\mathcal{C}_q}\left(\frac{\xi}{r_g^2}\right)\left[1 + \frac{\alpha_s C_F}{\pi}\left(\frac{1}{4}\ln^2\frac{\mu^2}{Q^2r_g^2} + \frac{3}{4}\ln\frac{\mu^2}{Q^2r_g^2}\right)\right] \qquad (4.33)$$

$$+ \frac{\alpha_s}{\pi}a_{20}^{\min}\frac{\alpha_s}{\pi}a_{10}^{\mathcal{C}_q}\left(\frac{16}{25}\frac{\xi}{r_g^2}\right),$$

$$\frac{\xi}{r_g^2}\mathcal{C}^g\left(\frac{\xi}{r_g^2},Qr_g,\mu;a_{20}^{\min}\right) = \frac{\alpha_s}{\pi}a_{10}^{\mathcal{C}_g}\left(\frac{\xi}{r_g^2}\right)\left[1 + \frac{\alpha_s}{\pi}\left(\frac{C_A}{4}\ln^2\frac{\mu^2}{Q^2r_g^2} + \frac{\beta_0}{4}\ln\frac{\mu^2}{Q^2r_g^2}\right)\right]$$

$$+ \frac{\alpha_s}{\pi}a_{20}^{\min}\frac{\alpha_s}{\pi}a_{10}^{\mathcal{C}_g}\left(\frac{16}{25}\frac{\xi}{r_g^2}\right).$$

Here $a_{10}^{\mathcal{C}_\kappa}\frac{\alpha_s(\mu)}{\pi}$ is the $\mathcal{O}(\alpha_s)$ result of the collinear function in eq. (3.20) after including ξ/r_g^2 factor that sets the $\delta(\xi/r_g^2)$ terms to zero. The new $\mathcal{O}(\alpha_s^2)$ pieces in the square brackets provide the boundary condition for NLL resummation, as we saw above in the max-R_g case. In the second line we have included parameterized the uncertainty from missing $\mathcal{O}(\alpha_s)$ pieces in terms of the parameter $a_{20}^{\min} \in [-2\pi,2\pi]$, while shifting the argument appropriately to take into account the different end-point of the jet mass spectrum at NLO [83] at $r_g = 8/5\sqrt{\xi}$ instead of $r_g = 2\sqrt{\xi}$ at LO. Additionally, we also include $\mathcal{O}(\alpha_s^2)$ cross terms from other pieces in eq. (4.31).

4.2.2 Intermediate-R_g regime

Finally, we describe the factorization in the intermediate R_g regime shown in the middle column in figure 4 which represents the most factorized scenario:

$$\mathcal{G}_\kappa^{\rm int}(z,\xi,r_g,\mu) = \sum_{\kappa'}\mathcal{H}_{\kappa'\to\kappa}(z,Q,\mu)S_G^\kappa(Q_{\rm cut},\zeta,\beta,\mu)\mathcal{S}_{\rm NGL}^\kappa\big(t[Q_{\rm cut},Q]\big)S_{c_g}^\kappa(Q_{\rm cut}r_g^{1+\beta},\beta,\mu)$$

$$\times \frac{\rm d}{{\rm d}\xi}\left[\mathcal{S}_{\rm NGL}^\kappa\Big(t\Big[Q_{\rm cut}r_g^{1+\beta},\frac{Q\xi}{r_g}\Big]\Big)\Sigma_{\rm int}^\kappa\Big(\frac{\xi}{r_g^2},Qr_g,\mu\Big)\right]. \tag{4.34}$$

Here the r_g-dependent NGLs are analogous to the previous case but involve running between the scales associated with CS_g and CS_m modes. Since they do depend on the jet mass, we have written them as a derivative of the cumulative jet mass cross section. Here $\Sigma_{\rm int}^\kappa$ is defined in terms of $\Sigma_{\rm no\,sd}^\kappa$ in eq. (4.11):

$$\Sigma_{\rm int}^\kappa\Big(\frac{\xi}{r_g^2},Qr_g,\mu\Big) = \Sigma_{\rm no\,sd}^\kappa\Big(\xi\to\frac{\xi}{r_g^2},Q\to Qr_g,\mu\Big). \tag{4.35}$$

The power corrections that are dropped in this regime are combinations of the previous cases:

$$\mathcal{G}_\kappa(z,\xi,r_g,\alpha_s(\mu)) = \mathcal{G}_\kappa^{\rm int}(z,\xi,r_g,\mu)\left[1+\mathcal{O}\Big(\xi_0,\Big(\frac{\xi}{\xi_0}\Big)^{\frac{2}{2+\beta}},r_g^{2+\beta}\frac{\xi_0}{\xi},\frac{\xi}{r_g^2}\Big)\right]. \tag{4.36}$$

Finally, we state the formula for the resummed cross section in this regime:

$$\tilde{\mathcal{G}}_\kappa^{\rm int}(\xi,r_g,Q,Q_{\rm cut},\zeta,\beta,\mu_{\rm int}) = N_\kappa^{\rm evol}\big(\mu_N,\mu_{gs},Q,Q_{\rm cut},\zeta,\beta\big)\mathcal{S}_{\rm NGL}^\kappa\big(t[Q_{\rm cut},Q]\big) \tag{4.37}$$

$$\times\left(\mathcal{S}_{\rm NGL}^\kappa\Big(t\Big[Q_{\rm cut}r_g^{1+\beta},\frac{Q\xi}{r_g}\Big]\Big)\mathcal{J}_\kappa^{\rm int}[\partial_\Omega;\xi,r_g,Q,Q_{\rm cut},\zeta,\beta,\mu_{\rm int}]\frac{e^{\gamma_E\Omega}}{\Gamma(-\Omega)}\right.$$

$$\left.+\frac{\rm d}{{\rm dln}\xi}\mathcal{S}_{\rm NGL}^\kappa\Big(t\Big[Q_{\rm cut}r_g^{1+\beta},\frac{Q\xi}{r_g}\Big]\Big)\times\mathcal{J}_\kappa^{\rm int}[\partial_\Omega;\xi,r_g,Q,Q_{\rm cut},\zeta,\beta,\mu_{\rm int}]\frac{e^{\gamma_E\Omega}}{\Gamma(1-\Omega)}\right)\Bigg|_{\Omega=\tilde{\omega}(\mu_s,\mu_J)}.$$

where

$$\mathcal{J}_\kappa^{\rm int}[\partial_\Omega;\xi,r_g,Q,Q_{\rm cut},\zeta,\beta,\mu_{\rm int}] \equiv \frac{e^{K_J+K_s+K_{cs_g}}}{\xi}\left(\frac{\mu_{cs_g}}{Q_{\rm cut}r_g^{1+\beta}}\right)^{\omega_{csg}}\frac{(Qr_g\mu_{cs_m})^{\omega_{csm}}(\mu_J^2)^{\omega_J}}{(\xi Q^2)^\Omega}$$

$$\times S_{c_g}^\kappa(Q_{\rm cut}r_g^{1+\beta},\beta,\mu_{cs_g})\tilde{J}_\kappa\left[\partial_\Omega+\log\Big(\frac{\mu_J^2}{Q^2\xi}\Big),\alpha_s(\mu_J)\right]\tilde{S}_{c_m}^\kappa\left[\partial_\Omega+\log\Big(\frac{\mu_{cs_m}r_g}{Q\xi}\Big),\alpha_s(\mu_{cs_m})\right], \tag{4.38}$$

and the intermediate-R_g profiles being

$$\mu_{\rm int}(\xi,r_g) \equiv \{\mu_N,\mu_{gs},\mu_J(\xi),\mu_{cs_m}(\xi,r_g),\mu_{cs_g}(r_g)\}. \tag{4.39}$$

Unlike the previous two cases, here every function contributes to the NLL boundary condition, and hence we do not need to include any additional $\mathcal{O}(\alpha_s^2)$ pieces.

5 Matched cross section

We now combine the cross sections in the three regimes and the two jet mass regions to obtain the complete matched cross section. In section 5.1 we describe how the results of ref. [55] are extended to match the max-R_g regime between soft drop and plain jet mass resummation regions. In section 5.2 we match this result to min- and int-R_g regimes, including the plain jet mass region. In section 5.3 we compute the perturbative uncertainty due to scale variation and nuisance parameters. The impact of $\mathcal{O}(\alpha_s^2)$ cross terms is assessed in section 5.4 and that of non-singular fixed order corrections in section 5.5. The computation of $C_{1\kappa}^{(n)}$ weights and the impact of NGLs is discussed in section 5.6.

5.1 Matching in the max-R_g regime

We first begin with combining the max-R_g cross sections in eqs. (4.6) and (4.24) to obtain a complete matched result in this regime. Our prescription for matching the two results parallels that of the single differential jet mass distribution derived in ref. [55], and is given by

$$\tilde{\mathcal{G}}_\kappa^{\max}(\xi, r_g) \equiv \tilde{\mathcal{G}}_\kappa^{\text{sd res.}}(\xi, r_g, \mu_{\text{sd}\to\text{plain}}) + [\tilde{\mathcal{G}}_\kappa^{\text{plain}}(\xi, r_g, \mu_{\text{plain}}) - \tilde{\mathcal{G}}_\kappa^{\text{sd res.}}(\xi, r_g, \mu_{\text{plain}})]. \quad (5.1)$$

For simplicity we have suppressed dependence on kinematic and grooming parameters. The profile $\mu_{\text{sd}\to\text{plain}}$ is designed such that it transitions from μ_{sd} scales in eq. (4.25) to μ_{plain} scales in eq. (4.7) by merging the c-soft μ_{cs} and global-soft μ_{gs} scales for $\xi \geq \xi_0$. As a result the two $\tilde{\mathcal{G}}_\kappa^{\text{sd res.}}$ terms cancel each other for $\xi \geq \xi_0$ leaving behind the correct $\tilde{\mathcal{G}}_\kappa^{\text{plain}}$ cross section in this region. In the soft drop resummation region for $\xi < \xi_0$, the term $\tilde{\mathcal{G}}_\kappa^{\text{sd res.}}(\xi, r_g, \mu_{\text{plain}})$ acts as subtraction piece for the $\tilde{\mathcal{G}}_\kappa^{\text{plain}}$ cross section evaluated with the same scale. By evaluating the collinear-soft and global-soft pieces at the same μ_s scale, the difference between the two amounts to $(\xi/\xi_0)^{\frac{2}{2+\beta}}$ soft drop related power corrections lacking in the $\tilde{\mathcal{G}}_\kappa^{\text{sd res.}}$ in eq. (4.23). Furthermore, since we have chosen to employ the same kernel $\mathcal{Q}_\kappa^{r_g}$ in eq. (4.18) in all the three pieces, the matching of r_g-related piece simply amounts to choosing the right soft scale in the argument of α_s and the resummation kernels $\omega_{cs_m,s}$ in eqs. (4.13) and (4.28). Finally, as remarked above, including the cross term $\mathcal{Q}_\kappa^{(\text{sd},r_g)}$ defined in eq. (4.19) in the plain jet mass cross section, eq. (5.1) seamlessly implements matching of $\mathcal{O}(\alpha_s^2)$ terms as well.

We show the result of matching for gluon and quark jets in figure 5. For now we will only include terms up to $\mathcal{O}(\alpha_s)$ and discuss the effects of including $\mathcal{O}(\alpha_s^2)$ cross terms below. Here we have taken the groomed jet radius cut r_g to lie somewhere between the maximum and minimum value of r_g for a given jet mass:

$$r_g^{\min}(\xi) \equiv \sqrt{\xi}, \qquad r_g^{\max}(\xi) \equiv \min\left\{1, \left[\left(\frac{\xi_0}{\xi}\right)^{\frac{2}{2+\beta}} - \zeta^2\right]^{-\frac{1}{2}}\right\}. \quad (5.2)$$

In figure 5 the vertical lines denote the extent of the soft drop operator expansion region, $\xi \in (\xi_{\text{SDOE}}, \xi_0')$. As explained above, the overlap curve $\mathcal{G}_\kappa^{\text{sd res.}}(\xi, r_g, \mu_{\text{plain}})$ merges with the un-factorized soft drop curve in for small jet masses and with the factorized one for $\xi > \xi_0$. We see that the effect of matching close to the cusp is particularly noticeable for gluon jets.
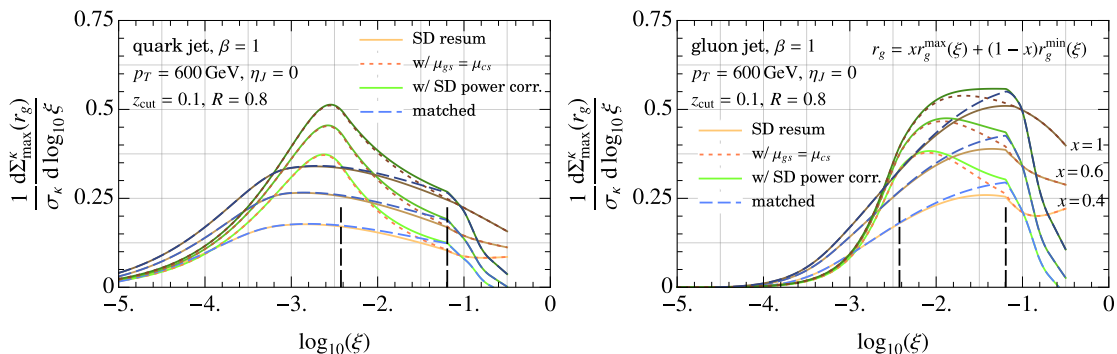
Figure 5. Matching for max-R_g cross section. The vertical lines denote the extent of the soft drop operator expansion region. The three curves correspond to choosing different intermediate values of groomed jet radius as a function of the jet mass.

5.2 Matched resummed cross section

Having defined the max-R_g cross section, we now follow the same strategy as in ref. [83] to obtain the matched resummed cross section valid across all three regimes:

$$\tilde{\mathcal{G}}_\kappa^{\text{match}}(\xi, r_g) \equiv \tilde{\mathcal{G}}_\kappa^{\text{int}}(\xi, r_g, \mu_{\text{hyb}}) + \left[\tilde{\mathcal{G}}_\kappa^{\text{max}}(\xi, r_g) - \tilde{\mathcal{G}}_\kappa^{\text{int}}(\xi, r_g, \mu_{\text{sd}\to\text{plain}}) \right] \tag{5.3}$$
$$+ \left[\tilde{\mathcal{G}}_\kappa^{\text{min}}(\xi, r_g, \mu_{\text{min}}) - \tilde{\mathcal{G}}_\kappa^{\text{int}}(\xi, r_g, \mu_{\text{min}}) \right].$$

The new hybrid profile μ_{hyb} that appears in the first term interpolates between the three sets of profiles $\mu_{\text{sd}\to\text{plain}}$, μ_{min} and μ_{int}, and is given by

$$\mu_{\text{hyb}} \equiv \left(\mu_{\text{min}} \right)^{w_{\text{min}}} \left(\mu_{\text{int}} \right)^{w_{\text{int}}} \left(\mu_{\text{sd}\to\text{plain}} \right)^{w_{\text{sd}\to\text{plain}}}, \quad w_{\text{min}} + w_{\text{int}} + w_{\text{sd}\to\text{plain}} = 1. \tag{5.4}$$

where w_i are weight functions that depend on both ξ and r_g and provide a prescription for demarcating boundaries between the three regimes, as shown in figure 3. The construction of the weight functions for soft drop resummation region was discussed in ref. [83]. In this work we extend the weight functions into the plain jet mass region, with their final result given by:

$$\begin{aligned} \text{2-EFT:} \quad & w_{\text{max}} = X\left(r_g, r_{g,t}(\xi) \right), \qquad w_{\text{int}} = 0, \\ \text{3-EFT:} \quad & w_{\text{max}} = X\left(r_g, r_{g,\text{PC}}^{\text{max}}(\xi) \right), \quad w_{\text{int}} = \left[1 - X\left(r_g, r_{g,\text{PC}}^{\text{max}}(\xi) \right) \right] X\left(r_g, r_{g,\text{PC}}^{\text{min}}(\xi) \right), \end{aligned} \tag{5.5}$$

and $w_{\text{min}} = 1 - w_{\text{int}} - w_{\text{max}}$. Here $X(r_g, r_{g,t}) \to 0$ for $r_g \ll r_{g,t}$ and $X(r_g, r_{g,t}) \to 1$ for $r_g \gg r_{g,t}$ transitioning around $r_{g,t}$. The transition points $r_{g,\text{PC}}^{\text{min}}(\xi)$ and $r_{g,\text{PC}}^{\text{min}}(\xi)$ are derived from power expansion parameters that determine validity of the EFT. We describe the details of the implementation in appendix C.

In figure 6 we show the matching across the three regimes for quark and gluon jets. We can see that the overlap pieces obtained from the intermediate-R_g regime (shown as dotted lines) cancel the max-R_g cross section for $r_g \ll r_g^{\text{max}}(\xi)$ and likewise the min-R_g cross section for $r_g \gg r_g^{\text{min}}$. The intermediate-R_g cross section with hybrid profiles (dashed) interpolates between the two overlap pieces. The matched curve thus obtained agrees with the NNLL
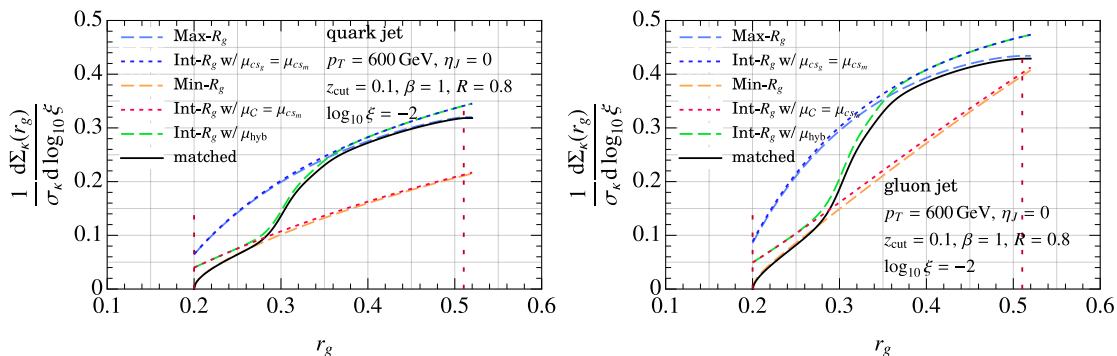
Figure 6. Matching across the three R_g regimes. The vertical lines denote the minimum and maximum r_g allowed for the specified $\xi = 10^{-2}$ value.

jet mass cross section at the end point $r_g = r_g^{\max}$, such that $\mathcal{G}_\kappa^{\mathrm{match}}(\xi, r_g^{\max}(\xi)) = \mathcal{G}_\kappa^{\mathrm{NNLL}}(\xi)$. However, note that $\mathcal{G}_\kappa^{\mathrm{match}}(\xi, r_g^{\max}(\xi)) \neq \mathcal{G}_\kappa^{\max}(\xi, r_g^{\max}(\xi))$. This is because the $\mathcal{G}_\kappa^{\max}$ cross section is derived from factorizing the jet mass measurement and lacks jet mass related power corrections which are supplied by the min-R_g cross section.

5.3 Perturbative uncertainty

In figure 7 we show the estimate of perturbative uncertainty at NNLL through scale variations and nuisance parameters. In appendix B we summarize the implementation of profile scales and their variation discussed in refs. [55, 83]. The variation involves six parameters that test sensitivity of the cross section to a) a uniform up/down variation of all scales, b) trumpet variation of ξ- and r_g-dependent scales in the resummation region, c) the scale where the coupling is deemed non-perturbative and frozen to a constant value, and d) breaking of three canonical relations which are used to derive the jet and (hard-)collinear scales from the soft scales.

In addition to scale variations, we also show uncertainty induced from lack of knowledge of two-loop non-logarithmic terms in the max-R_g and min-R_g cross sections via parameters $a_{20}^{\max/\min}$ in eqs. (4.18) and (4.33). As discussed in ref. [83] we limit these variations within their respective regime by multiplying them by the corresponding weight functions. We see that the $a_{20}^{\min}$ variation allows us to probe sensitivity to the order-dependent minimum r_g end point of the cross section, and that this variation also is the dominant uncertainty in the min-R_g regime. On the other hand, the variation due to $a_{20}^{\max}$ is subdominant compared to scale variations in the max-R_g region. We note that both these variations vanish for $r_g = r_g^{\max}$ and they do not impact the single differential jet mass cross section, whereas the scale variations are correlated between both single and doubly differential cross sections at each value of m_J.

5.4 Effect of two-loop pieces for NNLL resummation

Next, we inspect the effect of including $\mathcal{O}(\alpha_s^2)$ cross-terms to implement the boundary condition for NNLL resummation. As noted above, there are two places where this is needed: firstly in the max-R_g cross sections in eqs. (6.12) and (4.24) and secondly in the
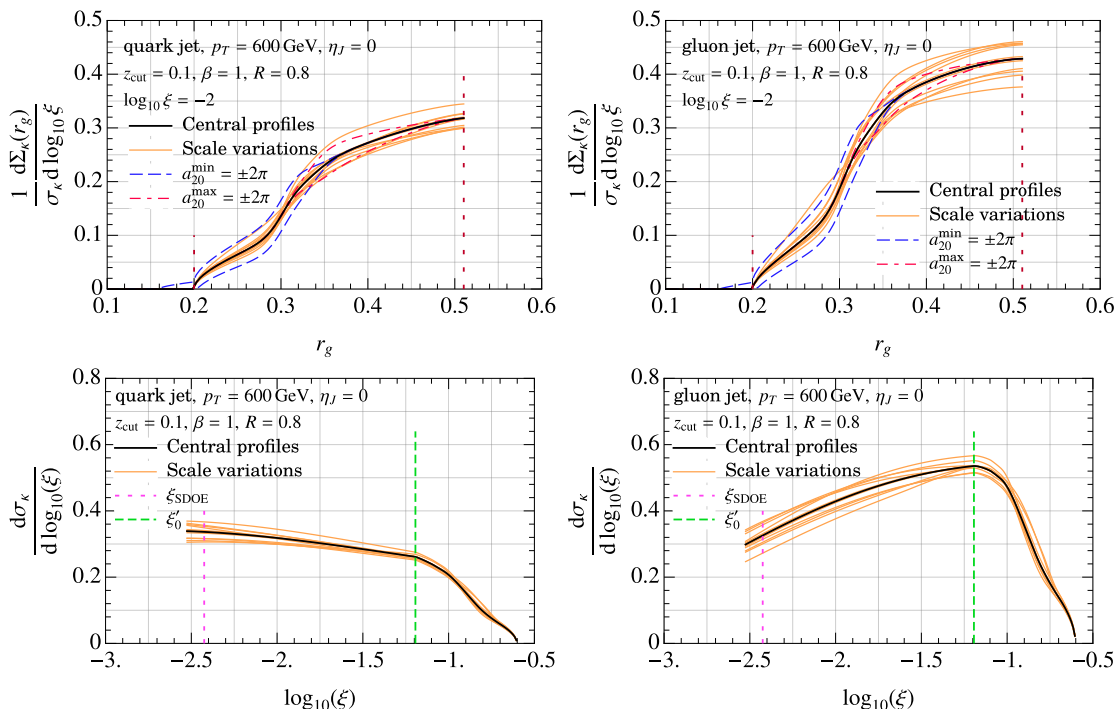
Figure 7. Profile and two-loop constant terms variation of the cumulative r_g cross section (top row) and the single differential jet mass cross section (bottom row) for quarks (left) and gluon (right) jets. The vertical lines in the top row denote the minimum and maximum r_g allowed for the specified $\xi = 10^{-2}$ value.

collinear function in the min-R_g regime as shown in eq. (4.33). Since these two loop pieces do not match straightforwardly as the one-loop pieces above in eq. (5.3) we include them in the cross section by multiplying these terms by the corresponding weight function. We show this in figure 8 where we plot

$$w_X(\xi, r_g)\, \xi \tilde{\mathcal{G}}_{\kappa X}^{[\mathcal{O}(\alpha_s^2)]}(\xi, r_g) \equiv w_X(\xi, r_g)\Big[\xi \tilde{\mathcal{G}}_{\kappa X}(\xi, r_g) - \xi \tilde{\mathcal{G}}_{\kappa X}^{[\mathcal{O}(\alpha_s)]}(\xi, r_g)\Big]\,, \tag{5.6}$$

where X refers to the regime considered and in the second term we truncate all the fixed-order terms to $\mathcal{O}(\alpha_s)$. In figure 8 we show the size of the two-loop pieces in the min-R_g cross section multiplied by $w_{\min}(\xi, r_g)$, and those from each of the three terms in eq. (5.1) with a common weight factor $w_{\max}(\xi, r_g)$. Note that despite the fact that corrections to the $\tilde{\mathcal{G}}_\kappa^{\mathrm{plain}}(\xi, r_g, \mu_{\mathrm{plain}})$ are relatively large, after including the two loop cross term in eq. (4.19) it cancels almost entirely against the correction from $\tilde{\mathcal{G}}_\kappa^{\mathrm{sd\,res.}}(\xi, r_g, \mu_{\mathrm{plain}})$ and only those remaining in the $\tilde{\mathcal{G}}_\kappa^{\mathrm{sd\,res.}}$ with soft drop resummation survive. These corrections are overall small and they turn out to be smaller than the perturbative uncertainty at NNLL from scale variations and nuisance parameters in figure 7. We will investigate them again when considering r_g-moments of the doubly differential cross section.
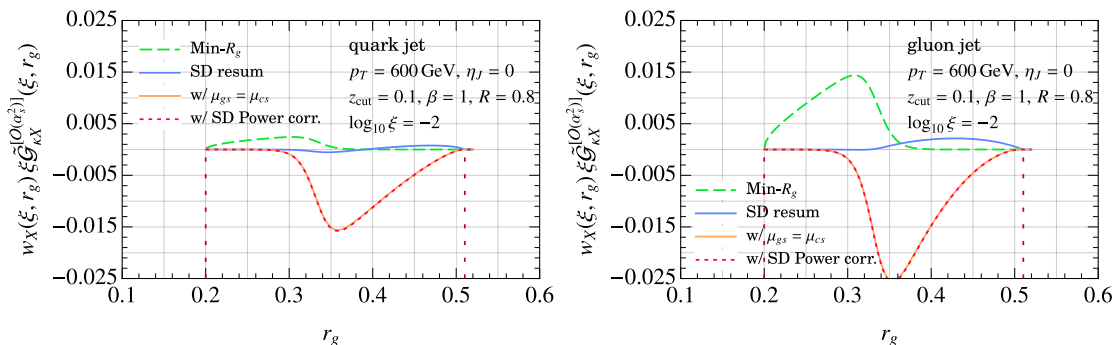
Figure 8. Size of two-loop pieces of the resummed cross section required for NLL′ boundary condition for quark and gluon jets. Here we have multiplied each piece in a given regime by corresponding weight function.

5.5 Non-singular corrections

Finally, we can include the non-singular pieces in the resummed, matched cross section as

$$\tilde{\mathcal{G}}_\kappa(\xi, r_g) \equiv \tilde{\mathcal{G}}_\kappa^{\text{match}}(\xi, r_g) + \Delta\tilde{\mathcal{G}}_\kappa^{[\text{n.s.}]}(\xi, r_g, \alpha_s(\mu_N)), \tag{5.7}$$

where

$$\Delta\tilde{\mathcal{G}}_\kappa^{[\text{n.s.}]}(\xi, r_g, \alpha_s(\mu_N)) \equiv \tilde{\mathcal{G}}_\kappa^{\text{FO}}(\xi, r_g, \alpha_s(\mu_N)) - \tilde{\mathcal{G}}_\kappa^{\text{match}}(\xi, r_g, \mu_i \to \mu_N) \tag{5.8}$$

In $\tilde{\mathcal{G}}_\kappa^{\text{match}}(\xi, r_g, \mu_i \to \mu_N)$ all the μ_i scales are set to the hard-collinear μ_N scale, turning off all resummation and non-global logarithms. To see how the cancellation of singular pieces between the fixed order and the matched cross section takes place, we note that the measurement function in eq. (3.52) can be written as

$$\xi\delta_\xi^{\text{FO}}(x, y, r_g, \xi_0, \zeta) \simeq \xi\Big[\delta_\xi^{\mathcal{C}}(x, y) + \delta_\xi^{\text{CS}_m}(x, y, 1) - \delta_\xi^{\text{CS}_m}(x, y, r_g) \tag{5.9}$$
$$+ \Delta\delta_{\xi, r_g}^{\text{CS, full}}(x, y, r_g, \xi_0, \zeta) + \Delta\delta_{\xi, \text{sd}}^{S_{\text{plain}}}(x, y, \xi_0, \zeta)\Big],$$

where the approximate equality results from dropping power suppressed terms in the soft approximations on the right hand side. The measurement functions on the right hand side were defined above in eqs. (3.18), (3.21), (3.41) and (3.47) respectively. It is not hard to see that setting all the scales in eq. (5.3) to μ_N will result in the above combination of factorization functions at one-loop.

In figure 9 we show the non-singular correction for quark and gluon jets. In fact, we find a complete cancellation between the fixed order and the matched cross-section for $r_g \leq r_g^{\text{max}}$ defined in eq. (5.2). This is because we have already taken into account the mass-power corrections in the collinear function in eq. (3.20) and the remaining power corrections in eq. (5.7) arise from only approximations made in the soft drop condition. For $r_g \leq r_g^{\text{max}}$ the r_g-constraint is stronger than soft drop constraint. This also serves as a strong cross check of the numerical implementation. On the other hand for $r_g > r_g^{\text{max}}$, the resummed-cross section saturates to single differential jet mass cross section governed by the soft drop
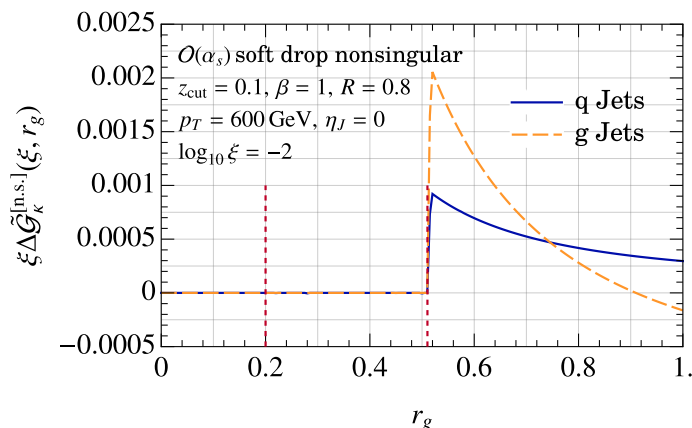
Figure 9. Non-singular correction related to approximations in the soft drop constraint. The vertical lines denote the range of groomed jet radius allowed for the specified jet mass value of $\xi = 10^{-2}$. The non-singular correction related to soft drop is non-zero only beyond this range since it is where the soft drop constraint is a stronger condition than r_g-constraint.

constraint. It is here there is a non-trivial non-singular correction in eq. (5.7). However, as can be seen in figure 9, this correction is numerically negligible. It is of the same order as the non-singular correction in single differential jet mass which was also shown to be numerically negligible in ref. [55]. Hence, we will ignore the non-singular corrections from soft drop constraints entirely in our numerical analysis.

5.6 R_g-weighted jet mass cross section

Having set up the matched cross section we can compute the r_g-weighted cross section differential in jet mass that are relevant phenomenologically as perturbative weights of hadronization and underlying event corrections. To facilitate comparison with Monte Carlo event generators we will normalize the weighted cross section with the usual jet mass cross section. To this end we define

$$C_{1\kappa}^{(n)}(\xi) \frac{1}{\hat{\sigma}_\kappa} \frac{\mathrm{d}\hat{\sigma}_\kappa}{\mathrm{d}\xi} \equiv \int_0^1 \mathrm{d}r_g \, r_g^n \frac{1}{\hat{\sigma}_\kappa} \frac{\mathrm{d}^2\hat{\sigma}_\kappa}{\mathrm{d}r_g \mathrm{d}\xi} \tag{5.10}$$

Since we have access to the cross section cumulative in r_g, we have

$$\frac{1}{\hat{\sigma}_\kappa} \frac{\mathrm{d}^2\hat{\sigma}_\kappa}{\mathrm{d}r_g \mathrm{d}\xi} = \frac{\mathrm{d}\tilde{\mathcal{G}}_\kappa^{\mathrm{match}}(\xi, r_g)}{\mathrm{d}r_g}, \qquad \frac{1}{\hat{\sigma}_\kappa} \frac{\mathrm{d}\hat{\sigma}_\kappa}{\mathrm{d}\xi} = \tilde{\mathcal{G}}_\kappa^{\mathrm{match}}(\xi, 1) \equiv \tilde{\mathcal{G}}_\kappa^{\mathrm{match}}(\xi). \tag{5.11}$$

Hence, the moment $C_1^{(n)}(\xi)$ becomes

$$\begin{aligned}
C_{1\kappa}^{(n)}(\xi) &= \frac{1}{\tilde{\mathcal{G}}_\kappa^{\mathrm{match}}(\xi)} \int_{r_g^{\min}(\xi)}^{r_g^{\max}(\xi)} \mathrm{d}r_g \, r_g^n \frac{\mathrm{d}}{\mathrm{d}r_g} \tilde{\mathcal{G}}_\kappa^{\mathrm{match}}(\xi, r_g) \\
&= \frac{1}{\tilde{\mathcal{G}}_\kappa^{\mathrm{match}}(\xi)} \left([r_g^{\max}(\xi)]^n \tilde{\mathcal{G}}_\kappa^{\mathrm{match}}(\xi, r_g^{\max}(\xi)) - n \int_{r_g^{\min}(\xi)}^{r_g^{\max}(\xi)} \mathrm{d}r_g \, r_g^{n-1} \tilde{\mathcal{G}}_\kappa^{\mathrm{match}}(\xi, r_g) \right) \\
&= [r_g^{\max}(\xi)]^n - \frac{n}{\tilde{\mathcal{G}}_\kappa^{\mathrm{match}}(\xi)} \int_{r_g^{\min}(\xi)}^{r_g^{\max}(\xi)} \mathrm{d}r_g \, r_g^{n-1} \tilde{\mathcal{G}}_\kappa^{\mathrm{match}}(\xi, r_g),
\end{aligned} \tag{5.12}$$
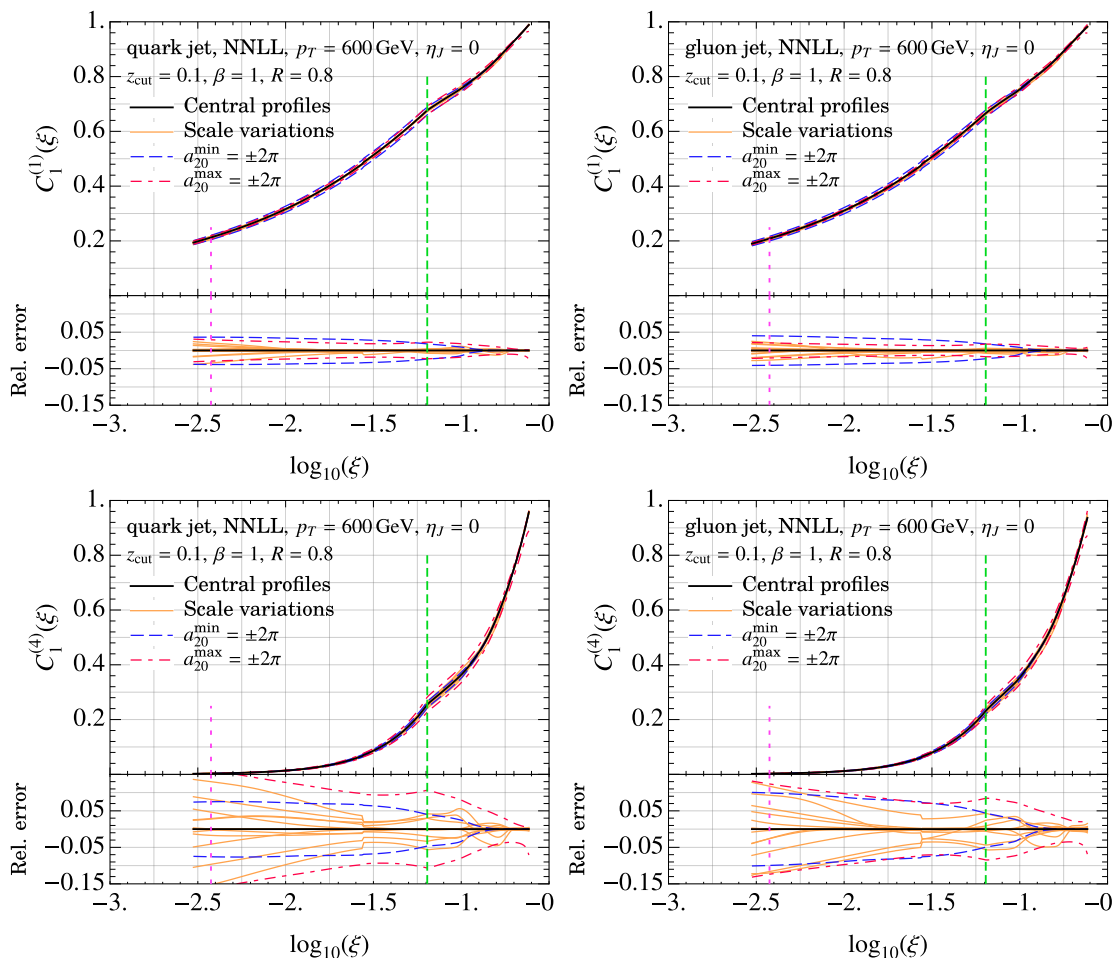
Figure 10. $C_{1\kappa}^{(n)}$ for $n = 1$ (top) and $n = 4$ (bottom) for quark and gluon jets. The vertical lines denote the extent of the SDOE region.

where we have used the fact that the differential cross section only has support between $r_g^{\min}(\xi)$ and $r_g^{\max}(\xi)$.

In figure 10 we show $C_{1\kappa}^{(n)}$ for $n = 1, 4$ cases, relevant for hadronization and underlying event corrections. Following the same color scheme as in figure 7 we find that the effect of scale variations on the normalized moment is very small. This is because the scale variation uncertainties are correlated between the doubly differential and the singly differential cross sections and cancel in the ratio. On the other hand, the dominant uncertainty in $C_{1\kappa}^{(n)}$ results from variation of the $a_{20}^{\min}$ and $a_{20}^{\max}$ nuisance parameters.

In figure 11 we inspect the effect of adding two-loop logarithmic pieces, that are required to implement consistently the NNLL boundary condition, and non-global logs at NLL (both separately) by considering the fractional deviation in the moment. We also show for comparison the fractional deviation from adding two loop non-logarithmic terms in the min-R_g cross section by varying the nuisance parameter $a_{20}^{\min}$, which dominates both these effects. The $a_{20}^{\max}$ variation (not shown) in the ungroomed region will similarly dominate
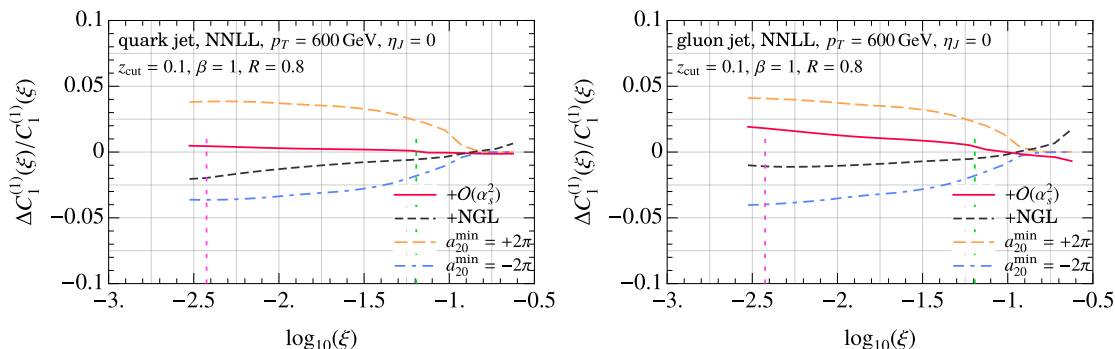
Figure 11. Fractional deviation of $C_1^{(1)}(\xi)$ upon including $\mathcal{O}(\alpha_s^2)$ pieces and non-global logarithms compared with that from varying the $a_{20}^{\min}$ nuisance parameter.

the effect of two-loop logarithmic terms. Hence, in our final numerical analysis we can safely ignore the $\mathcal{O}(\alpha_s^2)$ logarithmic pieces and non-global logarithms.

6 Soft drop boundary cross section

We now consider the computation of the soft drop boundary cross section stated in eq. (1.7). After describing the measurement function in section 6.1, we discuss the computation in the plain jet mass and soft drop resummation regions in sections 6.2 and 6.3. As we will see below, the one-loop fixed order results for soft functions are transformed into resummation kernels whose computation is discussed in section 6.4. In section 6.5 we discuss the fixed order non-singular corrections and show them to be small as seen above. In section 6.6 we finally describe the computation of the $C_{2\kappa}^{(n)}$ moment.

6.1 The measurement function

We are specifically interested in the projection of the triply differential cross section on the boundary of the soft drop:

$$\frac{1}{\hat{\sigma}_\kappa} \frac{\mathrm{d}\hat{\sigma}_\kappa^{\circledcirc}}{\mathrm{d}r_g \mathrm{d}\xi} \equiv \int \mathrm{d}z_g\, \delta(z_g - \xi_0 r_g^\beta) \frac{1}{\hat{\sigma}_\kappa} \frac{\mathrm{d}\hat{\sigma}_\kappa}{\mathrm{d}z_g \mathrm{d}r_g \mathrm{d}\xi} \tag{6.1}$$

However, instead of directly computing the triply-differential cross section we can equivalently calculate the doubly differential cross section while including a soft drop condition small shift in the soft drop condition:

$$\hat{\Theta}_{\mathrm{sd}}(x, y, \xi_0, \zeta, \varepsilon) = \Theta\left(\frac{\min\{x_1, x_2\}}{x_1 + x_2} - \xi_0\left(\frac{y}{4x_1 x_2}\right)^{\frac{\beta}{2}} + \varepsilon\right)$$

$$= \hat{\Theta}_{\mathrm{sd}}(x, y, \xi_0, \zeta) + \varepsilon\, \delta\left(\frac{\min\{x_1, x_2\}}{x_1 + x_2} - \xi_0\left(\frac{y}{4x_1 x_2}\right)^{\frac{\beta}{2}}\right) + \dots, \tag{6.2}$$

and differentiate it with respect to ε:

$$\frac{1}{\hat{\sigma}_\kappa} \frac{\mathrm{d}\hat{\sigma}_\kappa^{\circledcirc}}{\mathrm{d}r_g \mathrm{d}\xi} = \frac{\mathrm{d}}{\mathrm{d}\varepsilon}\left(\frac{1}{\hat{\sigma}_\kappa} \frac{\mathrm{d}^2 \hat{\sigma}_{\kappa,\varepsilon}}{\mathrm{d}r_g \mathrm{d}\xi}\right)\bigg|_{\varepsilon \to 0}, \tag{6.3}$$

where $\mathrm{d}\sigma_{\kappa,\varepsilon}$ is calculated with the shifted soft drop condition.

Additionally, as explained in ref. [83], we only need to consider the max-R_g regime which captures the correct two-pronged geometry, whereas the contributions from the intermediate and min-R_g enter beyond the LL nonperturbative factorization in eq. (1.3). In the discussion above for doubly differential cross section we did not drop contributions from these regions because effects of hadronization (and of ISR and underlying event) involve positive powers of r_g-moments, and hence they are naturally suppressed. Whereas for the boundary cross section we require $1/r_g$ moment, which receives large power corrections from the intermediate and min-R_g region, which must be suppressed by hand when calculating using shifted soft drop condition.

As above, in practice, we will find it easier to compute first the soft matrix elements, and use them in the factorization formulae as well as subtractions for fixed order pieces. In the soft limit, the shifted soft drop condition reads

$$\hat{\Theta}_{\mathrm{sd}}^{(s)}(x,y,\xi_0,\zeta,\varepsilon) = \Theta\left(y\zeta^2 + x - \xi_0^{\frac{2}{2+\beta}}y^{\frac{\beta}{2+\beta}} + \frac{2\varepsilon}{2+\beta}\left(\frac{y}{\xi_0}\right)^{\frac{\beta}{2+\beta}}\left(\zeta^2 + \frac{x}{y}\right)^{\frac{\beta}{2}} + \dots\right)$$

$$= \hat{\Theta}_{\mathrm{sd}}^{(s)}(x,y,\xi_0,\zeta) + \frac{2\varepsilon}{2+\beta}\,\delta\left(y\zeta^2 + x - (\xi_0)^{\frac{2}{2+\beta}}(y)^{\frac{\beta}{2+\beta}}\right) + \dots. \quad (6.4)$$

The same in collinear-soft limit is given by

$$\hat{\Theta}_{\mathrm{sd}}^{(cs)}(x,y,\xi_0,\varepsilon) = \Theta\left(x - \xi_0^{\frac{2}{2+\beta}}y^{\frac{\beta}{2+\beta}} + \frac{2\varepsilon}{2+\beta}\left(\frac{y}{\xi_0}\right)^{\frac{\beta}{2+\beta}}\left(\frac{x}{y}\right)^{\frac{\beta}{2}} + \dots\right)$$

$$= \hat{\Theta}_{\mathrm{sd}}^{(cs)}(x,y,\xi_0) + \frac{2\varepsilon}{2+\beta}\,\delta\left(x - \xi_0^{\frac{2}{2+\beta}}y^{\frac{\beta}{2+\beta}}\right) + \dots. \quad (6.5)$$

Thus, we define:

$$\hat{\delta}_{\mathrm{sd}}^{(s)}(x,y,\xi_0,\zeta) \equiv \frac{2}{2+\beta}\,\delta\left(y\zeta^2 + x - (\xi_0)^{\frac{2}{2+\beta}}(y)^{\frac{\beta}{2+\beta}}\right), \quad (6.6)$$

$$\hat{\delta}_{\mathrm{sd}}^{(cs)}(x,y,\xi_0) \equiv \frac{2}{2+\beta}\,\delta\left(x - \xi_0^{\frac{2}{2+\beta}}y^{\frac{\beta}{2+\beta}}\right).$$

6.2 Plain jet mass region

We first consider the plain jet mass region. Here the modification to the soft drop condition only affects the S_{plain} mode. Thus, the measurement function analogous to eq. (3.45) is given by

$$\delta_{\xi,\varepsilon}^{S_{\mathrm{plain}}}(x,y,r_g,\xi_0,\zeta) \equiv \hat{\Theta}_{k_T}^{(s)}(x,y)\hat{\delta}_{\mathrm{sd}}^{(s)}(x,y,\xi_0,\zeta)\left[\hat{\Theta}_{r_g}^{(s)}(x,y,r_g)\delta(\xi-y) - \delta(x)\right], \quad (6.7)$$

where here, and everywhere below, we will include a subscript ε to distinguish functions relevant to the soft drop boundary cross section. Similar to eq. (3.46) we can isolate the piece corresponding to r_g measurement:

$$\delta_{\xi,\varepsilon}^{S_{\mathrm{plain}}}(x,y,r_g,\xi_0,\zeta) = \Delta\delta_{\xi,r_g,\varepsilon}^{\mathrm{CS,\,full}}(x,y,r_g,\xi_0,\zeta) + \Delta\delta_{\xi,\mathrm{sd},\varepsilon}^{S_{\mathrm{plain}}}(x,y,\xi_0,\zeta). \quad (6.8)$$

Unlike eq. (3.46), there is no term corresponding to ungroomed measurement as we have differentiated with respect to ε. These terms are given by

$$\Delta \delta_{\xi, r_g, \varepsilon}^{\mathrm{CS, full}}(x, y, r_g, \xi_0, \zeta) \equiv -\hat{\Theta}_{k_T}^{(s)}(x, y)\big(1 - \hat{\Theta}_{r_g}^{(s)}(x, y, r_g)\big)\hat{\delta}_{\mathrm{sd}}^{(s)}(x, y, \xi_0, \zeta)\delta(\xi - y), \quad (6.9)$$

$$\Delta \delta_{\xi, \mathrm{sd}, \varepsilon}^{S_{\mathrm{plain}}}(x, y, \xi_0, \zeta) \equiv +\hat{\Theta}_{k_T}^{(s)}(x, y)\hat{\delta}_{\mathrm{sd}}^{(s)}(x, y, \xi_0, \zeta)\big[\delta(\xi - y) - \delta(\xi)\big].$$

The fixed order correction that captures the dependence on the r_g measurement is given by

$$Q_{\mathrm{cut}}^{\frac{1}{1+\beta}} \Delta S_{r_g, \varepsilon}^{\kappa}\Big(\ell^+ Q_{\mathrm{cut}}^{\frac{1}{1+\beta}}, r_g, Q_{\mathrm{cut}}, \zeta, \beta, \alpha_s(\mu)\Big) = \frac{1}{Q}\mathcal{S}_{\kappa}^{[1]}\Big(\xi = \frac{\ell^+}{Q}, \Delta\delta_{\xi, r_g, \varepsilon}^{\mathrm{CS, full}}, \mu\Big) \quad (6.10)$$

$$= \frac{\alpha_s C_\kappa}{\pi} \frac{\Theta(\ell^+ - Q_{\mathrm{cut}}'v(r_g))\Theta(Q_{\mathrm{cut}}' - \ell^+)}{(\ell^+)^2/Q}\Big(\Big(\frac{Q_{\mathrm{cut}}}{\ell^+}\Big)^{\frac{2}{2+\beta}} - \zeta^2\Big)^{-1},$$

and analogously, the soft drop related fixed-order piece is given by

$$\Delta S_{\mathrm{sd}, \varepsilon}^{\kappa}(\ell^+, Q_{\mathrm{cut}}, \zeta, \beta, \alpha_s(\mu)) = \frac{1}{Q}\mathcal{S}_{\kappa}^{[1]}\Big(\xi = \frac{\ell^+}{Q}, \Delta\delta_{\xi, \mathrm{sd}, \varepsilon}^{S_{\mathrm{plain}}}, \mu\Big) \quad (6.11)$$

$$= \frac{2}{2 + \beta}\frac{\alpha_s(\mu)C_\kappa}{\pi}\Bigg[\frac{\Theta(\ell^+)\Theta(Q_{\mathrm{cut}}' - \ell^+)}{(\ell^+)^2/Q}\Big(\Big(\frac{Q_{\mathrm{cut}}}{\ell^+}\Big)^{\frac{2}{2+\beta}} - \zeta^2\Big)^{-1}\Bigg]_+^{[Q_{\mathrm{cut}}']}.$$

These fixed order corrections are combined with the rest of the factorized cross section in precisely the same manner as in eq. (4.16) above

$$\tilde{\mathcal{G}}_{\kappa, \varepsilon}^{\mathrm{plain}}(\xi, Q, Q_{\mathrm{cut}}, \zeta, \mu_{\mathrm{plain}}) = N_{\mathrm{incl}}^{\kappa}(Q, \mu_N)e^{K_N}\Big(\frac{\mu_N}{Q}\Big)^{\omega_N} \quad (6.12)$$

$$\times \Bigg(\mathcal{S}_{\mathrm{NGL}}^{\kappa}(t[Q\xi, Q])\mathcal{J}_{\kappa}^{\mathrm{plain}}[\partial_\Omega; \xi, Q, \mu_{\mathrm{plain}}]\mathcal{Q}_{\kappa, \varepsilon}^{\mathrm{plain}}(\Omega, \alpha_s(\mu_s))$$

$$+ \Big(\frac{\mathrm{d}}{\mathrm{dln}\xi}\mathcal{S}_{\mathrm{NGL}}^{\kappa}(t[Q\xi, Q])\Big)\mathcal{J}_{\kappa}^{\mathrm{plain}}[\partial_\Omega; \xi, Q, \mu_{\mathrm{plain}}]\mathcal{Q}_{\kappa, \varepsilon}^{\mathrm{plain}}(\Omega - 1, \alpha_s(\mu_s))\Bigg)\Bigg|_{\Omega = \tilde{\omega}(\mu_s, \mu_J)}.$$

Similar to eq. (4.17), the kernels $\mathcal{Q}_{\kappa, \varepsilon}^{\mathrm{plain}}$ include Laplace transforms of the soft functions in eqs. (6.10) and (6.11), but also $\mathcal{O}(\alpha_s^2)$ cross terms that are required to consistently carry out NNLL resummation [83]. In table 2 we summarize the various $\mathcal{O}(\alpha_s^2)$ cross terms that constitute the kernel $\mathcal{Q}_{\kappa, \varepsilon}^{\mathrm{plain}}$. We have included cross terms involving $\Delta S_{\mathrm{sd}}^{\kappa}$ pieces for consistent matching with the cross section in the soft drop resummation regime. Finally, there are also cross terms arising from $\mathcal{O}(\alpha_s)$ parts of $\mathcal{J}_{\kappa}^{\mathrm{plain}}$ and $\mathcal{O}(\alpha_s)$ soft functions that we have not shown.

6.3 Soft drop resummation region

We now turn to the boundary cross section in the soft drop resummation region. Here, including shift in the boundary cross section modifies the measurement for the global soft and collinear-soft functions:

$$\hat{\Theta}_{\varepsilon}^{S_G}(x, y, \xi_0, \zeta) \equiv -\hat{\Theta}_{k_T}^{(s)}(x, y)\hat{\delta}_{\mathrm{sd}}^{(s)}(x, y, \xi_0, \zeta) + \hat{\delta}_{\mathrm{sd}}^{(s)}(x, y, \xi_0, \zeta), \quad (6.13)$$

$$\delta_{\xi, \varepsilon}^{\mathrm{CS}}(x, y, r_g, \xi_0) \equiv \hat{\delta}_{\mathrm{sd}}^{(cs)}(x, y, \xi_0)\big[\delta(\xi - y) - \delta(\xi)\big] + \Delta\delta_{\xi, r_g, \varepsilon}^{\mathrm{CS}}(x, y, r_g, \xi_0),$$

	$\mathcal{O}(\alpha_s)$	$\mathcal{O}(\alpha_s^2)$
Ungroomed region	$\partial_{r_g}\Delta S_{r_g,\varepsilon}^{\kappa[1]}$	$\Delta S_{\text{sd}}^{\kappa[1]}\partial_{r_g}\Delta S_{r_g,\varepsilon}^{\kappa[1]}, \quad \Delta S_{\text{sd},\varepsilon}^{\kappa[1]}\partial_{r_g}\Delta S_{r_g}^{\kappa[1]}, \quad \partial_{r_g}\big[\Delta S_{r_g}^{\kappa[1]}\Delta S_{r_g,\varepsilon}^{\kappa[1]}\big]$
SD res., $\beta=0$	$\partial_{r_g}\Delta S_{r_g,\varepsilon}^{\kappa[1]}$	$\mathcal{J}_{\kappa,\varepsilon}^{\text{sd res}}[\partial_\Omega]\,\partial_{r_g}\Delta S_{r_g}^{\kappa[1]}, \quad \partial_{r_g}\big[\Delta S_{r_g}^{\kappa[1]}\Delta S_{r_g,\varepsilon}^{\kappa[1]}\big]$
SD res., $\beta>0$	$\partial_{r_g}\Delta S_{r_g,\varepsilon}^{\kappa[1]}$	$\Delta S_{\text{sd},\varepsilon}^{\kappa[1]}\partial_{r_g}\Delta S_{r_g}^{\kappa[1]}, \quad \partial_{r_g}\big[\Delta S_{r_g}^{\kappa[1]}\Delta S_{r_g,\varepsilon}^{\kappa[1]}\big]$

Table 2. Fixed order corrections to soft functions that appear in soft drop boundary resummation kernels $\mathcal{Q}_{\kappa,\varepsilon}^{\text{plain}}$ and $\mathcal{Q}_{\kappa,\varepsilon}^{\text{sd res.}}$ for plain and soft drop resummation regions respectively. We have not shown the additional $\mathcal{O}(\alpha_s^2)$ terms that result from action of $\mathcal{J}_\kappa^{\text{plain}}[\partial_\Omega]$ and $\mathcal{J}_\kappa^{\text{sd res.}}[\partial_\Omega]$ on $\mathcal{O}(\alpha_s)$ pieces.

The corresponding soft functions are given by

$$S_{G,\varepsilon}^\kappa(Q_{\text{cut}},\zeta,\beta,\mu) \equiv \mathcal{S}_\kappa^{[1]}\big(\,\cdot\,,\hat{\Theta}_\varepsilon^{S_G},\mu\big) + \mathcal{O}(\alpha_s^2)\,, \tag{6.14}$$

$$S_{c,\varepsilon}^\kappa(\tilde{k},r_g,Q_{\text{cut}},\beta,\mu) \equiv \frac{1}{QQ_{\text{cut}}^{\frac{1}{1+\beta}}}\mathcal{S}_\kappa^{[1]}\bigg(\xi = \frac{\tilde{k}}{QQ_{\text{cut}}^{\frac{1}{1+\beta}}},\delta_{\xi,\varepsilon}^{\text{CS}},\mu\bigg) + \mathcal{O}(\alpha_s^2)\,.$$

Here, the second term in eq. (6.13) in the global soft measurement function $\hat{\Theta}_\varepsilon^{S_G}$ is required to appropriately cancel the UV divergences in of the virtual piece. In the collinear-soft measurement function, the measurement $\Delta\delta_{\xi,r_g,\varepsilon}^{\text{CS}}$ is simply the collinear limit of the one in eq. (6.9), which yields

$$S_{c,\varepsilon}^\kappa(\tilde{k},r_g,Q_{\text{cut}},\beta,\mu) = S_{c,\varepsilon}^\kappa(\tilde{k},\beta,\mu) + \Delta S_{r_g,\varepsilon}^\kappa(\tilde{k},r_g,Q_{\text{cut}},\beta,\alpha_s(\mu))\,. \tag{6.15}$$

However, as we did above for the usual soft drop case, we will continue to include the power suppressed terms and employ the full measurement in eq. (6.9).

It is helpful to consider the $\beta=0$ and $\beta>0$ cases separately. For $\beta=0$, the soft functions are given by

$$S_{G,\varepsilon}^{\kappa,\text{bare}}(Q_{\text{cut}},\zeta,\beta=0,\mu) = \frac{1}{\xi_0}\frac{\alpha_s C_\kappa}{\pi}\bigg(\frac{1}{\epsilon} + 2\ln\Big(\frac{\mu}{Q_{\text{cut}}}\Big)\bigg)\,, \tag{6.16}$$

$$S_{c,\varepsilon}^{\kappa,\text{bare}}(\tilde{k},\beta=0,\mu) = \frac{\alpha_s C_\kappa}{\pi}\frac{1}{\xi_0}\bigg[-\frac{\delta(\tilde{k})}{\varepsilon} + \mathcal{L}_0(\tilde{k},\mu^2)\bigg]\,,$$

and the same r_g-dependent correction as in eq. (6.11). Here we find an extra log-divergence [83] which is unrelated to the soft drop factorization we considered above. The extra divergence leads to a nontrivial non-cusp anomalous dimension $\varepsilon\,\gamma_0^\varepsilon(z_{\text{cut}})$ where

$$\gamma_0^{\varepsilon,S_G^\kappa} = -\gamma_0^{\varepsilon,S_c^\kappa} \equiv \gamma_0^\varepsilon(z_{\text{cut}}) = \frac{8C_\kappa}{z_{\text{cut}}}\,, \qquad (\beta=0)\,. \tag{6.17}$$

We can verify that for $\mu_{cs}=\mu_{gs}=\mu$ the fixed order pieces add to yield the correct fixed order result in eq. (6.11) in the limit $\xi \ll \xi_0$ by noting that

$$\begin{aligned}
Q_{\text{cut}}^{\frac{1}{1+\beta}} S_{c,\varepsilon}^\kappa(Q_{\text{cut}}^{\frac{1}{1+\beta}}\ell^+,\beta=0,\mu) &= \frac{1}{\xi_0}\frac{\alpha_s C_\kappa}{\pi}Q_{\text{cut}}\mathcal{L}_0(Q_{\text{cut}}\ell^+,\mu^2) \\
&= \frac{1}{\xi_0}\frac{\alpha_s C_\kappa}{\pi}\bigg[\mathcal{L}_0(\ell^+,\mu) - \ln\Big(\frac{\mu}{Q_{\text{cut}}}\Big)\delta(\ell^+)\bigg]
\end{aligned} \tag{6.18}$$

adding to this the contribution from global soft function, we find

$$\delta(\ell^+)S_{G,\varepsilon}^{\kappa}(Q_{\text{cut}},\zeta,\beta=0,\mu) + Q_{\text{cut}}^{\frac{1}{1+\beta}}S_{c,\varepsilon}^{\kappa}\left(Q_{\text{cut}}^{\frac{1}{1+\beta}}\ell^+,\beta=0,\mu\right) \tag{6.19}$$

$$= \frac{1}{\xi_0}\frac{\alpha_s C_\kappa}{\pi}\left[\mathcal{L}_0(\ell^+,\mu) + \ln\left(\frac{\mu}{Q_{\text{cut}}}\right)\delta(\ell^+)\right]$$

$$= \frac{1}{\xi_0}\frac{\alpha_s C_\kappa}{\pi}\left[\frac{\Theta(\ell^+)}{\ell^+}\right]_+^{[Q_{\text{cut}}]},$$

which is precisely the limit $\ell^+/Q_{\text{cut}} \ll \zeta$ of $\Delta S_{\text{sd},\varepsilon}^{\kappa}$ above for $\beta = 0$.

On the other hand, for $\beta > 0$, there is no straightforward way to split $\Delta S_{\text{sd},\varepsilon}^{\kappa}$ in eq. (6.11) into two pieces as the divergence is a power law and we simply include the piece as in the case of plain jet mass region. Thus, the resummed formula in soft drop resummation region is given by

$$\tilde{\mathcal{G}}_{\kappa,\varepsilon}^{\text{sd res}}(\xi,r_g,Q,Q_{\text{cut}},\zeta,\beta,\mu_{\text{sd}}) = N_\kappa^{\text{evol}}(\mu_N,\mu_{gs},Q,Q_{\text{cut}},\zeta,\beta)\mathcal{S}_{\text{NGL}}^{\kappa}(t[Q_{\text{cut}},Q]) \tag{6.20}$$

$$\times \mathcal{J}_{\kappa,\varepsilon}^{\text{sd res.}}[\partial_\Omega;\xi,Q,Q_{\text{cut}},\mu_{\text{sd}}]\,\mathcal{Q}_{\kappa,\varepsilon}^{\text{sd res.}}(\Omega,\xi,r_g,Q_{\text{cut}},\zeta,\beta,\alpha_s(\mu_{cs}))\Big|_{\Omega=\tilde{\omega}(\mu_{cs},\mu_J)}.$$

$$\mathcal{J}_{\kappa,\varepsilon}^{\text{sd res.}}[\partial_\Omega] = \left(1 + \delta_{\beta,0}\eta(\gamma_0^{\varepsilon}(z_{\text{cut}}),\mu_{cs},\mu_{gs})\right)\mathcal{J}_{\kappa}^{\text{sd res}}[\partial_\Omega] \tag{6.21}$$

$$+ \frac{\delta_{\beta,0}}{\xi\xi_0}\,e^{K_{cs}+K_J}\frac{\left(\mu_J^2\right)^{\omega_J}\left(Q\mu_{cs}\right)^{\omega_{cs}}}{(\xi Q^2)^{\Omega}}\left(\frac{\mu_{cs}}{Q_{\text{cut}}}\right)^{\frac{\omega_{cs}}{1+\beta}}$$

$$\times \left[\frac{2\alpha_s(\mu_{gs})C_\kappa}{\pi}\ln\left(\frac{\mu_{gs}}{Q_{\text{cut}}}\right) - \frac{\alpha_s(\mu_{cs})C_\kappa}{\pi}\left(\partial_\Omega + \log\left(\frac{\mu_{cs}}{Q\xi}\left(\frac{\mu_{cs}}{Q_{\text{cut}}}\right)^{\frac{1}{1+\beta}}\right)\right)\right],$$

Here $\mathcal{J}_{\kappa}^{\text{sd res}}[\partial_\Omega]$ is the same function that appeared above for the usual soft drop cross section in eq. (4.27). The additional $\mathcal{O}(\varepsilon)$ terms arise only for $\beta = 0$ case. The first of these involves $\eta(\gamma_0^{\varepsilon}(z_{\text{cut}}),\mu_{cs},\mu_{gs})$ which is the single log non-cusp resummation kernel arising from the new non-cusp anomlous dimension in eq. (6.17):

$$\eta(\gamma_0^{\varepsilon}(z_{\text{cut}}),\mu_{cs},\mu_{gs}) = -\frac{\gamma_0^{\varepsilon}(z_{\text{cut}})}{2\beta_0}\ln\left(\frac{\alpha_s(\mu_{cs})}{\alpha_s(\mu_{gs})}\right). \tag{6.22}$$

In the third line of eq. (6.21) we have included the $\mathcal{O}(\alpha_s)$ logarithms associated with the factorized $\beta = 0$ boundary global-soft and collinear-soft functions in eq. (6.16). For this reason these pieces are not included in the $\mathcal{Q}_{\kappa,\varepsilon}^{\text{sd res.}}$ kernel for $\beta = 0$. For $\beta > 0$, the non-factorized $\Delta S_{\text{sd},\varepsilon}^{\kappa}$ contribution is included directly in $\mathcal{Q}_{\kappa,\varepsilon}^{\text{sd res.}}$ as indicated in table 2.

6.4 Computing the resummation kernels

We now turn to the computation of the resummation kernels that appear due to non-logarithmic functions in the cross sections summarized in table 2. For compactness, we write all the relevant soft functions as

$$a_\kappa\mathcal{S}_\kappa^{(\text{sd})}(\xi) \equiv Q\Delta S_{\text{sd}}^{\kappa[1]}(Q\xi,\alpha_s(\mu)), \quad a_\kappa\mathcal{S}_\kappa^{(r_g)}(\xi) \equiv QQ_{\text{cut}}^{\frac{1}{1+\beta}}\Delta S_{r_g}^{\kappa[1]}\left(\xi QQ_{\text{cut}}^{\frac{1}{1+\beta}},r_g,\alpha_s(\mu)\right),$$

$$a_\kappa\mathcal{S}_{\kappa,\varepsilon}^{(\text{sd})}(\xi) \equiv Q\Delta S_{\text{sd},\varepsilon}^{\kappa[1]}(Q\xi,\alpha_s(\mu)), \quad a_\kappa\mathcal{S}_{\kappa,\varepsilon}^{(r_g)}(\xi) \equiv QQ_{\text{cut}}^{\frac{1}{1+\beta}}\Delta S_{r_g,\varepsilon}^{\kappa[1]}\left(\xi QQ_{\text{cut}}^{\frac{1}{1+\beta}},r_g,\alpha_s(\mu)\right).$$

$$\tag{6.23}$$

where we have defined $a_\kappa \equiv \alpha_s(\mu) C_\kappa / \pi$, and have left the r_g-dependence of $\mathcal{S}_\kappa^{(r_g)}$ and $\mathcal{S}_{\kappa,\varepsilon}^{(r_g)}$ implicit. Next, since we do not intend to match the max-R_g cross section with other regimes for boundary cross section, we can directly consider the r_g-derivative. This will help us avoid considering some of the more complicated cross terms not shown in table 2. The r_g-derivatives of the soft functions are given by

$$Q_{\text{cut}}^{\frac{1}{1+\beta}} \partial_{r_g} \Delta S_{r_g}^{\kappa[1]}\left(\ell^+ Q_{\text{cut}}^{\frac{1}{1+\beta}}, r_g, \alpha_s(\mu)\right) = \frac{2\alpha_s C_\kappa}{\pi} \frac{\Theta(\ell^+ - Q_{\text{cut}}' v(r_g))}{\ell^+}, \tag{6.24}$$

$$Q_{\text{cut}}^{\frac{1}{1+\beta}} \partial_{r_g} \Delta S_{r_g,\varepsilon}^{\kappa[1]}\left(\ell^+ Q_{\text{cut}}^{\frac{1}{1+\beta}}, r_g, \alpha_s(\mu)\right) = \frac{2}{2+\beta} \frac{\alpha_s C_\kappa}{\pi} \frac{1}{\xi_0'} \left(\frac{r_g}{v(r_g)}\right)^2 \partial_{r_g} v(r_g) \delta(\ell^+ - Q_{\text{cut}}' v(r_g)).$$

Next, we write

$$\mathcal{Q}_\kappa^{[1]X}(\Omega) \equiv a_\kappa \frac{e^{\gamma_E \Omega}}{\Gamma(-\Omega)} \left(\delta_{X,\text{plain}} \mathcal{R}_\kappa^{(\text{sd})}(\Omega) + \mathcal{R}_\kappa^{(r_g)}(\Omega)\right), \tag{6.25}$$

$$\mathcal{Q}_\kappa^{[2]X}(\Omega) \equiv a_\kappa^2 \frac{e^{\gamma_E \Omega}}{\Gamma(-\Omega)} \delta_{X,\text{plain}} \mathcal{R}_\kappa^{(\text{sd},r_g)}(\Omega),$$

$$\partial_{r_g} \mathcal{Q}_{\kappa,\varepsilon}^{[1]X}(\Omega) \equiv a_\kappa \frac{2}{2+\beta} \frac{e^{\gamma_E \Omega}}{\Gamma(-\Omega)} \frac{\Psi(\xi, r_g)}{\xi} \mathcal{R}_{\kappa,\varepsilon}'^{(r_g)}(\Omega),$$

$$\partial_{r_g} \mathcal{Q}_{\kappa,\varepsilon}^{[2]X}(\Omega) \equiv a_\kappa^2 \frac{2}{2+\beta} \frac{e^{\gamma_E \Omega}}{\Gamma(-\Omega)} \frac{\Psi(\xi, r_g)}{\xi} \sum_{AB \in \{\text{sd}, r_g\}_X} \mathcal{R}_{\kappa,\varepsilon}'^{AB}(\Omega),$$

where $X \in \{\text{plain, sd res.}\}$ and the set $\{\text{sd}, r_g\}_X$ refers to the combinations of soft functions in eq. (6.23) relevant for plain jet mass and soft drop jet mass resummation region, as summarized in table 2. In the last two lines, for the soft drop boundary cross section we have factored out the pre-factor,

$$\Psi(\xi, r_g) \equiv \frac{\xi}{\xi_0'} \left(\frac{r_g}{v(r_g)}\right)^2 \partial_{r_g} v(r_g). \tag{6.26}$$

In terms of the rescaled-soft functions defined in eq. (6.23), from eq. (4.18) we have

$$\mathcal{R}_\kappa^{(\text{sd}/r_g)}(\Omega) = \int_0^\infty \mathrm{d}y \, \mathcal{L}_0^{-\Omega}(1-y) \, \xi \mathcal{S}_\kappa^{(\text{sd}/r_g)}(\xi y), \tag{6.27}$$

$$\mathcal{R}_\kappa^{(\text{sd},r_g)}(\Omega) = \int_0^\infty \mathrm{d}y_A \mathrm{d}y_B \, \mathcal{L}_0^{-\Omega}(1-(y_A+y_B)) \, \xi \mathcal{S}_{\kappa,\varepsilon}^{(\text{sd})}(\xi y_A) \, \xi \mathcal{S}_\kappa^{(r_g)}(\xi y_B),$$

$$\frac{\Psi(\xi, r_g)}{\xi} \frac{2}{2+\beta} \mathcal{R}_{\kappa,\varepsilon}'^{(r_g)}(\Omega) = \int_0^\infty \mathrm{d}y \, \mathcal{L}_0^{-\Omega}(1-y) \, \xi \partial_{r_g} \mathcal{S}_{\kappa,\varepsilon}^{r_g}(\xi y),$$

$$\frac{\Psi(\xi, r_g)}{\xi} \frac{2}{2+\beta} \mathcal{R}_{\kappa,\varepsilon}'^{AB}(\Omega) = \int_0^\infty \mathrm{d}y_A \mathrm{d}y_B \, \mathcal{L}_0^{-\Omega}(1-(y_A+y_B)) \partial_{r_g} \left[\xi \mathcal{S}_{\kappa,\varepsilon}^A(\xi y_A) \, \xi \mathcal{S}_\kappa^B(\xi y_B)\right].$$

To proceed further we define the functions,

$$\gamma(\xi, r_g) \equiv \frac{\xi_0' v(r_g)}{\xi}, \quad f(w) \equiv \frac{\ln(r_g^2)}{w}, \quad h(w) \equiv \frac{1}{w} \ln\left((1+\zeta^2)\left(\frac{\gamma_{\max}}{w}\right)^{\frac{2}{2+\beta}} - \zeta^2\right), \tag{6.28}$$

$$\gamma_{\max}(\xi) \equiv \frac{\xi_0'}{\xi}, \qquad f'(w) \equiv \frac{2}{w r_g}, \qquad g(w) \equiv \frac{1}{w^2}\left((1+\zeta^2)\left(\frac{\gamma_{\max}}{w}\right)^{\frac{2}{2+\beta}} - \zeta^2\right)^{-1}.$$

We see that in terms of $\gamma(\xi, r_g)$ the prefactor $\Psi(\gamma, r_g)$ using eq. (6.26) becomes

$$\Psi(\gamma, r_g) = \left(\frac{r_g}{\gamma}\right)^2 \partial_{r_g}\gamma(\xi, r_g)\,. \tag{6.29}$$

We will find it convenient later to switch variables $r_g \to \gamma$ when considering r_g-moments.

In terms of these functions we have

$$
\begin{aligned}
\xi \mathcal{S}_\kappa^{(\text{sd})}(\xi w) &= -\big[\Theta(\gamma_{\max} - w)h(w)\big]_+^{[\gamma_{\max}]}, \\
\xi \mathcal{S}_\kappa^{(r_g)}(\xi w) &= \Theta(w - \gamma)\Big[f(w) + \Theta(\gamma_{\max} - w)h(w)\Big], \\
\xi \mathcal{S}_{\kappa,\varepsilon}^{(\text{sd})}(\xi w) &= \frac{2}{2+\beta}\big[\Theta(\gamma_{\max} - w)g(w)\big]_+^{[\gamma_{\max}]}, \\
\xi \mathcal{S}_{\kappa,\varepsilon}^{(r_g)}(\xi w) &= -\frac{2}{2+\beta}\Theta(\gamma_{\max} - w)\Theta(w - \gamma)g(w)\,,
\end{aligned}
\tag{6.30}
$$

such that from eq. (6.27), the one-loop kernels are given by

$$
\begin{aligned}
\mathcal{R}_\kappa^{(\text{sd})}(\Omega) &= -\int_0^\infty \mathrm{d}w\, \mathcal{L}_0^{-\Omega}(1 - w)\big[\Theta(\gamma_{\max} - w)\Theta(w)h(w)\big]_+^{[\gamma_{\max}]}, \\
\mathcal{R}_\kappa^{(r_g)}(\Omega) &= \int_0^\infty \mathrm{d}w\, \mathcal{L}_0^{-\Omega}(1 - w)\Theta(w - \gamma)\Big[f(w) + \Theta(\gamma_{\max} - w)h(w)\Big], \\
\mathcal{R}_{\kappa,\varepsilon}'^{(r_g)}(\Omega) &= \mathcal{L}_0^{-\Omega}(1 - \gamma)\,,
\end{aligned}
\tag{6.31}
$$

and the two-loop kernels $\mathcal{R}_\kappa^{(\text{sd},r_g)}$ and $\mathcal{R}_{\kappa,\varepsilon}'^{AB}$ being

$$
\begin{aligned}
\mathcal{R}_\kappa^{(\text{sd},r_g)} &= -\int_0^\infty \mathrm{d}w\, \mathrm{d}u \mathcal{L}_0^{-\Omega}(1 - w - u)\big[\Theta(\gamma_{\max} - u)\Theta(u)h(u)\big]_+^{[\gamma_{\max}]} \\
&\qquad \times \Theta(w - \gamma)\Big[f(w) + \Theta(\gamma_{\max} - w)h(w)\Big], \\
\mathcal{R}_{\kappa,\varepsilon}'^{(\text{sd},r_g)}(\Omega) &= -\int_0^\infty \mathrm{d}w\, \mathcal{L}_0^{-\Omega}(1 - w - \gamma)\big[\Theta(\gamma_{\max} - w)\Theta(w)h(w)\big]_+^{[\gamma_{\max}]}, \\
\mathcal{R}_{\kappa,\varepsilon}'^{(r_g,\text{sd})}(\Omega) &= +\Psi^{-1}\int_0^\infty \mathrm{d}w\, \mathrm{d}u \mathcal{L}_0^{-\Omega}(1 - u - w)f'(w)\Theta(w - \gamma)\big[\Theta(\gamma_{\max} - u)\Theta(u)g(u)\big]_+^{[\gamma_{\max}]}, \\
\mathcal{R}_{\kappa,\varepsilon}'^{(r_g,r_g)}(\Omega) &= -\Psi^{-1}\int_0^\infty \mathrm{d}w\, \mathrm{d}u \mathcal{L}_0^{-\Omega}(1 - u - w)f'(w)\Theta(w - \gamma)\Theta(\gamma_{\max} - u)\Theta(u - \gamma)g(u) \\
&\qquad + \int_0^\infty \mathrm{d}w\, \mathcal{L}_0^{-\Omega}(1 - w - \gamma)\Theta(w - \gamma)\Big[f(w) + \Theta(\gamma_{\max} - w)h(w)\Big].
\end{aligned}
\tag{6.32}
$$

Note that we have not included $\mathcal{R}_{\kappa,\varepsilon}^{(\text{sd},\text{sd})}$ in the list above as it does not carry any r_g dependence and vanishes upon taking r_g-derivative.

To further compactify these expressions we introduce the following transforms acting on a function or a distribution $F(w)$:

$$
q\{F\}(u, u_{\min}) \equiv \Theta(1 - u_{\min} - u)\int_0^\infty \mathrm{d}w\, \mathcal{L}_0^{-\Omega}(1 - u - w)F(w)\Theta(w - u_{\min})\,, \tag{6.33}
$$

$$
q_+\{F\}(u, u_{\max}) \equiv \Theta(1 - u)\int_0^\infty \mathrm{d}w\, \mathcal{L}_0^{-\Omega}(1 - u - w)\big[\Theta(u_{\max} - w)\Theta(w)F(w)\big]_+^{[u_{\max}]}\,.
$$

In terms of these transforms the above expressions become

$$\mathcal{R}^{(\mathrm{sd})}_\kappa(\Omega) = -q_+\{h\}(0,\gamma_{\max})\,, \tag{6.34}$$

$$\mathcal{R}^{(r_g)}_\kappa(\Omega) = q\{f+h\}(0,\gamma) - q\{h\}(0,\gamma_{\max})\,,$$

$$\mathcal{R}^{(\mathrm{sd},r_g)}_\kappa(\Omega) = -\int_\gamma^{\min\{\gamma_{\max},1\}} \mathrm{d}w\, q_+\{h\}(w,\gamma_{\max})\Big[f(w) + \Theta(\gamma_{\max}-w)h(w)\Big]\,,$$

$$\mathcal{R}'^{(\mathrm{sd},r_g)}_{\kappa,\varepsilon}(\Omega) = -q_+\{h\}(\gamma,\gamma_{\max})\,,$$

$$\mathcal{R}'^{(r_g,\mathrm{sd})}_{\kappa,\varepsilon}(\Omega) = \Psi^{-1}\int_0^{\gamma_{\max}} \mathrm{d}u\, g(u)\Big[q\{f'\}(u,\gamma) - q\{f'\}(0,\gamma)\Big]\,,$$

$$\mathcal{R}'^{(r_g,r_g)}_{\kappa,\varepsilon}(\Omega) = -\Psi^{-1}\int_\gamma^{\gamma_{\max}} \mathrm{d}u\, g(u)\, q\{f'\}(u,\gamma) + \Big[q\{f+h\}(\gamma,\gamma) - q\{h\}(\gamma,\gamma_{\max})\Big]\,.$$

The transform on the combination $f+h$ in the second and last line is necessary to stabilize the numerical integration.

The transforms simplify to the following expressions:

$$q\{F\}(u,\,u_{\min}) = \left[\frac{F(1-u)}{-\Omega(1-u_{\min}-u)^\Omega} + \int_{u_{\min}}^{1-u} \mathrm{d}w\, \frac{F(w)-F(1-u)}{(1-w-u)^{1+\Omega}}\right]\,,$$

$$q_+\{F\}(u,\,u_{\max}) = \Theta(1-u-u_{\max})\int_0^{u_{\max}} \mathrm{d}w\, F(w)\Big[(1-w-u)^{-1-\Omega} - (1-u)^{-1-\Omega}\Big]$$

$$+ \Theta(u_{\max}-1+u)\left[\int_0^{1-u} \mathrm{d}w\left(\frac{(F(w)-F(1-u))}{(1-w-u)^{1+\Omega}} - \frac{F(w)}{(1-u)^{1+\Omega}}\right)\right.$$

$$\left.- \int_{1-u}^{u_{\max}} \mathrm{d}w\, \frac{F(w)}{(1-u)^{1+\Omega}} + \frac{F(1-u)}{-\Omega(1-u)^\Omega}\right]\,. \tag{6.35}$$

In the first expression, the w integration always sees the zero of the argument of $\mathcal{L}_0^{-\Omega}$ for every value of u. In the second expression, we see that only in the second and third line is the plus prescription of $\mathcal{L}_0^{-\Omega}$ necessary. In writing the integrals in the form shown above, we regulate singularities in $F(w)$ at $w\to 0$ and in $\mathcal{L}_0^{-\Omega}(1-u)$ for $u\to 1$. Finally, for $\Omega\to 0$ limit, the resummation is turned off and we find

$$\lim_{\Omega\to 0} \frac{e^{\gamma_E\Omega}}{\Gamma(-\Omega)} q\{F\}(u,\,u_{\min}) = \Theta(1-u_{\min}-u)F(1-u)\,, \tag{6.36}$$

$$\lim_{\Omega\to 0} \frac{e^{\gamma_E\Omega}}{\Gamma(-\Omega)} q_+\{F\}(u,\,u_{\max}) = \Big[\Theta(u_{\max}-(1-u))\Theta(1-u)F(1-u)\Big]_+^{[u_{\max}]}\,.$$

In ref. [83], the results for some of the resummation kernels above were presented in terms of incomplete beta functions and their integrals. We have checked that the results there agree with the ones above when $\zeta\to 0$ in eq. (6.28). The numerical implementation associated with this work follows the above presentation of these kernels in terms of integral transforms, and in fact results in a significantly faster and reliable code.

6.5 Fixed order cross section

Finally, we consider the non-singular corrections from using the full soft drop condition without expansions in the soft limit. In analogy with eq. (3.52) the measurement function

is given by

$$\delta_{\xi,\varepsilon}^{\mathrm{FO}}(x,y,r_g,\xi_0,\zeta) \equiv \hat{\Theta}_{k_T}(x,y)\delta_{\mathrm{sd}}(x,y,\xi_0,\zeta)[\hat{\Theta}_{r_g}(x,y,r_g)\delta(\xi-y)-\delta(\xi)]. \qquad (6.37)$$

Again restricting to $\xi > 0$ for the differential cross section we can ignore the $\delta(\xi)$ term. The two delta-functions fix both x and y, such that the fixed order cross section is given by

$$\xi\tilde{\mathcal{G}}_{\kappa,\varepsilon}^{\mathrm{FO}[1]}(\xi,r_g) = (1+\delta_{\kappa,g})j(x^*,\xi)\frac{\alpha_s}{2\pi}\hat{\Theta}_{k_T}(x^*,\xi)\hat{\Theta}_{r_g}(x^*,\xi,r_g)\sum_{\kappa'}\hat{P}_{\kappa'\kappa}(x^*) \qquad (6.38)$$

$$+ \delta_{\kappa,q}|j(1-x^*,\xi)|\frac{\alpha_s}{2\pi}\hat{\Theta}_{k_T}(x^*,\xi)\hat{\Theta}_{r_g}(x^*,\xi,r_g)\sum_{\kappa'}\hat{P}_{\kappa'\kappa}(1-x^*),$$

where x^* is the solution of the soft drop constraint in eq. (6.2) for $y = \xi$ and $j(x,y)$ is the Jacobian given by

$$j(x,y) = \left(\frac{1+y\zeta^2}{1-y\zeta^2}\right)\left(1+\frac{\beta}{2}\frac{(1-2x)(1-y\zeta^2)}{(1-x)+xy\zeta^2}\right)^{-1}. \qquad (6.39)$$

In the soft limit $(x \sim y, x \to 0)$, $j(x,y) = 2/(2+\beta)$. The δ_{sd} constraint can be easily solved for $\beta = 0$, for which we find

$$x^*(y,\xi_0,\beta=0) = 1 - \frac{1-\xi_0(1+y\zeta^2)}{1-y\zeta^2}. \qquad (6.40)$$

For other values of β we employ the following approximation which fairly well reproduces the exact solution for the range of z_{cut} and β that we consider:

$$x^*(y,\xi_0,\beta>0) \approx y^{\frac{\beta}{2+\beta}}\xi_0^{\frac{2}{2+\beta}} - y\zeta^2 + \frac{1}{4}y\zeta^2\left(\frac{z_{\mathrm{cut}}}{0.1}\right). \qquad (6.41)$$

Since the r_g-dependence in the fixed order cross section in eq. (6.38) only arises from the measurement theta-function and collinear matrix elements, to gauge the size of non-singular corrections we can simply consider the boundary soft drop cross section for $r_g = 1$. To this end we define

$$\Delta\tilde{\mathcal{G}}_{\kappa,\mathrm{sd},\varepsilon}^{\mathrm{n.s.}[1]}(\xi,\alpha_s(\mu_N)) \equiv \tilde{\mathcal{G}}_{\kappa,\varepsilon}^{\mathrm{FO}}(\xi,r_g=1) - Q\Delta S_{\mathrm{sd},\varepsilon}^{\kappa}(Q\xi,Q_{\mathrm{cut}},\zeta,\beta,\alpha_s(\mu_N)). \qquad (6.42)$$

In figure 12 we show the size of the non-singular correction relative to the fixed-order result. We see that the deviation is below 5% which we will find to be well within the perturbative uncertainties.

6.6 R_g-weighted boundary soft drop cross section

Having discussed the construction of the soft drop boundary cross section we now use it to compute the r_g moments. The first step is to combine the results in the plain jet mass and soft drop resummation regions to compute the matched cross section. This is straightforwardly obtained by repeating the steps for the max-R_g cross section in eq. (5.1):

$$\tilde{\mathcal{G}}_{\kappa,\varepsilon}^{\mathrm{match}}(\xi,r_g) \equiv \tilde{\mathcal{G}}_{\kappa,\varepsilon}^{\mathrm{sd}}(\xi,r_g,\mu_{\mathrm{sd}\to\mathrm{plain}}) + [\tilde{\mathcal{G}}_{\kappa,\varepsilon}^{\mathrm{plain}}(\xi,r_g,\mu_{\mathrm{plain}}) - \tilde{\mathcal{G}}_{\kappa,\varepsilon}^{\mathrm{sd}}(\xi,r_g,\mu_{\mathrm{plain}})]. \qquad (6.43)$$
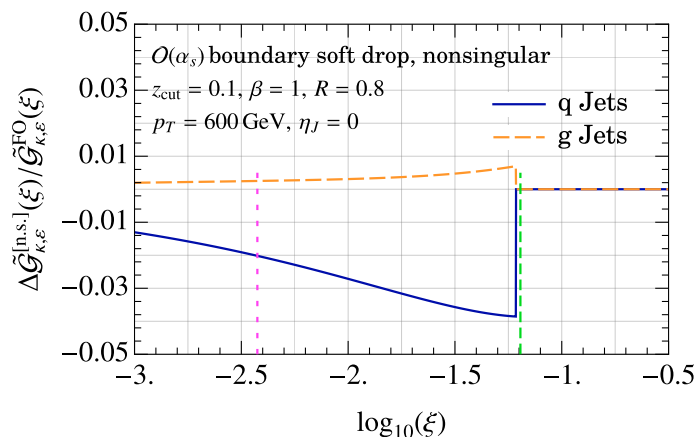
Figure 12. Relative size of non-singular corrections to the boundary soft drop cross section. Using the full soft drop condition shifts the cusp slightly to the left of ξ_0' (green-dashed vertical line).

Using this result, we can compute the $C_{2\kappa}^{(n)}(\xi)$ moments:

$$C_{2\kappa}^{(n)}(\xi) = \frac{\xi}{\tilde{\mathcal{G}}_\kappa^{\text{match}}(\xi)} \int_{r_g^{\text{min}}(\xi)}^{r_g^{\text{max}}(\xi)} \mathrm{d}r_g \, r_g^n \, w_{\text{sd}\to\text{plain}}(\xi, r_g) \frac{\mathrm{d}\tilde{\mathcal{G}}_{\kappa,\varepsilon}^{\text{match}}(\xi, r_g)}{\mathrm{d}r_g} \,. \tag{6.44}$$

Next, we note that the cross section $\partial_{r_g}\tilde{\mathcal{G}}_{\kappa,\varepsilon}^{\text{match}}(\xi, r_g)$ is proportional to $\Psi(\xi, r_g)$ defined in eq. (6.26):

$$\xi \frac{\mathrm{d}\tilde{\mathcal{G}}_{\kappa,\varepsilon}^{\text{match}}(\xi, r_g)}{\mathrm{d}r_g} = \Psi(\xi, r_g) \, \mathcal{F}_{\kappa,\varepsilon}^{\text{match}}(\xi, r_g) \,, \tag{6.45}$$

and have factored out the pre-factor in eq. (6.24), such that using eq. (6.29) $C_{2\kappa}^{(n)}(\xi)$ in eq. (6.44) becomes

$$C_{2\kappa}^{(n)}(\xi) = \frac{1}{\tilde{\mathcal{G}}^{\text{match}}(\xi)} \int_{\gamma_{\text{min}}(\xi)}^{\min\{1,\gamma_{\text{max}}(\xi)\}} \mathrm{d}\gamma \, [r_g(\gamma)]^n \left(\frac{r_g^{\text{max}}(\xi\gamma)}{\gamma}\right)^2 \mathcal{F}_{\kappa,\varepsilon}^{\text{match}}(\xi, r_g^{\text{max}}(\xi\gamma)) \,, \tag{6.46}$$

where

$$r_g(\xi,\gamma) \equiv r_g^{\text{max}}(\xi\gamma) \,, \qquad \gamma_{\text{min}}(\xi) \equiv \frac{\xi_0' v(\sqrt{\xi})}{\xi} \,, \qquad \gamma_{\text{max}}(\xi) = \frac{\xi_0'}{\xi} \,. \tag{6.47}$$

In figure 13 we demonstrate how the matching for $C_{2\kappa}^{(-1)}$ works. We see that the overlap piece completely cancels the soft drop resummed cross section in the plain jet mass region and the plain jet mass cross section in the soft drop resummation region. In figure 14 we show the impact of scale variations and the variation of the nuisance parmaeter $a_{20,\varepsilon}^{\text{max}}$ for two-loop non-logarithmic pieces for $C_{2\kappa}^{(-1,2)}$ moments. Unlike the doubly differential cross section considered in the previous section the boundary cross section is not directly related to single differential jet mass cross section. As a result we find a significant impact of scale variation left in the ratio, which dominates the nuisance parmaeter variation. The variations for $C_{2\kappa}^{(2)}$ are somewhat smaller than those of the $C_{2\kappa}^{(-1)}$ moment. This is because for positive moments $n = 2$, the contribution from the int-R_g and min-R_g regions is naturally power suppressed. The scale variations for small r_g tend to be larger due to smaller scales being probed.
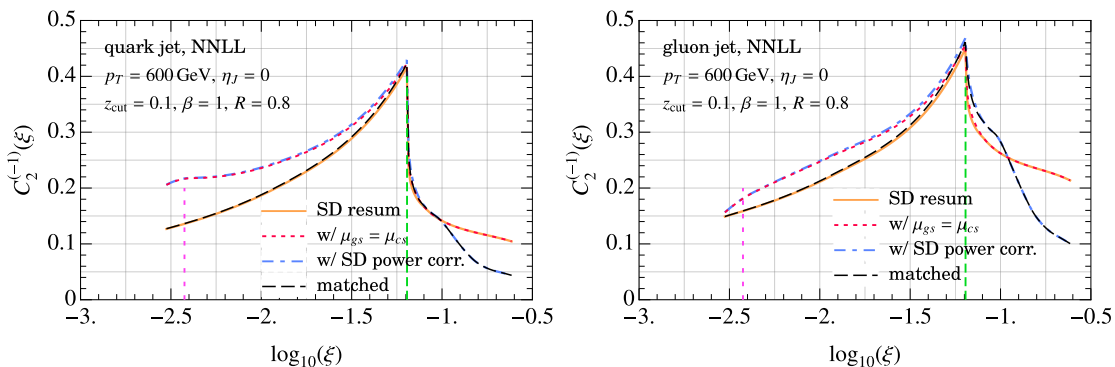
Figure 13. Matching the result for $C_{2\kappa}^{(n)}$ for $n = -1$ for quark and gluon jets across the soft drop resummation and plain jet mass regions. The vertical lines denote the extent of the SDOE region.
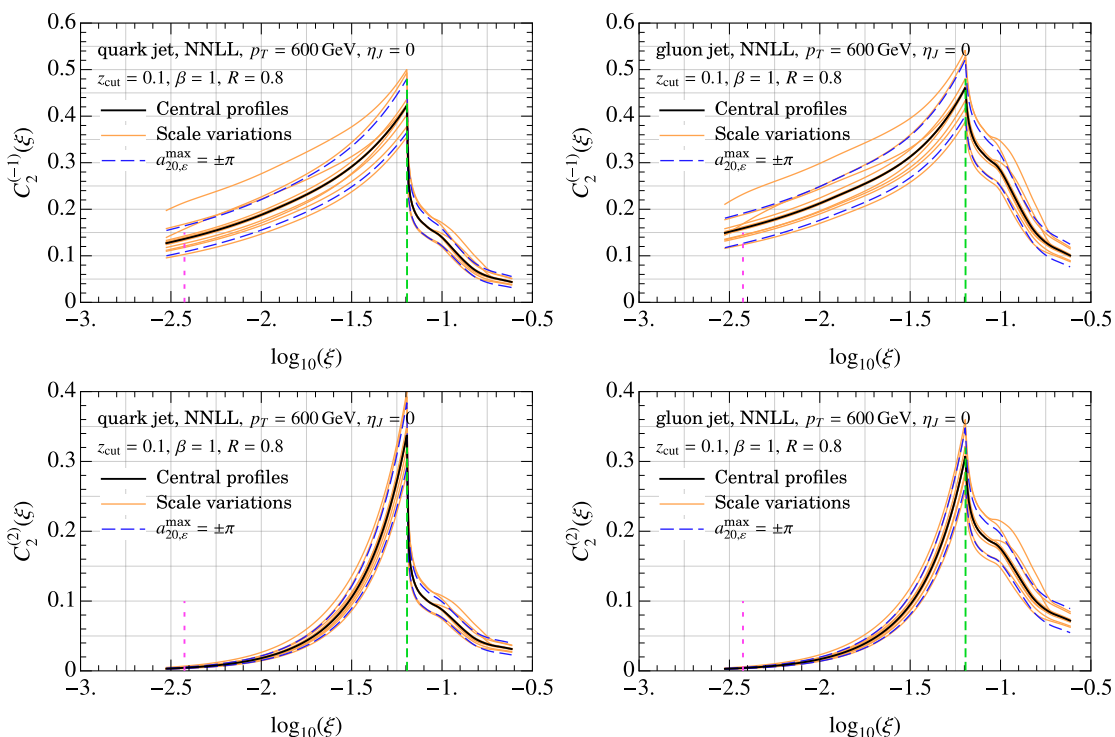

Figure 14. $C_{2\kappa}^{(n)}$ for $n = -1$ (top) and $n = 2$ (bottom) for quark and gluon jets. The vertical lines denote the extent of the SDOE region.

7 Comparison with previous results

Having discussed the NNLL computation of the Wilson coefficients we now investigate the impact of improvements achieved in this work from matching to the plain jet mass region. In figure 15 we show the comparison of NNLL results for $C_{1q}^{(1)}$ and $C_{2q}^{(1)}$ and the previous result derived in ref. [83], taking the $e^+e^- \to q\bar{q}$ process for illustration. A comparison with LL and NLL results, as well as with a computation in the coherent branching framework can be found in ref. [83]. Crucially, in the NLL$'$ calculation in ref. [83] the power corrections
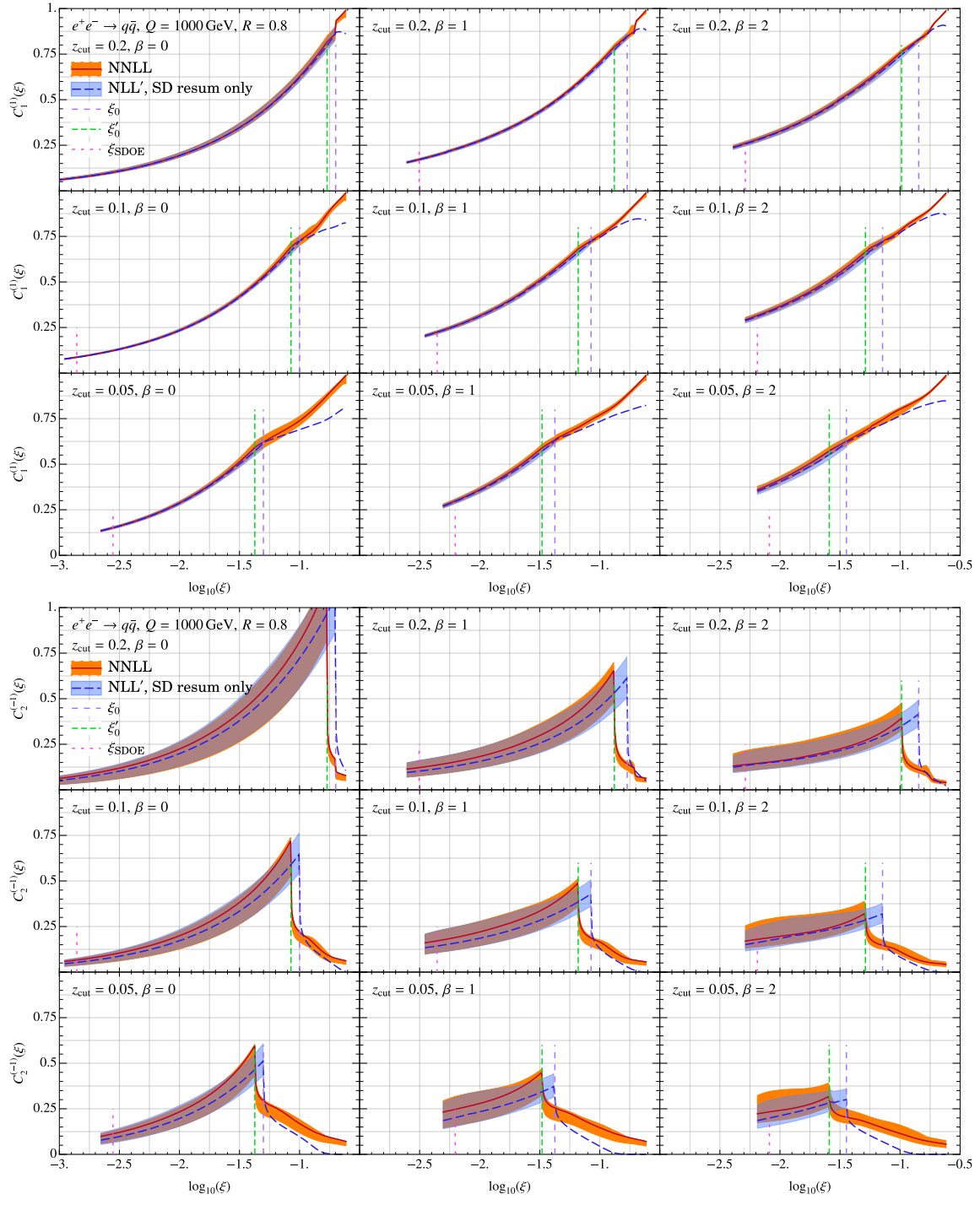
Figure 15. Comparison of NNLL prediction of $C_1^{(1)}$ and $C_2^{(-1)}$ against the NLL′ prediction from ref. [83] in the soft drop resummation region.
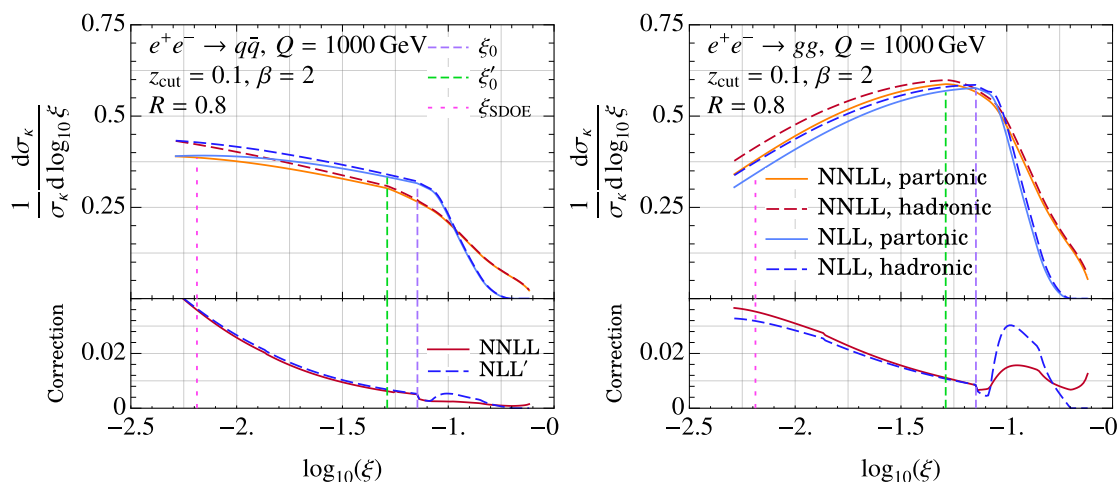
Figure 16. Hadronization corrections in the jet mass spectrum by combining the Wilson coefficients and the corresponding moments following eq. (1.3). The insets show correction to the parton level curve for two different calculations of perturbative weights. The same sets of legends apply to both plots and the corresponding insets.

associated with the max-R_g regime in the soft drop resummation region shown in eq. (4.23) were systematically dropped. Hence, the result is not valid close to the soft drop cusp and beyond. For this reason we only show the central curve in figure 15 obtained by simply switching from soft drop to plain jet mass resummation profiles. Our NNLL calculation reveals that the power corrections from matching to the plain jet mass region are not large in the region $\xi < \xi'_0 < \xi_0$ for typical grooming parameters. For both $C_{1\kappa}^{(1)}$ and $C_{2\kappa}^{(-1)}$ the difference in the region where the two results overlap, however, becomes significant for low grooming cases such as $z_{\text{cut}} = 0.05$ and $\beta = 2$. On the other hand, we see a significant impact on $C_{2\kappa}^{(-1)}$ from the shift of the soft drop cusp from the NLL location, ξ_0, to NNLL location, ξ'_0. We now investigate the impact of this shift on the cusp location on the numerical size of the power corrections.

We first assess the improvements in the perturbative weights achieved in this work by considering the impact on the jet mass spectrum. We note that the NLL jet mass spectrum exhibits cusp at ξ_0, whereas the NNLL (or NLL$'$) spectrum at ξ'_0. To include hadronization corrections consistently we must ensure that this is also the case for the Wilson coefficients. In figure 16 we combine the NLL$'$ results for perturbative weights from ref. [83] without $(\xi/\xi_0)^{1/(2+\beta)}$ soft drop power corrections with the NLL jet mass spectrum, and the NNLL results derived in this work (including these power corrections) with the NNLL jet mass spectrum. Here, as a reference, we used $\{\Omega_{1q}^{\circledcirc}, \Upsilon_{1,0q}^{\circledcirc}, \Upsilon_{1,1q}^{\circledcirc}\} = \{0.55, -0.57, 1.06\}$ obtained from fitting to `Pythia 8.3` hadronization model in ref. [92].[8] As can be seen in the top panel, figure 16, the nonperturbative corrections start to grow as we reduce the jet masses past the respective cusp location shown in dashed vertical lines. We find, however, that the correction to the parton level for two different calculations of perturbative weights shown in

---

[8]These values are chosen purely for illustration purposes and we do not claim to have determined these parameters by fitting to `Pythia 8.3`.
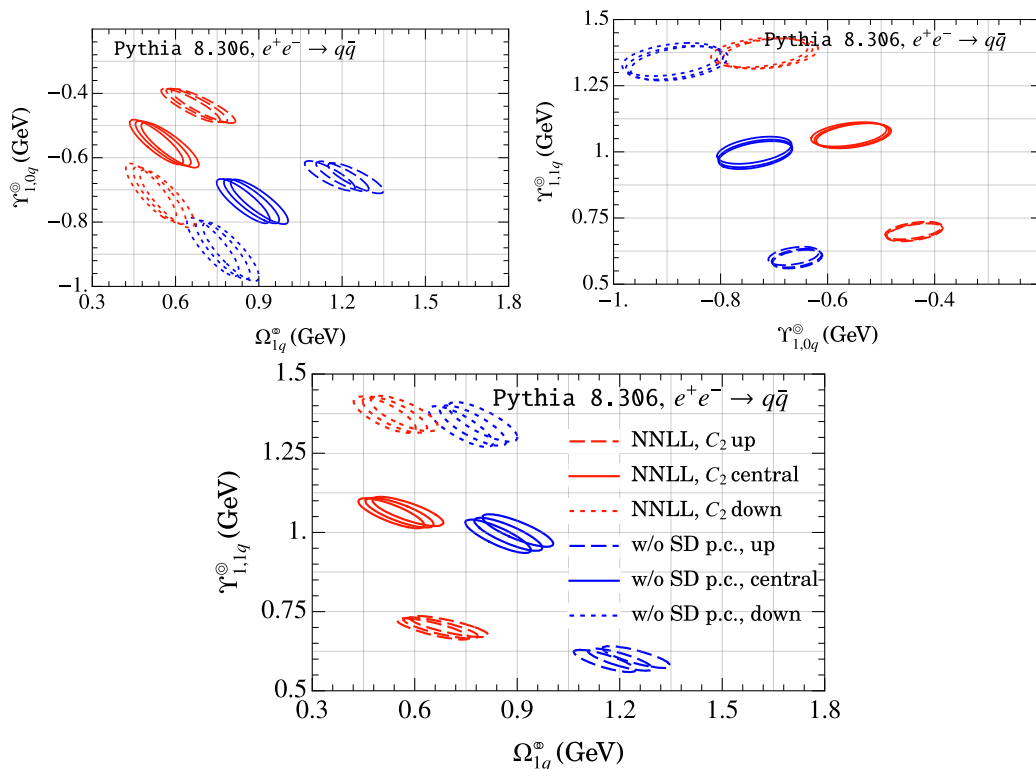
Figure 17. Results of fitting to `Pythia 8.3` using NNLL $C_\kappa^{(n)}$ coefficients and with dropping soft drop power corrections.

the bottom inset differs significantly only beyond the cusp at ξ_0, with the NNLL calculation being the reliable one in this region.

We can further investigate this effect by carrying out simple Monte Carlo fitting analysis along the lines of ref. [92]. More specifically, we treat the parton shower prediction in the MC as the perturbative calculation and fit for the nonperturbative parameters $\{\Omega_{1q}^{\circledcirc}, \Upsilon_{1,0q}^{\circledcirc}, \Upsilon_{1,1q}^{\circledcirc}\}$ in $e^+e^- \to q\bar{q}$ process by comparing it with the hadron level curve and using analytical calculations of the Wilson coefficients. We consider two different cases where calculation of Wilson coefficients in ref. [83] without soft drop power corrections and the NNLL calculation of this work is employed. When fitting using the NNLL result of this work, we take the fit region to be $\xi \in (\xi_{\mathrm{SDOE}}, \xi_0')$, where ξ_{SDOE} was defined above in eq. (2.15) and with ρ in eq. (2.15) chosen to be 4.5 [92]. On the other hand, since in the NLL$'$ calculation of ref. [83] the soft drop power corrections were systematically dropped, it is natural to choose the fit range to be $\xi \in (\xi_{\mathrm{SDOE}}, \xi_0)$. Additionally, following the procedure of ref. [92], we interpret the uncertainty in the extractions of these moments by varying the Wilson coefficients within their respective uncertainty bands shown in figure 15. In figure 17 we show the results of this fitting procedure. The dominant uncertainty comes from variations in $C_{2\kappa}^{(-1)}$ which are shown as dotted and dashed ellipses, whereas the uncertainty in $C_{1\kappa}^{(1)}$ being small leads to tighter variations. From the spread of the ellipses we can gauge that the two fit results are compatible. However, the fit results for NLL$'$ computation, where soft

drop power corrections are also dropped, lead to larger uncertainty (and a slightly lower χ^2 value). Thus, the improved calculation with matching in the plain jet mass region enables a more precise calibration of hadronization models in terms of soft drop nonperturbative parameters. At the same time, through this comparison it is reassuring to see that by including power corrections, we do not significantly alter the outcome the determination of these parameters. A discussion on how the choice of lower end of the fit range ξ_{SDOE} impacts the fit results can be found in ref. [92].

Finally, we note that in figure 16 we have not truncated the hadronization corrections in the ungroomed region, and have incorporated as shown in eq. (1.3) also for jet masses larger than the respective cusp locations. While the prescription of eq. (1.3) is strictly valid only in the SDOE region, this approach nevertheless captures the main features of transition from the groomed to ungroomed region. This is because the $C_{2\kappa}^{(-1)}$ coefficient which is specific to effects of soft drop automatically becomes small in the ungroomed region for $\xi > \xi_0, \xi_0'$, whereas the $C_{1\kappa}^{(1)}$ coefficient tends to 1, the value at the jet radius boundary. This is consistent with the behavior expected in the ungroomed region as described in eq. (1.2). However, because of the jet boundary, the dipole geometry valid in the SDOE region gets distorted, and as such $\Omega_{1\kappa}^{\circledcirc}$ is a distinct moment from $\Omega_{\kappa}^{(1)}$ for the ungroomed region. Nevertheless, the power corrections are very small in this region and numerically the differences between these two moments may be ignored. Hence, our NNLL result valid throughout the jet mass spectrum provides a starting point for matching the nonperturbative power corrections across the two regions.

8 Comparison with simulations

In this section we show a comparison of the numerical implementation of the NNLL calculation of the moments above against simulations of quarks and gluon jets in e^+e^- and pp collisions in `Pythia 8.3` and `Herwig 7.2`. For `Pythia 8.3` simulations we employ the default p_T-ordered shower and for `Herwig 7.2` the default angular-ordered shower. Both parton showers are simulated with LO hard process. Below we only show results for parton-level predictions and do not turn on hadronization and underlying event models. In the simulations we reconstruct anti-k_T [99] jets using `Fastjet` [100], and analyze them using jet analysis software `JETlib` [101]. We note that since the parton shower results are $\sim$ LL accurate, we do not anticipate a perfect agreement with the more precise NNLL results. Nevertheless, we will see below that the parton shower results are largely in agreement with analytical calculations within perturbative uncertainty.

8.1 Results for C_1

In figure 18 we show compare the analytical prediction for $C_{1\kappa}^{(n)}$ for phenomenologically relevant cases of $n = 1, 4$ for quark jets in $e^+e^- \to q\bar{q}$ parton level process simulated at leading order for all combinations of $z_{\mathrm{cut}} \in \{0.05, 0.1, 0.2\}$ (rows) and $\beta \in \{0, 1, 2\}$ (columns). We will stick to leading order treatment of the hard scattering since the main goal of this work is the hadronization model and its interface with the parton shower which can be well isolated with the help of soft drop in the SDOE region. Within the SDOE region shown

between the vertical lines we find the MC extraction to agree very well with the analytical result, and we expect this to work even when higher order hard matching corrections are included. Beyond the cusp, however, we expect that the prediction for $\xi_0 < \xi \lesssim 1$ to be modified with more precise matching to account for additional jets, though continue to find a very good agreement for e^+e^- collisions for our LO simulations. We have also shown the result for the central curve of NLL$'$ calculation without soft drop power corrections in dashed line. We also simulate the $e^+e^- \to h_0 \to gg$ process to study gluon jets in isolation shown in figure 19 and find similar results as quark jets.

In figures 20 and 21 we compare the analytical prediction for quarks and gluon jets in pp collisions against simulations. Here we simulate $pp \to Z + q/g$ jet process and sample the leading jet. We see that both MC simulations yield almost identical results and agree with the NNLL result in the SDOE region, though there are some small noticeable differences for $\beta = 2$ case. We find that despite the differences in the theory setup for inclusive jets and the jet selection criteria in simulations they remain close to the analytical result in the plain jet mass region for many of the z_{cut}, β combinations.

8.2 Results for C_2

Next, we show a comparison of NNLL results for $C_{2\kappa}^{(n)}$ for $n = -1, 2$ and parton level simulations for the same processes as considered above. Here we use an improved method for extracting of $C_{2\kappa}^{(n)}$ moments from parton showers than what was originally employed in ref. [82]. In ref. [82] the soft drop condition was shifted by a small amount ε/r_g to result in a new constraint $\Theta(z - \xi_0 r_g^\beta + \varepsilon/r_g)$ which upon numerically differentiating with respect to ε resulted in the $C_{2\kappa}^{(-1)}$ moment. This approach however fails to work for positive moments that we consider because for small angles and $n > 0$ the shift εr_g^n becomes too small for numerical differentiation. Instead, we calculate $C_{2\kappa}^{(n)}$ here via a weighted cross-section given by

$$C_{2\kappa}^{\mathrm{MC},(n)}(\xi) = \frac{\xi}{\mathrm{d}\hat{\sigma}_\kappa^{\mathrm{MC}}/\mathrm{d}\xi} \int \mathrm{d}r_g \sum_{\varepsilon_i} \frac{a_i^{\mathrm{fd}}}{\left(r_g^{\mathrm{max}}(\xi)\right)^\beta \varepsilon} r_g^n w_{\mathrm{sd}\to\mathrm{plain}}(\xi, r_g) \frac{\mathrm{d}\hat{\sigma}_\kappa^{\mathrm{MC}}(\varepsilon_i)}{\mathrm{d}r_g \mathrm{d}\xi} \tag{8.1}$$

where $\frac{\mathrm{d}\hat{\sigma}_\kappa^{\mathrm{MC}}(\varepsilon_i)}{\mathrm{d}r_g \mathrm{d}\xi}$ is obtained by differentiating the jet with the shifted soft drop condition

$$\Theta_{\mathrm{sd}}^{\mathrm{MC}}(\varepsilon) \equiv \Theta\left(z - \xi_0 r_g^\beta + \varepsilon\left(r_g^{\mathrm{max}}(\xi)\right)^\beta\right), \tag{8.2}$$

for a range of uniformly spaced $\{\varepsilon_i\}$ choices and the corresponding finite difference coefficients $\{a_i^{\mathrm{fd}}\}$ to build in numerical derivative. Doing so ensure that the shifted term remains commensurate in size with the $\xi_0 r_g^\beta$ term.

The results for $e^+e^- \to q\bar{q}$ process are shown in figure 22. Unlike in the case of $C_{1\kappa}^{(n)}$, the simulations in `Pythia` and `Herwig` do not agree with each other for $\beta > 0$. Nevertheless, for all combinations of z_{cut} and β shown the simulations agree with analytical calculations within the NNLL uncertainty band, with the `Herwig` result being closer to the central curve. Comparing $n = -1$ and $n = 2$ we see a better agreement between the analytical results and simulations for $n = 2$. This is due to the fact that for $n = -1$ there is larger weight associated with smaller angles in eq. (8.1) which we need to manually eliminate using the
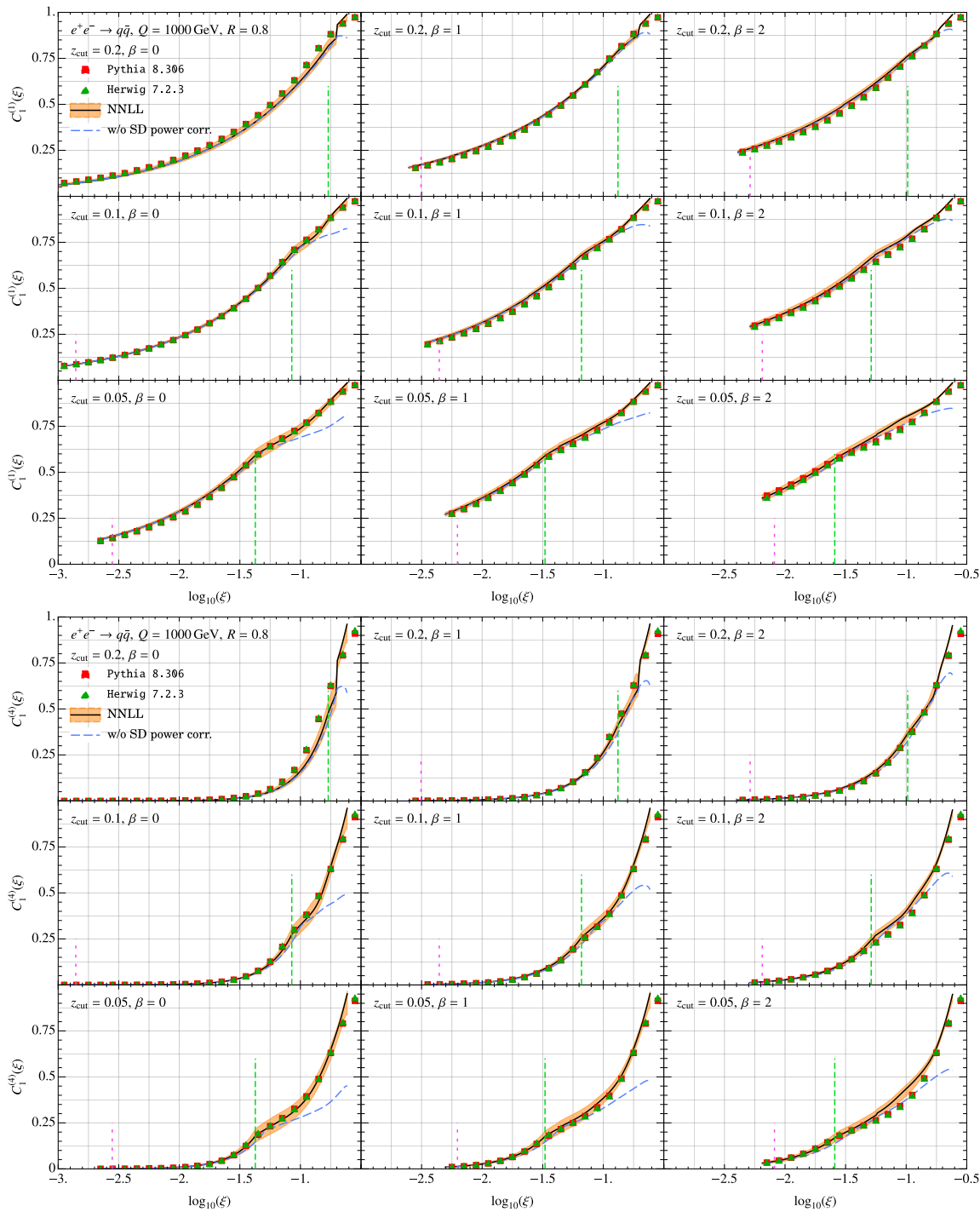
Figure 18. Comparison of NNLL prediction of $C_1^{(1)}$ (top) and $C_1^{(4)}$ (bottom) against parton level simulations of quark jets in e^+e^- collisions in `Pythia 8.3` and `Herwig 7.2`.
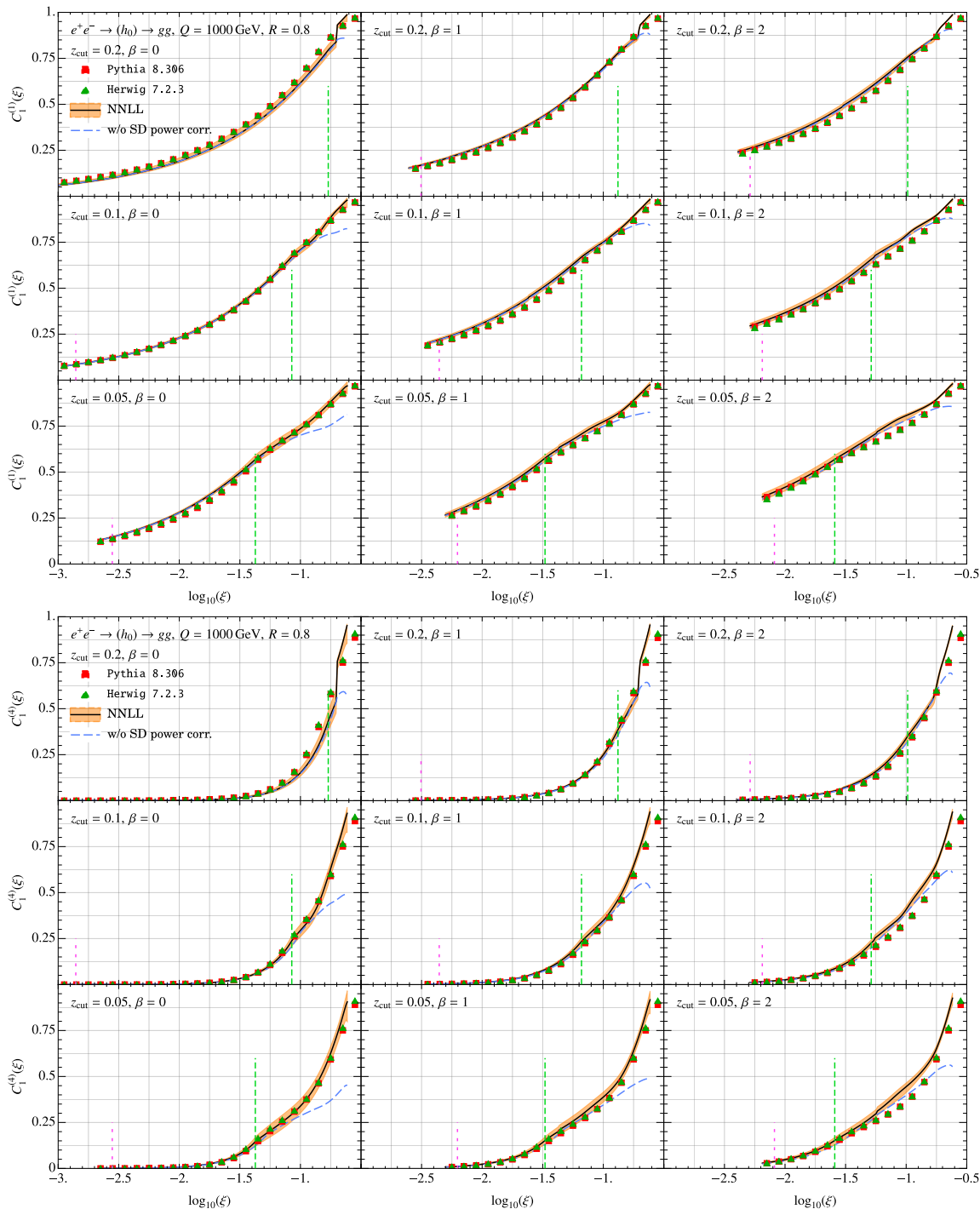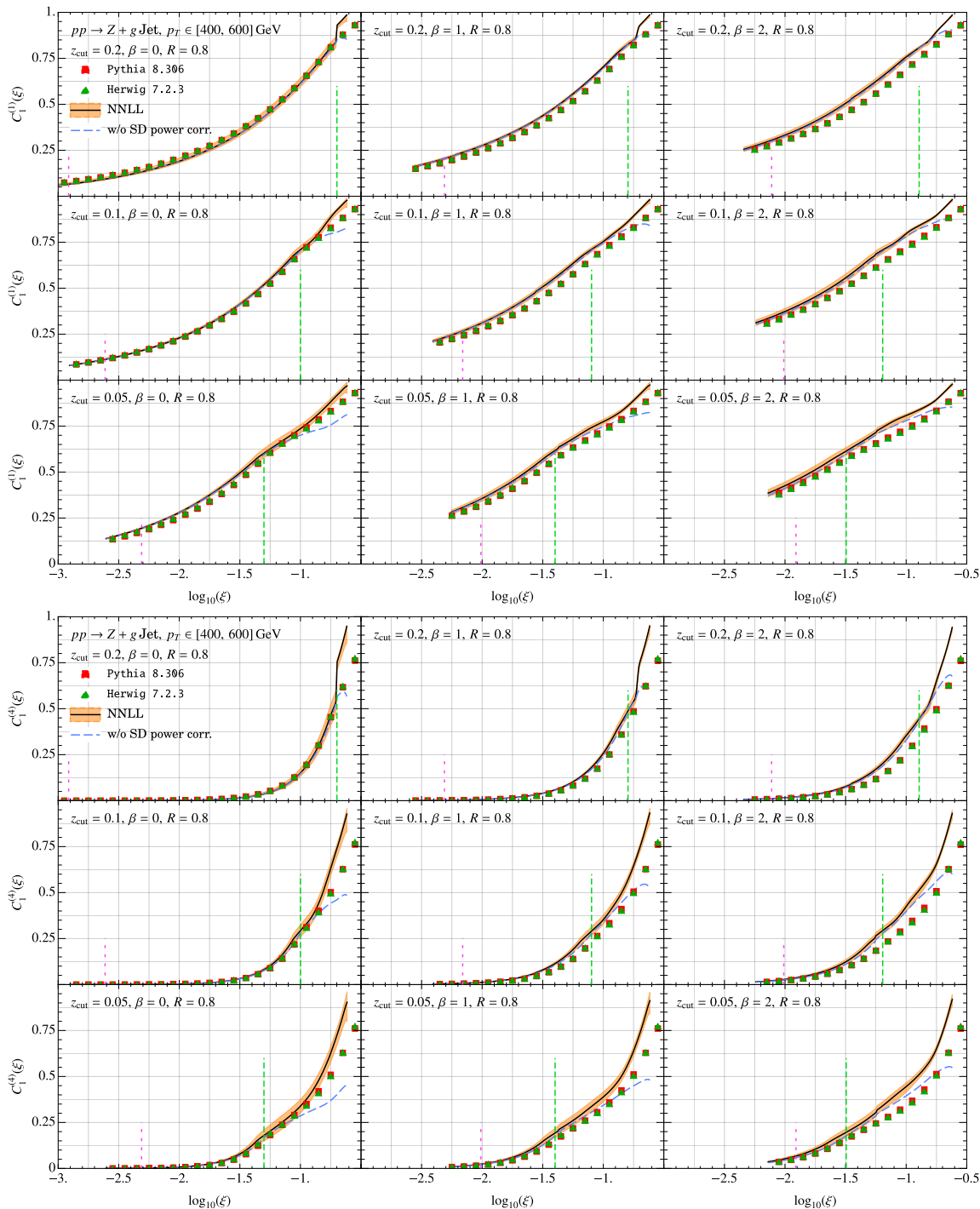
Figure 19. Comparison of NNLL prediction of $C_1^{(1)}$ and $C_1^{(4)}$ against parton level simulations of gluon jets in isolation in `Pythia 8.3` and `Herwig 7.2`.
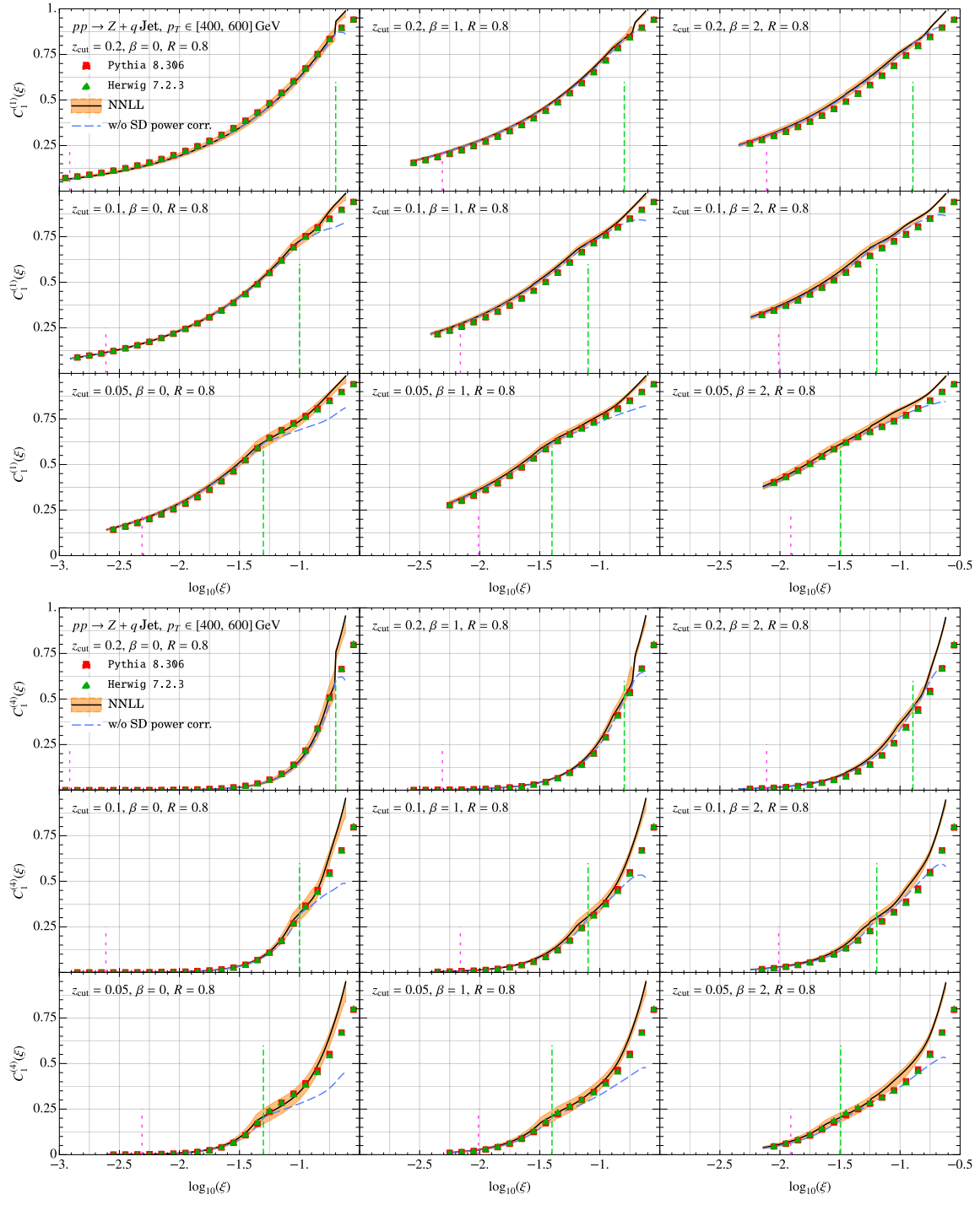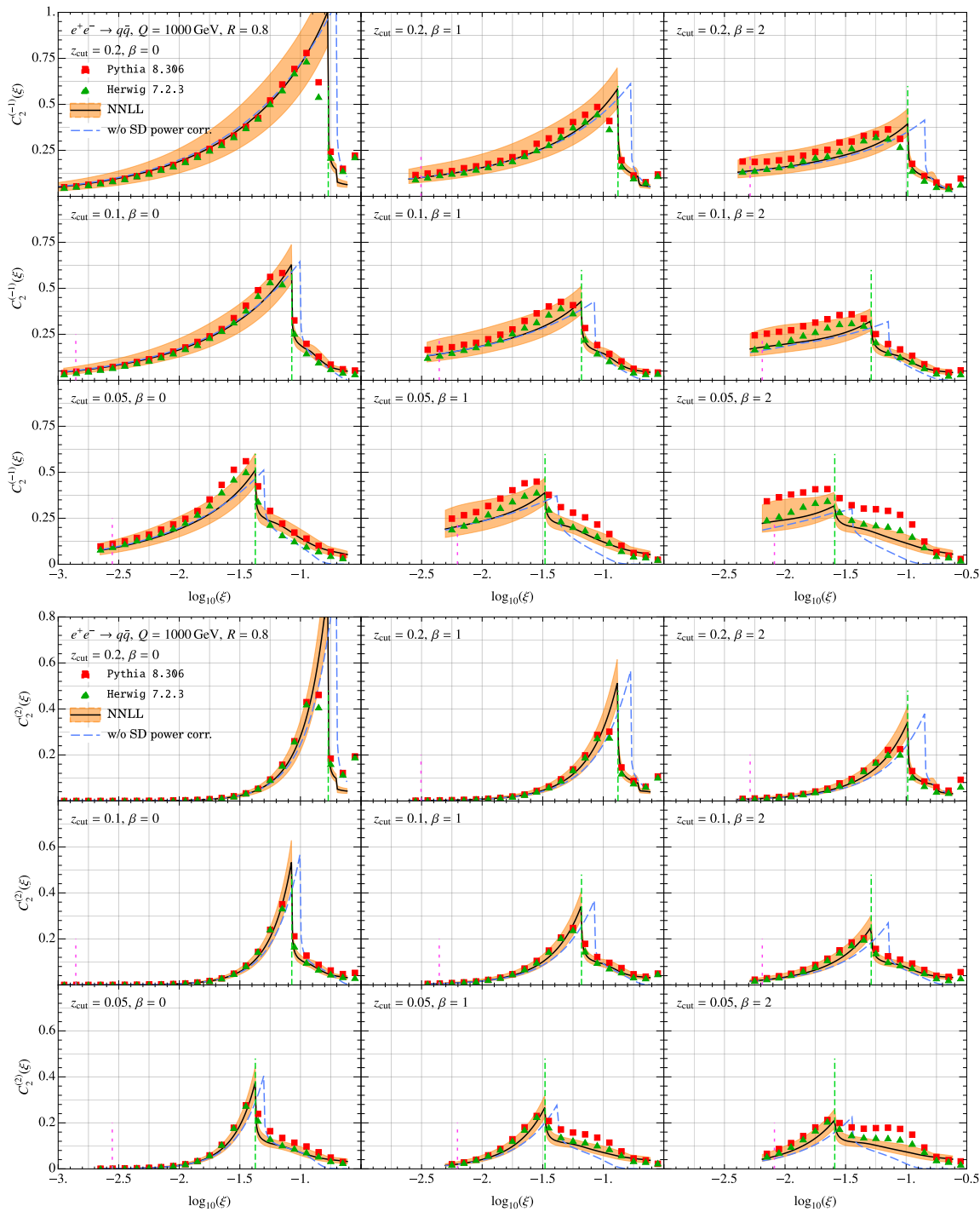
Figure 20. Comparison of NNLL prediction of $C_1^{(1)}$ (top) and $C_1^{(4)}$ (bottom) against parton level simulations of quark jets in pp collisions in `Pythia 8.3` and `Herwig 7.2`.

Figure 21. Comparison of NNLL prediction of $C_1^{(1)}$ and $C_1^{(4)}$ against parton level simulations of gluon jets in pp collisions in `Pythia 8.3` and `Herwig 7.2`.

Figure 22. Comparison of NNLL prediction of $C_{2\kappa}^{(-1)}$ and $C_{2\kappa}^{(2)}$ against parton level simulations in `Pythia 8.3` and `Herwig 7.2`.

weight function to capture only the max-R_g regime contribution. We have also displayed for comparison the NLL$'$ result from ref. [83]. We see that including soft drop power corrections results in a more accurate location of the cusp and agrees better with simulations. This is particularly noticeable for $\beta = 1, 2$. In figure 23 we show the results for gluon jets simulated in e^+e^- collisions and can draw similar conclusions as the quark case.

In figures 24 and 25 comparison of analytical results with simulations in pp collisions for quark and gluon jets is shown. Contrary to the e^+e^- case the simulations differ significantly in the plain jet mass region due to additional inevitable contribution from the initial state radiation. In the SDOE region, the analytical result agrees with the simulations, except however for the $n = -1$ moment, there is a disagreement for jet masses closer to the cusp. These differences for pp collisions between our analytical results and MC simulations are however not troublesome since we expect the contribution of ISR to nonperturbative effects to be proportional to $C_{2\kappa}^{(2)}$, which is suppressed relative to that of the collinear-soft radiation within the jet. Thus, as far as the nonperturbative corrections associated with boundary soft drop are concerned, the same moment $C_{2\kappa}^{(-1)}$ describes both e^+e^- and pp scenario. For $n = 2$ moment, we however find a comparatively better agreement between MC and analytical calculation in the SDOE region.

9   Conclusion

In this paper we have calculated the key ingredients required to describe hadronization and underlying event corrections to the groomed jet mass spectrum in a model independent framework. These ingredients are differential jet mass cross sections weighted by certain moments of groomed jet radius and occur in combination with universal nonperturbative $\mathcal{O}(\Lambda_{\text{QCD}})$ constants for hadronization corrections and analogous parameters for underlying event contribution to the groomed jet mass. A precise knowledge of these perturbative weights is crucial for precision measurements with soft drop jet mass as higher order calculations become available. The results for the moments associated with hadronization derived in this paper were used in ref. [55] to ascertain the ultimate precision possible on the strong coupling constant determination when all the nonperturbative power corrections are left unconstrained. At the same time, this field-theory based formalism imposes highly nontrivial constraints on the form and functional dependence of power corrections on jet kinematics and grooming parameters. This property of nonperturbative corrections can be used as a benchmark tool for improving modeling of hadronization and its interface with parton showers in event generators. The NNLL predictions for the perturbative weights calculated in this paper were employed in ref. [92] for a detailed calibration of hadronization models.

We calculated the perturbative weights associated with power corrections by computing the NNLL result for the doubly differential cross section and the boundary soft drop cross section. We improved upon the earlier calculation in ref. [83] and extended the previous result into the ungroomed region and performed a more accurate treatment of the prediction near soft drop cusp. We also accounted for the $\mathcal{O}(\alpha_s)$ non-singular corrections and parameterized the effect of two-loop non-logarithmic pieces via nuisance parameters. We compared the phenomenologically relevant R_g-moments of these cross sections against
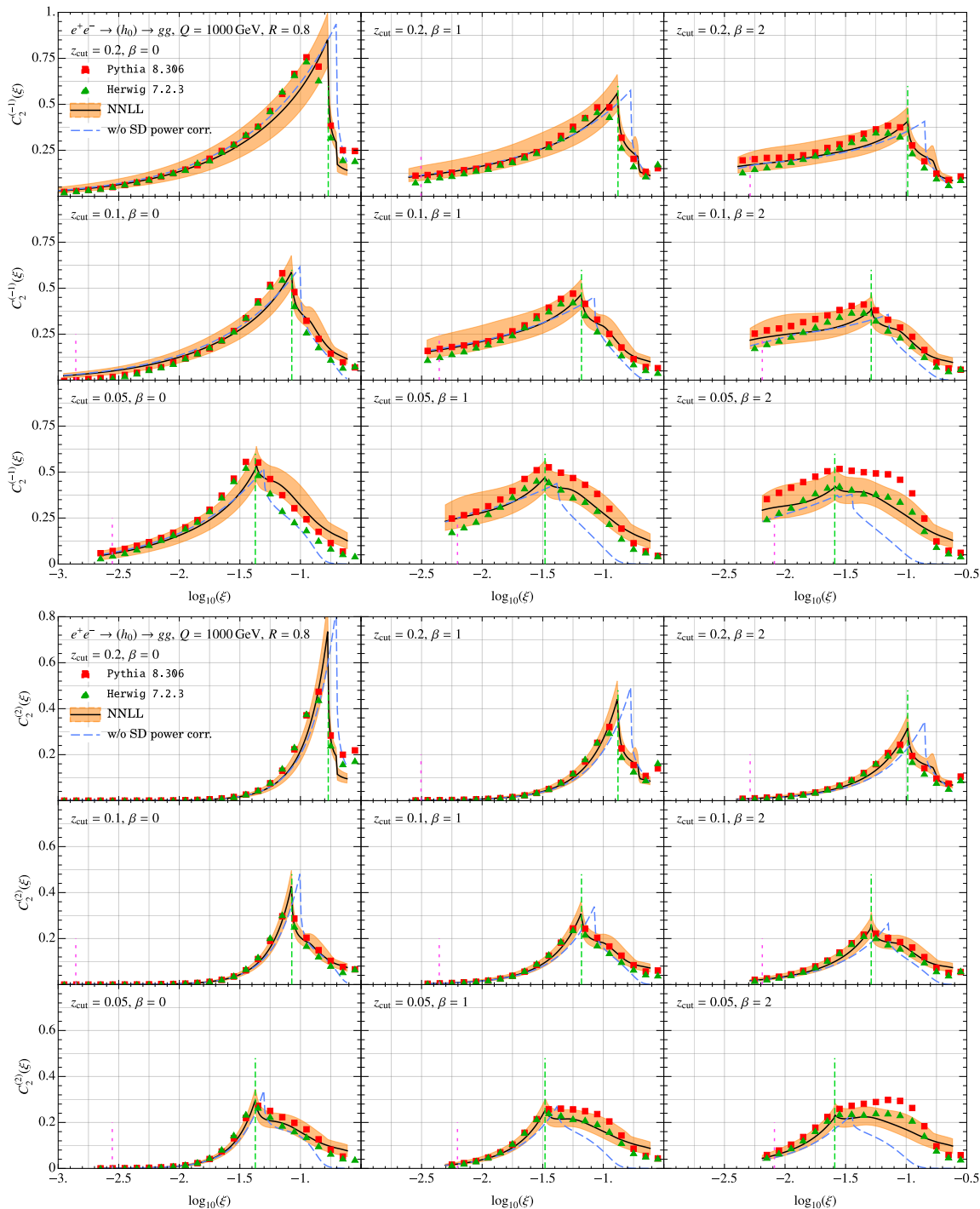
Figure 23. Comparison of NNLL prediction of $C_{2\kappa}^{(-1)}$ and $C_{2\kappa}^{(2)}$ against parton level simulations of gluon jets in isolation in `Pythia 8.3` and `Herwig 7.2`.
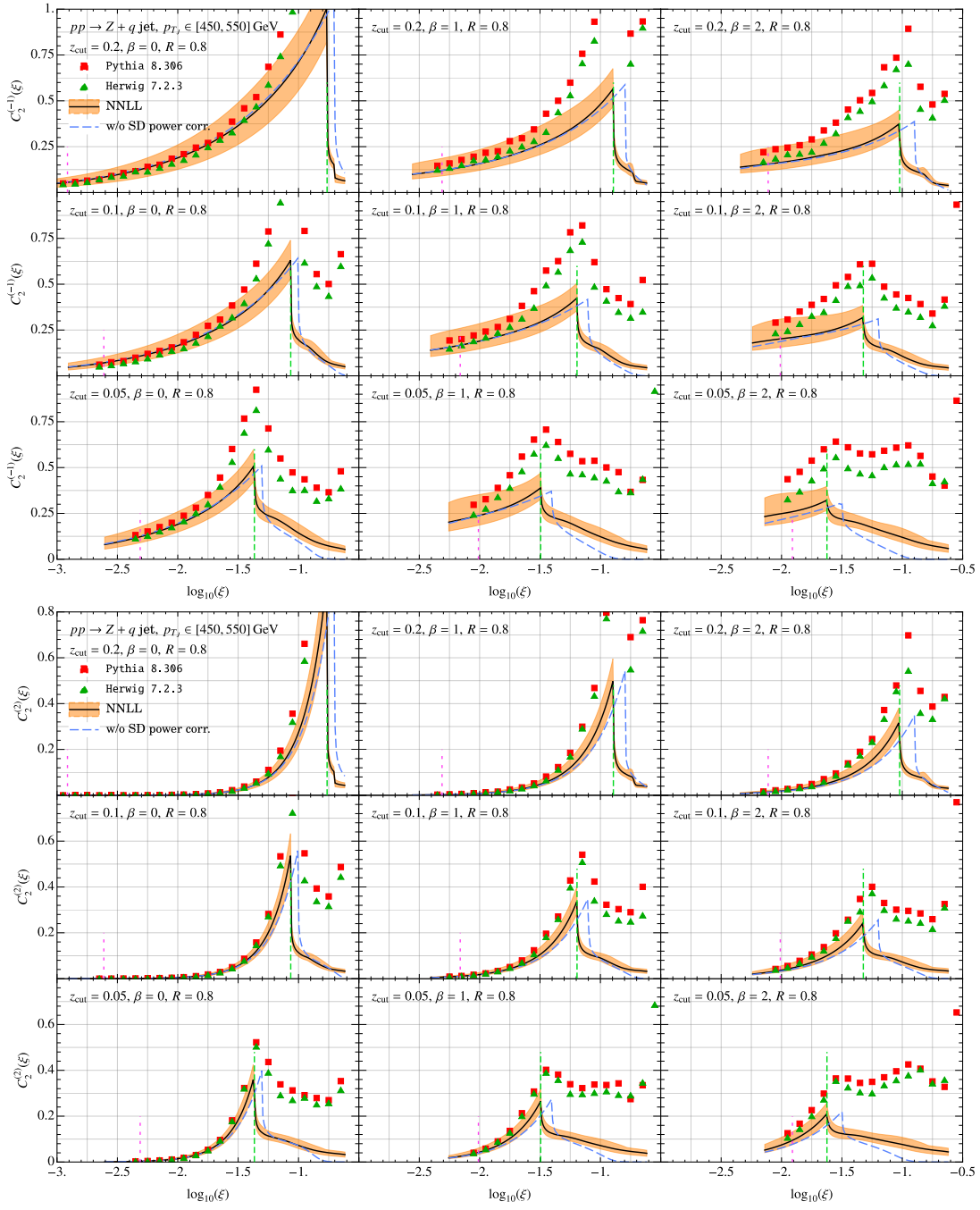
Figure 24. Comparison of NNLL prediction of $C_{2\kappa}^{(-1)}$ and $C_{2\kappa}^{(2)}$ against parton level simulations of quark jets in `Pythia 8.3` and `Herwig 7.2` in pp collisions. The additional contribution beyond the cusp region arises from ungroomed initial state radiation.
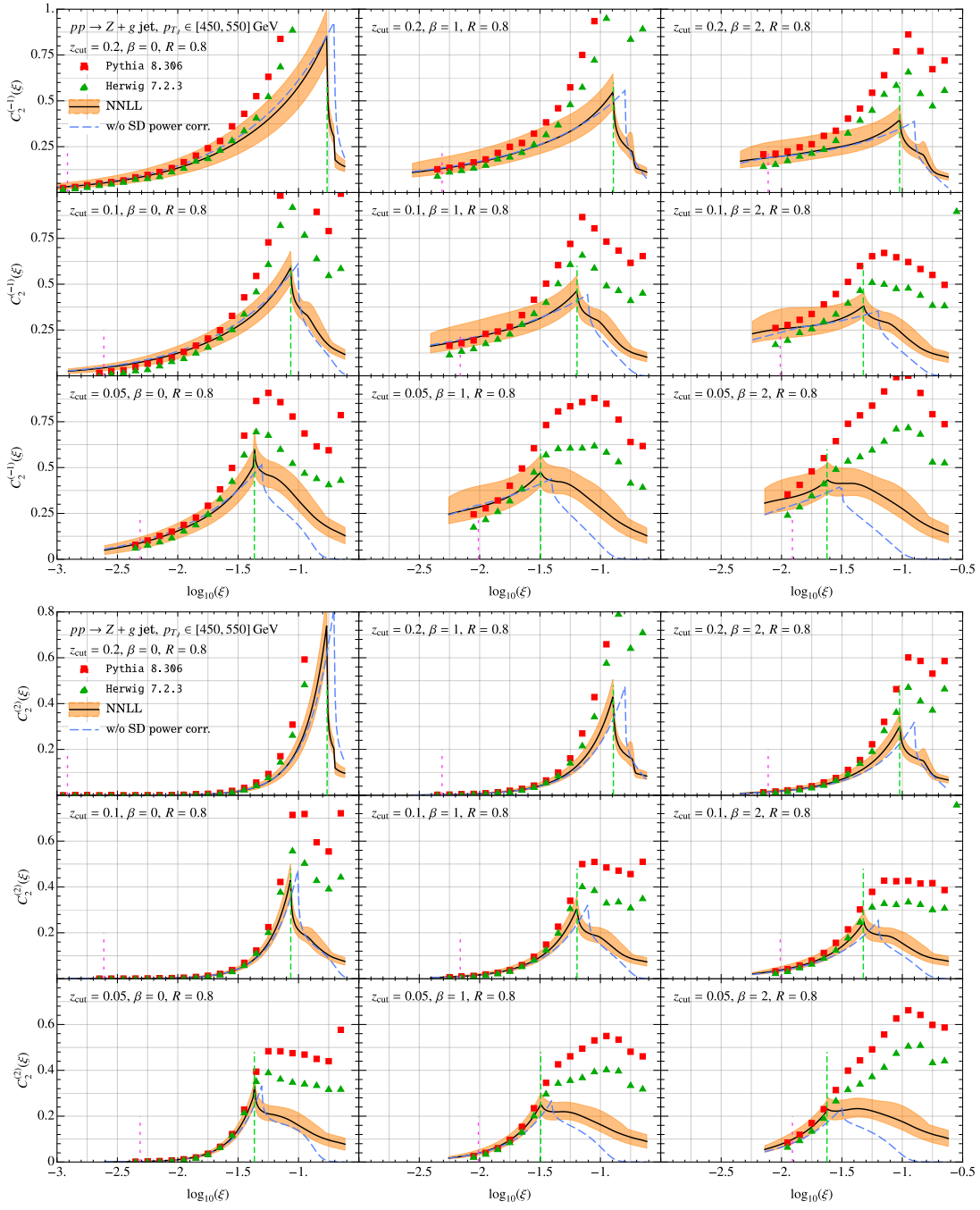
Figure 25. Comparison of NNLL prediction of $C_{2\kappa}^{(-1)}$ and $C_{2\kappa}^{(2)}$ against parton level simulations of gluon jets in `Pythia 8.3` and `Herwig 7.2` in pp collisions. The additional contribution beyond the cusp region arises from ungroomed initial state radiation.

parton level extractions from `Pythia 8.3` and `Herwig 7.2` simulations. The parton shower extractions of these weights, though less precise, agreed well within the uncertainty bands for $e^+e^- \to q\bar{q}$ and $e^+e^- \to gg$ processes within the SDOE region. We saw some disagreement near the cusp for $C_{2\kappa}^{(-1)}$ moment for pp collisions due to inevitable contribution from the initial state radiation in simulations. On the other hand, the moments that are relevant for ISR and the underlying event were found to be in better agreement in the SDOE region for simulations of jets in pp collisions.

In comparing the results of this work with the previous computation in ref. [83] we found that the results in the soft drop resummation region did not differ significantly. However, by including the ungroomed region, we ensure a more comprehensive treatment of the problem. This matching also described the significant shift in the soft drop cusp arising at NNLL accuracy, that cannot be systematically accounted for otherwise. Additionally, in the region soft drop resummation region, the fact that the new calculation falls within tthe uncertainty of the previous results can be seen as a consistency check, giving us increased confidence in the validity of our theoretical framework. It is also reassuring to see that the new calculation, though more intricate, does not introduce any unexpected large power corrections in the soft drop resummation region that were previously neglected. Finally, the result of the perturbative weights extended into the ungroomed region provides a starting point for equivalently extending the power corrections beyond the soft drop cusp.

In summary, we believe that this paper provides motivation for carrying out analyses with unfolded data from colliders. With the prospects of high quality data to be delivered from high-luminosity phase of the LHC, it will be very exciting to use the approach presented in this paper to further our understanding of hadronization effects as well as carry out precision measurements using groomed observables.

Acknowledgments

A Anomalous dimensions

In this appendix we consolidate the anomalous dimensions up to $\mathcal{O}(\alpha_s^2)$ for NNLL resummation of the various factorization functions appearing in our analysis as well as results of certain functions in Laplace space. We refer the reader to appendix A of ref. [83] for a details of the notation for anomalous dimension and RG evolution kernels.

The cusp anomalous dimensions are given by

$$\Gamma_{N_{\text{incl}}^{\kappa}}[\alpha_s] = -2\,C_\kappa \Gamma^{\text{cusp}}[\alpha_s]\,, \tag{A.1}$$
$$\Gamma_{J^\kappa}[\alpha_s] = +2\,C_\kappa \Gamma^{\text{cusp}}[\alpha_s]\,,$$
$$\Gamma_{\mathcal{C}^\kappa}[\alpha_s] = +2\,C_\kappa \Gamma^{\text{cusp}}[\alpha_s]\,,$$
$$\Gamma_{S_{c_m}^\kappa}[\alpha_s] = -2C_\kappa \Gamma^{\text{cusp}}[\alpha_s]\,,$$
$$\Gamma_{S_G^\kappa}[\alpha_s] = +2C_\kappa \Gamma^{\text{cusp}}[\alpha_s]\,,$$
$$\Gamma_{S_{cg}^\kappa}[\alpha_s] = -2C_\kappa \Gamma^{\text{cusp}}[\alpha_s]\,,$$
$$\Gamma_{S_c^\kappa}[\alpha_s] = -2C_\kappa \Gamma^{\text{cusp}}[\alpha_s]\,,$$

where with the convention

$$\Gamma^{\text{cusp}}[\alpha_s] = \sum_{n=0}^{\infty} \Gamma_n^{\text{cusp}} \left(\frac{\alpha_s}{4\pi}\right)^{n+1}\,, \tag{A.2}$$

up to NNLL we have [104–106]

$$\Gamma_0^{\text{cusp}} = 4\,, \tag{A.3}$$
$$\Gamma_1^{\text{cusp}} = 8\left[\left(\frac{67}{18} - \frac{\pi^2}{6}\right)C_A - \frac{5}{9}n_f\right]$$
$$\Gamma_2^{\text{cusp}} = 16\left[\left(\frac{245}{24} - \frac{67}{54} + \frac{11\pi^4}{180} + \frac{11}{6}\right)C_A^2 + \left(-\frac{209}{108} + \frac{5\pi^2}{27} - \frac{7}{3}\zeta_3\right)C_A n_f \right.$$
$$\left. + \left(\frac{-55}{27} + 2\zeta_3\right)C_F n_f - \frac{1}{27}n_f^2\right].$$

Next, we state the non-cusp anomalous dimensions following the same series expansion as in eq. (A.2). The non-cusp anomalous dimensions of the normalization factor N_{incl}^{κ} for quark and gluon jets are given by

$$\gamma_0^{N^q} = -6C_F\,, \qquad \gamma_0^{N^g} = -2\beta_0\,, \tag{A.4}$$

$$\gamma_1^{N^q} = \left(-3 + 4\pi^2 - 48\zeta_3\right)C_F^2 + \left(-\frac{961}{27} - \frac{11\pi^2}{3} + 52\zeta_3\right)C_F C_A + \left(\frac{260}{27} + \frac{4\pi^2}{3}\right)C_F n_f T_F\,,$$
$$\gamma_1^{N^g} = \left(-\frac{118}{9} + 4\zeta_3\right)C_A^2 + \left(-\frac{38}{9} + \frac{\pi^2}{3}\right)C_A \beta_0 - 4\beta_1\,. \tag{A.5}$$

For the jet function we have

$$\gamma_0^{J_q} = 6C_F\,, \qquad \gamma_0^{J_g} = 2\beta_0\,, \tag{A.6}$$

$$\gamma_1^{J_q} = C_F\left[C_F\left(3 - 4\pi^2 + 48\zeta_3\right) + C_A\left(\frac{1769}{27} + \frac{22\pi^2}{9} - 80\zeta_3\right) + T_R n_f\left(-\frac{484}{27} - \frac{8\pi^2}{9}\right)\right],$$

$$\gamma_1^{J_g} = C_A^2\left(\frac{2192}{27} - \frac{22\pi^2}{9} - 32\zeta_3\right) + C_A T_R n_f\left(-\frac{736}{27} + \frac{8\pi^2}{9}\right) - 8C_F T_R n_f\,. \tag{A.7}$$

The one-loop non-cusp anomalous dimension of all the soft functions are zero (with the exception of the boundary soft drop non-cusp anomalous dimension for $\beta = 0$ in eq. (6.17)). For $S_{c_m}^\kappa$ (and S_{plain}^κ), we have

$$\gamma_1^{S_{c_m}^\kappa} = C_\kappa\left(C_A\left(-\frac{808}{27} + \frac{11\pi^2}{9} + 28\zeta_3\right) + n_f T_F\left(\frac{224}{27} - \frac{4\pi^2}{9}\right)\right). \tag{A.8}$$

At two-loops a numerical approximation of the global soft anomalous dimension reads [55, 91]:

$$\gamma_1^{S_G^\kappa}(\beta) = \frac{C_\kappa}{1+\beta}\left(\gamma_{C_F}^{S_G^\kappa}(\beta) + n_f \gamma_{T_F}^{S_G^\kappa}(\beta) + \gamma_{C_A}^{S_G^\kappa}(\beta)\right), \tag{A.9}$$

where

$$\gamma_{C_F}^{S_G^\kappa}(\beta) = C_F\left(0.00563338\beta^3 - 0.621462\beta^2 - 1.11337\beta + 16.9974\right), \tag{A.10}$$

$$\gamma_{T_F}^{S_G^\kappa}(\beta) = T_F\left(-0.26041\beta^3 + 2.01765\beta^2 + 3.48117\beta - 10.9341\right),$$

$$\gamma_{C_A}^{S_G^\kappa}(\beta) = C_A\left(+0.640703\beta^3 + 3.37308\beta^2 + 3.68876\beta - 20.4351\right).$$

The anomalous dimension of the hard-collinear function $\mathcal{C}^\kappa(\xi, r_g, Q, \mu)$ is simply the negative of that of the normalization factor N_{incl}^κ. Likewise the anomalous dimension of $S_{c_g}^\kappa$ is negative of that of the global soft function:

$$\gamma_{\mathcal{C}^\kappa}[\alpha_s] = -\gamma_{N^\kappa}[\alpha_s]\,, \tag{A.11}$$

$$\gamma_{S_{c_g}^\kappa}[\alpha_s] = -\gamma_{S_G^\kappa}[\alpha_s]\,.$$

Finally, the non-cusp anomalous dimension of the collinear soft function S_c^κ can be obtained using RG consistency of the max-R_g cross section:

$$\gamma_1^{S_c^\kappa}(\beta) = -\gamma_1^{N^\kappa} - \gamma_1^{J_\kappa} - \gamma_1^{S_G^\kappa}(\beta)\,. \tag{A.12}$$

B Profile functions

Here we discuss the profile functions that incorporate the appropriate canonical scales for various factorization functions as well as enable us to estimate perturbative uncertainty through their varaitions. Here we simply summarize the final formulae of original implementation discussed in great detail in ref. [83] in the soft drop resummation region, which was further extended into the plain jet mass region in ref. [55].

Firstly, the hard scale and global-soft scales are defined as

$$\mu_N \equiv e_N Q \,, \qquad \mu_{gs} \equiv e_N Q_{\text{cut}} \,, \qquad e_N \in [0.5, 2] \,, \tag{B.1}$$

where the parameter e_N is varied in the range shown. In the fixed-order cross section we use the same μ_N scale. We vary the two scales with the same parameters so as to be consistent with matching at the soft drop cusp by ensuring that $\mu_{gs}/\mu_N = \xi_0$.

B.1 Plain jet mass profiles

Next, we summarize the profile scales and their variations associated with the plain jet mass cross section as described in ref. [55]:

$$\tilde{\mu}_s^{\text{plain}}(\xi; \lambda) \equiv \mu_N \left[f_{\text{vary}}^{\text{plain}}(\xi) \right]^\lambda f_{\text{run}}^{\text{plain}}(\xi) \,, \tag{B.2}$$

$$\mu_s^{\text{plain}}(\xi; \lambda) \equiv f_{\text{freeze}} \left[\tilde{\mu}_s^{\text{plain}}(\xi; \lambda) \right] \,,$$

$$\mu_J^{\text{plain}}(\xi; \lambda, \gamma) \equiv \mu_N^{\frac{1}{2}+\gamma} \left(\mu_s^{\text{plain}}(\xi; \lambda) \right)^{\frac{1}{2}-\gamma} \,.$$

The jet and soft scales being proportional to μ_N inherit the e_N norm-variation in eq. (B.1). The interpolation of the canonical ungroomed soft scales between various regions is governed by $f_{\text{run}}^{\text{plain}}(\xi)$ given by

$$f_{\text{run}}^{\text{plain}}(\xi) \equiv \begin{cases} x_0 \left(1 + \frac{\xi^2}{4x_0^2} \right) & \xi \leq 2x_0 \\ \xi & 2x_0 < \xi \leq x_1 \\ \xi + \frac{(2-x_2-x_3)(\xi-x_1)^2}{2(x_2-x_1)(x_3-x_1)} & x_1 < \xi \leq x_2 \\ 1 - \frac{(2-x_1-x_2)(\xi-x_3)^2}{2(x_3-x_1)(x_3-x_2)} & x_2 < \xi \leq x_3 \\ 1 & x_3 < \xi \leq 1 \end{cases} \,. \tag{B.3}$$

The regions $\xi < x_0$, $2x_0 < \xi < x_1$ and $x_3 < \xi < 1$ respectively correspond to the ungroomed-nonperturbative, ungroomed-resummation and fixed order region. x_0 is determined by the point where the soft scale freezes to a nonperturbative scale,

$$x_0 = \frac{n_0}{(\mu_N/1\text{GeV})} \,, \tag{B.4}$$

where we take the default value of $n_0 = 1$. Additionally, varying this parameter tests sensitivity of the cross section to nonperturbative effects:

$$\text{Vary } \alpha_s \text{ freezing scale:} \qquad n_0 \in [0.75, 1.25] \,. \tag{B.5}$$

The other three parameters take different values depending on the transition point ξ_0. Firstly, x_3 is given by

$$\begin{aligned} \xi_0 < 0.2 & \quad : x_3 = 0.2 \,, \\ 0.2 \leq \xi_0 < 0.25 & \quad : x_3 = \frac{0.25 + \xi_0}{2} \,, \\ 0.25 \leq \xi_0 & \quad : x_3 = \min\{\xi_0 + 0.1, 1\} \,, \end{aligned} \tag{B.6}$$

and x_1 and x_2 are given by

$$x_1 = \Theta(x_3 - 1.15\xi_0)1.15\xi_0 + \Theta(1.15\xi_0 - x_3)\xi_0, \qquad x_2 = \frac{x_1 + x_3}{2}. \tag{B.7}$$

Having defined the canonical soft scale $\tilde{\mu}_s(\xi)$ we implement its variation in the plain jet mass resummation region alone, different than the overall normalization probed by e_N, using the trumpet function

$$f_{\text{vary}}^{\text{plain}}(\xi) \equiv \begin{cases} 1 & 0 < \xi \leq \xi_0 \\ \zeta(\xi, \xi_0, x_{\text{mid}}; 1, 2), & \xi_0 \leq \xi < x_{\text{mid}} \\ \zeta(\xi, x_{\text{mid}}, x_3; 2, 1), & x_{\text{mid}} \leq \xi \leq x_3 \\ 1 & x_3 < \xi \leq 1 \end{cases}, \tag{B.8}$$

where

$$x_{\text{mid}} \equiv \frac{\xi_0 + x_3}{2}, \tag{B.9}$$

and

$$\zeta(\xi, x_{\text{start}}, x_{\text{end}}; a_1, a_2) \equiv \begin{cases} a_1 & \xi \leq x_{\text{start}} \\ a_1 + \frac{2(a_2 - a_1)(\xi - x_{\text{start}})^2}{(x_{\text{end}} - x_{\text{start}})^2}, & x_{\text{start}} \leq \xi < \frac{x_{\text{start}} + x_{\text{end}}}{2} \\ a_2 - \frac{2(a_2 - a_1)(x_{\text{end}} - \xi)^2}{(x_{\text{end}} - x_{\text{start}})^2}, & \frac{x_{\text{start}} + x_{\text{end}}}{2} \leq \xi \leq x_{\text{end}} \\ a_2 & x_{\text{end}} < \xi \end{cases}. \tag{B.10}$$

This variation is controlled via the parameter λ:

Trumpet variation in plain jet mass region: $\qquad \lambda \in [-1, 0.3]. \tag{B.11}$

Finally we avoid the scale varying below the nonperturbative scale n_0 by re-freezing via the function

$$f_{\text{freeze}}[\mu] \equiv \begin{cases} \mu, & \mu \geq 2n_0 \\ n_0\left(1 + \frac{\mu^2}{4n_0^2}\right), & \mu < 2n_0 \end{cases}. \tag{B.12}$$

The jet scale in eq. (B.2) is derived from the ungroomed soft scale using the canonical see-saw relation with $\gamma = 0$. Breaking this canonical relation defines another variation:

Break jet-hard-soft see-saw canonical relation: $\qquad \gamma \in [-0.1, 0.1], \tag{B.13}$

We have written a "plain" subscript on the jet scale as we use a sightly different prescription for freezing in the nonperturbative region for the jet scale in the soft drop resummed cross section below.

B.2 Soft drop profiles

We first summarize min-R_g profiles:

$$\tilde{\mu}_{cs_g}(r_g; \alpha) \equiv \left(f_{\text{vary}}^{\text{sd res.}}(r_g^{1+\beta})\right)^{\alpha} \mu_{gs} f_{\text{run}}^{\text{sd res.}}(r_g^{1+\beta}), \tag{B.14}$$

$$\mu_{cs_g}(r_g; \alpha) \equiv f_{\text{freeze}}\left[\tilde{\mu}_{cs_g}(r_g; \alpha)\right],$$

$$\mu_{\mathcal{C}}(r_g; \alpha, \gamma) \equiv \mu_N\left(\frac{\mu_{cs_g}(r_g; \alpha)}{\mu_{gs}}\right)^{\frac{1-\gamma}{1+\gamma}\frac{1}{1+\beta}},$$

Here the soft scale depends on the groomed jet radius r_g instead of the jet mass, and the interpolating function is defined to be

$$f_{\text{run}}^{\text{sd res.}}(r_g) \equiv \begin{cases} y_0\left(1 + \frac{r_g^2}{4y_0^2}\right) & r_g \leq 2y_0 \\ r_g & 2y_0 < r_g \leq 1 \end{cases}. \tag{B.15}$$

Here, the parameter governing the transition into the (soft drop) nonperturbative region is given by

$$y_0 \equiv \frac{n_0}{(\mu_{gs}/1\,\text{GeV})} > \frac{\Lambda_{\text{QCD}}}{Q_{\text{cut}}}. \tag{B.16}$$

As above, the trumpet variation that vanishes at the end points is governed by

$$f_{\text{vary}}^{\text{sd res.}}(r_g) = \begin{cases} 2(1 - r_g^2), & r_g < 0.5 \\ 1 + 2(1 - r_g)^2, & 0.5 \leq r_g \leq 1 \end{cases}. \tag{B.17}$$

With $\alpha = 0$ in eq. (B.14) the new variation we have is given by

Trumpet variation in the soft drop resummation region: $\quad \alpha \in [-1, 1]$. $\quad$ (B.18)

As in the case of jet scale above, the hard-collinear scale $\mu_{\mathcal{C}}$ is derived from the μ_{cs_g} scale as shown in eq. (B.14) using the canonical relation for $\gamma = 0$. To ensure that the jet scale in the max-R_g and int-R_g region merges with the hard-collinear scale for $\gamma \neq 0$, we are required to use the same parameter for the two and vary them together as in eq. (B.13).

Next, we summarize the implementation of profiles for max-R_g cross section in soft drop resummation region:

$$\tilde{\mu}_s^{\text{sd res.}}(\xi) \equiv \mu_{gs}\left[f_{\text{run}}^{\text{sd res.}}\left(\left(\frac{\xi}{\xi_0}\right)^{\frac{1+\beta}{2+\beta}}\right)\right]^{\frac{2+\beta}{1+\beta}}, \tag{B.19}$$

$$\tilde{\mu}_{cs}(\xi; \alpha, \rho) \equiv \left[f_{\text{vary}}^{\text{sd res.}}\left(\left(\frac{\xi}{\xi_0}\right)^{\frac{1+\beta}{2+\beta}}\right)\right]^{\alpha}\left(\tilde{\mu}_s^{\text{sd res.}}(\xi)\right)^{\frac{1+\beta+\rho}{2+\beta}}(\mu_{gs})^{\frac{1-\rho}{2+\beta}},$$

$$\mu_{cs}(\xi; \alpha, \rho) \equiv f_{\text{freeze}}\left[\tilde{\mu}_{cs}(\xi; \alpha, \rho)\right],$$

$$\mu_J(\xi; \alpha, \gamma, \rho) \equiv \left[\mu_{\mathcal{C}}(r_g; \alpha, \gamma)\right]^{\frac{1}{2}+\gamma}\left[\mu_{cs}(\xi; \alpha, \rho)\left(\frac{\mu_{cs}(\xi; \alpha, \rho)}{\mu_{gs}}\right)^{\frac{1}{1+\beta}}\right]^{\frac{1}{2}-\gamma}.$$

In addition to the functions and variation parameters discussed already above, we have a new canonical relation between the ungroomed soft scale, collinear-soft scale and global-soft scale. This relation allows us to define the c-soft scale in terms of the other two, whereas the auxiliary "ungroomed-soft scale" $\tilde{\mu}_s^{\text{sd res.}}(\xi)$ itself is derived using the μ_{cs_g} scale. Thus, the variation of ρ with default value $\rho = 0$ now probes the effect of breaking this canonical relation:

Break μ_{gs}, μ_{cs} and plain soft see-saw canonical relation: $\quad \rho \in [-0.1, 0.1]$. $\quad$ (B.20)

Lastly, in the intermediate region, we use the $\mu_J, \mu_{gs}, \mu_{cs_g}$ and the hard scale above, and use the soft drop canonical see-saw relation to define the μ_{cs_m} scale:

$$\mu_{cs_m}(\xi, r_g; \alpha, \rho) \equiv \mu_{cs}(\xi; \alpha, \rho) \left(\frac{\mu_{cs}(\xi; \alpha, \rho)}{\mu_{gs}} \right)^{\frac{1}{1+\beta}} \left(\frac{\mu_{cs_g}(r_g; \alpha)}{\mu_{gs}} \right)^{\frac{-(1-\rho)}{1+\rho+\beta}} . \tag{B.21}$$

This concludes the summary of profile scales implementation and their variations.

C Weight functions

Here we describe how the weight functions constructed in ref. [83] are extended into the plain jet mass resummation region. We first list down the relevant canonical profile scales

$$\mu_J^{\text{can.}} = Q\sqrt{\xi}, \qquad \mu_{gs}^{\text{can.}} = Q_{\text{cut}}, \qquad \mu_{cs_m}^{\text{can.}} = Q\xi/r_g, \qquad \mu_{cs_g}^{\text{can.}} = Q_{\text{cut}} r_g^{1+\beta}, \tag{C.1}$$

Using these scales and the size of power corrections in the intermediate-R_g regime in eq. (4.36) we can define parameters that control transition from intermediate to min and max-R_g regimes. For transition from intermediate to min-R_g regime, we define

$$\lambda_{\text{min}} \equiv \frac{\mu_{cs_m}}{\mu_J} = \frac{\sqrt{\xi}}{r_g} . \tag{C.2}$$

In transitioning to the max-R_g regime, we define two parameters for cases $\xi < \xi_0'$ and $\xi > \xi_0'$:

$$\lambda_{\text{max}}^{\text{sd res.}} \equiv \frac{\mu_{cs_g}}{\mu_{cs_m}} = \frac{\xi_0}{\xi} r_g^{2+\beta}, \qquad\qquad \lambda_{\text{max}}^{\text{plain}} \equiv \frac{\mu_{cs_g}}{\mu_{gs}} = r_g^{1+\beta} . \tag{C.3}$$

Next, to determine whether or not the intermediate regime is required, we calculate the angle $r_{g,t}$ for which $\lambda_{\text{min}} = \lambda_{\text{max}}$:

$$r_{g,t}^{\text{sd res.}}(\xi) \equiv \left[\frac{\xi}{\xi_0} \sqrt{\xi} \right]^{\frac{1}{3+\beta}}, \qquad r_{g,t}^{\text{plain}}(\xi) \equiv \left(\sqrt{\xi} \right)^{\frac{1}{2+\beta}}, \tag{C.4}$$

which can be combined as

$$r_{g,t}(\xi) \equiv \left(\frac{\xi}{\xi_0} \right)^{a_{\text{sd}}(\log_{10}\xi)} (\sqrt{\xi})^{a_{\text{plain}}(\log_{10}\xi)}, \tag{C.5}$$

where the exponents are modified as a function of ξ, and are given by

$$a_{\text{sd}}(\log_{10}\xi) \equiv a\left(\log_{10}(\xi); \frac{1}{3+\beta}, 0 \right), \tag{C.6}$$

$$a_{\text{plain}}(\log_{10}\xi) \equiv a\left(\log_{10}(\xi); \frac{1}{3+\beta}, \frac{1}{2+\beta} \right),$$

where $a(\log_{10}(\xi); x, y)$ is a function that smoothly transitions from the value x to y as ξ is increased past $\xi = \xi_0'$, and is defined as

$$a(\log_{10}(\xi); x, y) \equiv \zeta\left(\log_{10}\xi, \left[\log_{10}(\xi_0') - \delta\xi \right], \left[\log_{10}(\xi_0') + \delta\xi \right]; x, y \right), \tag{C.7}$$

where the function $\zeta(\xi, x_{\text{start}}, x_{\text{end}}; a_1, a_2)$ was defined above in eq. (B.10) and we set $\delta\xi = 0.75$.

We will take $\lambda = 1/3$ as the reference power correction to determine the validity of the intermediate regime; i.e. if $\lambda_{\max}, \lambda_{\min} < \lambda$ then we implement resummation in the intermediate region defined by

$$r_{g,\text{PC}}^{\min}(\xi, \lambda) \leq r_g \leq r_{g,\text{PC}}^{\max}(\xi, \lambda), \tag{C.8}$$

where

$$r_{g,\text{PC}}^{\min}(\xi, \lambda) \equiv \frac{\sqrt{\xi}}{\lambda}. \tag{C.9}$$

Now for the max-R_g regime, we have two cases:

$$r_{g,\text{PC}}^{\text{sd res.}}(\xi, \lambda) \equiv \left(\frac{\xi}{\xi_0}\lambda\right)^{\frac{1}{2+\beta}}, \qquad r_{g,\text{PC}}^{\text{plain}}(\xi, \lambda) \equiv \lambda^{\frac{1}{1+\beta}}, \tag{C.10}$$

the following combination of which defines $r_{g,\text{PC}}^{\max}$ in eq. (C.8):

$$r_{g,\text{PC}}^{\max}(\xi, \lambda) \equiv \left(\frac{\xi}{\xi_0}\right)^{a_{\text{sd}}^{\text{PC}}(\log_{10}\xi)} \lambda^{a_{\text{plain}}^{\text{PC}}(\log_{10}\xi)}, \tag{C.11}$$

where

$$
\begin{aligned}
a_{\text{sd}}^{\text{PC}}(\log_{10}\xi) &\equiv a\left(\log_{10}\xi; \frac{1}{2+\beta}, 0\right), \\
a_{\text{plain}}^{\text{PC}}(\log_{10}\xi) &\equiv a\left(\log_{10}\xi; \frac{1}{2+\beta}, \frac{1}{1+\beta}\right).
\end{aligned}
\tag{C.12}
$$

We finally introduce a transition function $X(r_g, r_{g,t})$ for a given value of ξ:

$$X(r_g, r_{g,t}) = \frac{1}{2}\left(1 + \tanh\left(x_t \frac{r_g - r_{g,t}}{r_g^{\max}(\xi) - r_g^{\min}(\xi)}\right)\right), \qquad x_t = 20, \tag{C.13}$$

and design the weight functions for the three EFT regimes as

2-EFT: $\quad w_{\max} = X(r_g, r_{g,t}(\xi)), \qquad w_{\text{int}} = 0,$ (C.14)

3-EFT: $\quad w_{\max} = X(r_g, r_{g,\text{PC}}^{\max}(\xi, \lambda)), \quad w_{\text{int}} = \left[1 - X(r_g, r_{g,\text{PC}}^{\max}(\xi, \lambda))\right] X(r_g, r_{g,\text{PC}}^{\min}(\xi, \lambda)),$

In either of these cases $w_{\min} = 1 - w_{\text{int}} - w_{\max}$. With the above construction, these weight functions turn on in their respective regime.

References

[1] A.J. Larkoski, I. Moult and B. Nachman, *Jet Substructure at the Large Hadron Collider: A Review of Recent Advances in Theory and Machine Learning*, *Phys. Rept.* **841** (2020) 1 [`arXiv:1709.04464`] [INSPIRE].

[2] R. Kogler et al., *Jet Substructure at the Large Hadron Collider: Experimental Review*, *Rev. Mod. Phys.* **91** (2019) 045003 [`arXiv:1803.06991`] [INSPIRE].

[3] C. Lee and G.F. Sterman, *Universality of nonperturbative effects in event shapes*, *eConf* **C0601121** (2006) A001 [`hep-ph/0603066`] [INSPIRE].

[4] G.P. Korchemsky and G.F. Sterman, *Nonperturbative corrections in resummed cross-sections*, *Nucl. Phys. B* **437** (1995) 415 [`hep-ph/9411211`] [INSPIRE].

[5] G.P. Korchemsky, G. Oderda and G.F. Sterman, *Power corrections and nonlocal operators*, *AIP Conf. Proc.* **407** (1997) 988 [`hep-ph/9708346`] [INSPIRE].

[6] G.P. Korchemsky and G.F. Sterman, *Power corrections to event shapes and factorization*, *Nucl. Phys. B* **555** (1999) 335 [`hep-ph/9902341`] [INSPIRE].

[7] A.V. Belitsky, G.P. Korchemsky and G.F. Sterman, *Energy flow in QCD and event shape functions*, *Phys. Lett. B* **515** (2001) 297 [`hep-ph/0106308`] [INSPIRE].

[8] M. Dasgupta, L. Magnea and G.P. Salam, *Non-perturbative QCD effects in jets at hadron colliders*, *JHEP* **02** (2008) 055 [`arXiv:0712.3014`] [INSPIRE].

[9] I.W. Stewart, F.J. Tackmann and W.J. Waalewijn, *Dissecting Soft Radiation with Factorization*, *Phys. Rev. Lett.* **114** (2015) 092001 [`arXiv:1405.6722`] [INSPIRE].

[10] S.D. Ellis, C.K. Vermilion and J.R. Walsh, *Recombination Algorithms and Jet Substructure: Pruning as a Tool for Heavy Particle Searches*, *Phys. Rev. D* **81** (2010) 094023 [`arXiv:0912.0033`] [INSPIRE].

[11] M. Cacciari, G.P. Salam and G. Soyez, *SoftKiller, a particle-level pileup removal method*, *Eur. Phys. J. C* **75** (2015) 59 [`arXiv:1407.0408`] [INSPIRE].

[12] D. Krohn, J. Thaler and L.-T. Wang, *Jet Trimming*, *JHEP* **02** (2010) 084 [`arXiv:0912.1342`] [INSPIRE].

[13] M. Dasgupta, A. Fregoso, S. Marzani and G.P. Salam, *Towards an understanding of jet substructure*, *JHEP* **09** (2013) 029 [`arXiv:1307.0007`] [INSPIRE].

[14] A.J. Larkoski, S. Marzani, G. Soyez and J. Thaler, *Soft Drop*, *JHEP* **05** (2014) 146 [`arXiv:1402.2657`] [INSPIRE].

[15] J.M. Butterworth, A.R. Davison, M. Rubin and G.P. Salam, *Jet substructure as a new Higgs search channel at the LHC*, *Phys. Rev. Lett.* **100** (2008) 242001 [`arXiv:0802.2470`] [INSPIRE].

[16] C. Frye, A.J. Larkoski, J. Thaler and K. Zhou, *Casimir Meets Poisson: Improved Quark/Gluon Discrimination with Counting Observables*, *JHEP* **09** (2017) 083 [`arXiv:1704.06266`] [INSPIRE].

[17] F.A. Dreyer, L. Necib, G. Soyez and J. Thaler, *Recursive Soft Drop*, *JHEP* **06** (2018) 093 [`arXiv:1804.03657`] [INSPIRE].

[18] K. Lee, B. Meçaj and I. Moult, *Conformal Colliders Meet the LHC*, [`arXiv:2205.03414`] [INSPIRE].

[19] P.T. Komiske, I. Moult, J. Thaler and H.X. Zhu, *Analyzing N-Point Energy Correlators inside Jets with CMS Open Data*, *Phys. Rev. Lett.* **130** (2023) 051901 [arXiv:2201.07800] [INSPIRE].

[20] J. Holguin, I. Moult, A. Pathak and M. Procura, *New paradigm for precision top physics: Weighing the top with energy correlators*, *Phys. Rev. D* **107** (2023) 114002 [arXiv:2201.08393] [INSPIRE].

[21] H. Chen, I. Moult, J. Thaler and H.X. Zhu, *Non-Gaussianities in collider energy flux*, *JHEP* **07** (2022) 146 [arXiv:2205.02857] [INSPIRE].

[22] H. Chen, I. Moult, J. Sandor and H.X. Zhu, *Celestial blocks and transverse spin in the three-point energy correlator*, *JHEP* **09** (2022) 199 [arXiv:2202.04085] [INSPIRE].

[23] C. Andres et al., *Resolving the Scales of the Quark-Gluon Plasma with Energy Correlators*, *Phys. Rev. Lett.* **130** (2023) 262301 [arXiv:2209.11236] [INSPIRE].

[24] C. Frye, A.J. Larkoski, M.D. Schwartz and K. Yan, *Factorization for groomed jet substructure beyond the next-to-leading logarithm*, *JHEP* **07** (2016) 064 [arXiv:1603.09338] [INSPIRE].

[25] C. Frye, A.J. Larkoski, M.D. Schwartz and K. Yan, *Precision physics with pile-up insensitive observables*, arXiv:1603.06375 [INSPIRE].

[26] A.H. Hoang, S. Mantry, A. Pathak and I.W. Stewart, *Extracting a Short Distance Top Mass with Light Grooming*, *Phys. Rev. D* **100** (2019) 074021 [arXiv:1708.02586] [INSPIRE].

[27] P. Cal, K. Lee, F. Ringer and W.J. Waalewijn, *The soft drop momentum sharing fraction zg beyond leading-logarithmic accuracy*, *Phys. Lett. B* **833** (2022) 137390 [arXiv:2106.04589] [INSPIRE].

[28] A. Larkoski et al., *Exposing the QCD Splitting Function with CMS Open Data*, *Phys. Rev. Lett.* **119** (2017) 132003 [arXiv:1704.05066] [INSPIRE].

[29] D. Gutierrez-Reyes et al., *Probing Transverse-Momentum Distributions With Groomed Jets*, *JHEP* **08** (2019) 161 [arXiv:1907.05896] [INSPIRE].

[30] Y. Makris and V. Vaidya, *Transverse Momentum Spectra at Threshold for Groomed Heavy Quark Jets*, *JHEP* **10** (2018) 019 [arXiv:1807.09805] [INSPIRE].

[31] Y.-T. Chien and I.W. Stewart, *Collinear Drop*, *JHEP* **06** (2020) 064 [arXiv:1907.11107] [INSPIRE].

[32] P. Cal, K. Lee, F. Ringer and W.J. Waalewijn, *Jet energy drop*, *JHEP* **11** (2020) 012 [arXiv:2007.12187] [INSPIRE].

[33] I.W. Stewart and X. Yao, *Pure quark and gluon observables in collinear drop*, *JHEP* **09** (2022) 120 [arXiv:2203.14980] [INSPIRE].

[34] R. Kunnawalkam Elayavalli and K.C. Zapp, *Medium response in JEWEL and its impact on jet shape observables in heavy ion collisions*, *JHEP* **07** (2017) 141 [arXiv:1707.01539] [INSPIRE].

[35] H.A. Andrews et al., *Novel tools and observables for jet physics in heavy-ion collisions*, *J. Phys. G* **47** (2020) 065102 [arXiv:1808.03689] [INSPIRE].

[36] Y. Mehtar-Tani and K. Tywoniuk, *Groomed jets in heavy-ion collisions: sensitivity to medium-induced bremsstrahlung*, *JHEP* **04** (2017) 125 [arXiv:1610.08930] [INSPIRE].

[37] J. Casalderrey-Solana, G. Milhano, D. Pablos and K. Rajagopal, *Modification of Jet Substructure in Heavy Ion Collisions as a Probe of the Resolution Length of Quark-Gluon Plasma*, *JHEP* **01** (2020) 044 [arXiv:1907.11248] [INSPIRE].

[38] J. Brewer, Q. Brodsky and K. Rajagopal, *Disentangling jet modification in jet simulations and in Z+jet data*, *JHEP* **02** (2022) 175 [arXiv:2110.13159] [INSPIRE].

[39] ALICE collaboration, *First measurement of jet mass in Pb-Pb and p-Pb collisions at the LHC*, *Phys. Lett. B* **776** (2018) 249 [arXiv:1702.00804] [INSPIRE].

[40] ATLAS collaboration, *Jet mass and substructure of inclusive jets in $\sqrt{s} = 7$ TeV pp collisions with the ATLAS experiment*, *JHEP* **05** (2012) 128 [arXiv:1203.4606] [INSPIRE].

[41] ATLAS collaboration, *ATLAS Measurements of the Properties of Jets for Boosted Particle Searches*, *Phys. Rev. D* **86** (2012) 072006 [arXiv:1206.5369] [INSPIRE].

[42] ATLAS collaboration, *Measurement of the Soft-Drop Jet Mass in pp Collisions at $\sqrt{s} = 13$ TeV with the ATLAS Detector*, *Phys. Rev. Lett.* **121** (2018) 092001 [arXiv:1711.08341] [INSPIRE].

[43] ATLAS collaboration, *Measurement of the jet mass in high transverse momentum $Z(\to b\bar{b})\gamma$ production at $\sqrt{s} = 13$ TeV using the ATLAS detector*, *Phys. Lett. B* **812** (2021) 135991 [arXiv:1907.07093] [INSPIRE].

[44] ATLAS collaboration, *Measurement of soft-drop jet observables in pp collisions with the ATLAS detector at $\sqrt{s} =13$ TeV*, *Phys. Rev. D* **101** (2020) 052007 [arXiv:1912.09837] [INSPIRE].

[45] CMS collaboration, *Measurement of the differential jet production cross section with respect to jet mass and transverse momentum in dijet events from pp collisions at $\sqrt{s} = 13$ TeV*, CMS-PAS-SMP-16-010 (2017) [INSPIRE].

[46] CMS collaboration, *Measurement of jet substructure observables in $t\bar{t}$ events from proton-proton collisions at $\sqrt{s} = 13$ TeV*, *Phys. Rev. D* **98** (2018) 092014 [arXiv:1808.07340] [INSPIRE].

[47] CMS collaboration, *Measurement of the Jet Mass Distribution and Top Quark Mass in Hadronic Decays of Boosted Top Quarks in pp Collisions at $\sqrt{s} = 13$ TeV*, *Phys. Rev. Lett.* **124** (2020) 202001 [arXiv:1911.03800] [INSPIRE].

[48] CMS collaboration, *Measurement of the groomed jet mass in PbPb and pp collisions at $\sqrt{s_{NN}} = 5.02$ TeV*, *JHEP* **10** (2018) 161 [arXiv:1805.05145] [INSPIRE].

[49] ALICE collaboration, *Measurements of the groomed and ungroomed jet angularities in pp collisions at $\sqrt{s} = 5.02$ TeV*, *JHEP* **05** (2022) 061 [arXiv:2107.11303] [INSPIRE].

[50] CMS collaboration, *Study of quark and gluon jet substructure in Z+jet and dijet events from pp collisions*, *JHEP* **01** (2022) 188 [arXiv:2109.03340] [INSPIRE].

[51] ATLAS collaboration, *Measurement of jet-substructure observables in top quark, W boson and light jet production in proton-proton collisions at $\sqrt{s} = 13$ TeV with the ATLAS detector*, *JHEP* **08** (2019) 033 [arXiv:1903.02942] [INSPIRE].

[52] B. Bachu et al., *Boosted top quarks in the peak region with NL^3L resummation*, *Phys. Rev. D* **104** (2021) 014026 [arXiv:2012.12304] [INSPIRE].

[53] ATLAS collaboration, *A precise interpretation for the top quark mass parameter in ATLAS Monte Carlo simulation*, ATL-PHYS-PUB-2021-034 (2021).

[54] S. Marzani et al., *Fitting the Strong Coupling Constant with Soft-Drop Thrust*, *JHEP* **11** (2019) 179 [arXiv:1906.10504] [InSPIRE].

[55] H.S. Hannesdottir, A. Pathak, M.D. Schwartz and I.W. Stewart, *Prospects for strong coupling measurement at hadron colliders using soft-drop jet mass*, *JHEP* **04** (2023) 087 [arXiv:2210.04901] [InSPIRE].

[56] A. Kardos, A.J. Larkoski and Z. Trócsányi, *Groomed jet mass at high precision*, *Phys. Lett. B* **809** (2020) 135704 [arXiv:2002.00942] [InSPIRE].

[57] T. Sjostrand, S. Mrenna and P.Z. Skands, *A Brief Introduction to PYTHIA 8.1*, *Comput. Phys. Commun.* **178** (2008) 852 [arXiv:0710.3820] [InSPIRE].

[58] T. Gleisberg et al., *Event generation with SHERPA 1.1*, *JHEP* **02** (2009) 007 [arXiv:0811.4622] [InSPIRE].

[59] M. Bahr et al., *Herwig++ Physics and Manual*, *Eur. Phys. J. C* **58** (2008) 639 [arXiv:0803.0883] [InSPIRE].

[60] S. Marzani, L. Schunk and G. Soyez, *A study of jet mass distributions with grooming*, *JHEP* **07** (2017) 132 [arXiv:1704.02210] [InSPIRE].

[61] D. Reichelt et al., *Phenomenology of jet angularities at the LHC*, *JHEP* **03** (2022) 131 [arXiv:2112.09545] [InSPIRE].

[62] S. Marzani, L. Schunk and G. Soyez, *The jet mass distribution after Soft Drop*, *Eur. Phys. J. C* **78** (2018) 96 [arXiv:1712.05105] [InSPIRE].

[63] Y.L. Dokshitzer, G. Marchesini and B.R. Webber, *Dispersive approach to power behaved contributions in QCD hard processes*, *Nucl. Phys. B* **469** (1996) 93 [hep-ph/9512336] [InSPIRE].

[64] Y.L. Dokshitzer, A. Lucenti, G. Marchesini and G.P. Salam, *Universality of 1/Q corrections to jet-shape observables rescued*, *Nucl. Phys. B* **511** (1998) 396 [hep-ph/9707532] [InSPIRE].

[65] Y.L. Dokshitzer, A. Lucenti, G. Marchesini and G.P. Salam, *On the universality of the Milan factor for 1/Q power corrections to jet shapes*, *JHEP* **05** (1998) 003 [hep-ph/9802381] [InSPIRE].

[66] M. Dasgupta and Y. Delenda, *On the universality of hadronisation corrections to QCD jets*, *JHEP* **07** (2009) 004 [arXiv:0903.2187] [InSPIRE].

[67] M. Dasgupta and Y. Delenda, *Hadronisation corrections to jets in the k_t algorithm*, in the proceedings of the *17th International Workshop on Deep-Inelastic Scattering and Related Subjects*, Berlin, Germany, Science Wise Publ. (2009), p. 67–73 [arXiv:0906.5463] [InSPIRE].

[68] G.P. Salam and D. Wicke, *Hadron masses and power corrections to event shapes*, *JHEP* **05** (2001) 061 [hep-ph/0102343] [InSPIRE].

[69] J.C. Collins and G.F. Sterman, *Soft Partons in QCD*, *Nucl. Phys. B* **185** (1981) 172 [InSPIRE].

[70] J.C. Collins, D.E. Soper and G.F. Sterman, *Factorization for Short Distance Hadron-Hadron Scattering*, *Nucl. Phys. B* **261** (1985) 104 [InSPIRE].

[71] J.C. Collins, D.E. Soper and G.F. Sterman, *Soft Gluons and Factorization*, *Nucl. Phys. B* **308** (1988) 833 [InSPIRE].

[72] J.C. Collins, D.E. Soper and G.F. Sterman, *Factorization of Hard Processes in QCD*, *Adv. Ser. Direct. High Energy Phys.* **5** (1989) 1 [hep-ph/0409313] [InSPIRE].

[73] J. Collins, *Foundations of perturbative QCD*, Cambridge University Press (2013) [INSPIRE].

[74] C.W. Bauer, S. Fleming and M.E. Luke, *Summing Sudakov logarithms in $B \to X_s \gamma$ in effective field theory*, *Phys. Rev. D* **63** (2000) 014006 [hep-ph/0005275] [INSPIRE].

[75] C.W. Bauer, S. Fleming, D. Pirjol and I.W. Stewart, *An Effective field theory for collinear and soft gluons: Heavy to light decays*, *Phys. Rev. D* **63** (2001) 114020 [hep-ph/0011336] [INSPIRE].

[76] C.W. Bauer, D. Pirjol and I.W. Stewart, *Soft collinear factorization in effective field theory*, *Phys. Rev. D* **65** (2002) 054022 [hep-ph/0109045] [INSPIRE].

[77] C.W. Bauer and I.W. Stewart, *Invariant operators in collinear effective theory*, *Phys. Lett. B* **516** (2001) 134 [hep-ph/0107001] [INSPIRE].

[78] C.W. Bauer et al., *Hard scattering factorization from effective field theory*, *Phys. Rev. D* **66** (2002) 014017 [hep-ph/0202088] [INSPIRE].

[79] R. Abbate et al., *Thrust at N^3LL with Power Corrections and a Precision Global Fit for $\alpha_s(mZ)$*, *Phys. Rev. D* **83** (2011) 074021 [arXiv:1006.3080] [INSPIRE].

[80] R. Abbate et al., *Precision Thrust Cumulant Moments at N^3LL*, *Phys. Rev. D* **86** (2012) 094002 [arXiv:1204.5746] [INSPIRE].

[81] A.H. Hoang, D.W. Kolodrubetz, V. Mateu and I.W. Stewart, *Precise determination of α_s from the C-parameter distribution*, *Phys. Rev. D* **91** (2015) 094018 [arXiv:1501.04111] [INSPIRE].

[82] A.H. Hoang, S. Mantry, A. Pathak and I.W. Stewart, *Nonperturbative Corrections to Soft Drop Jet Mass*, *JHEP* **12** (2019) 002 [arXiv:1906.11843] [INSPIRE].

[83] A. Pathak, I.W. Stewart, V. Vaidya and L. Zoppi, *EFT for Soft Drop Double Differential Cross Section*, *JHEP* **04** (2021) 032 [arXiv:2012.15568] [INSPIRE].

[84] Y. Chen et al., *Jet energy spectrum and substructure in e^+e^- collisions at 91.2 GeV with ALEPH Archived Data*, *JHEP* **06** (2022) 008 [arXiv:2111.09914] [INSPIRE].

[85] A.J. Larkoski, I. Moult and D. Neill, *Non-Global Logarithms, Factorization, and the Soft Substructure of Jets*, *JHEP* **09** (2015) 143 [arXiv:1501.04596] [INSPIRE].

[86] K. Benkendorfer and A.J. Larkoski, *Grooming at the cusp: all-orders predictions for the transition region of jet groomers*, *JHEP* **11** (2021) 188 [arXiv:2108.02779] [INSPIRE].

[87] Z.-B. Kang et al., *The soft drop groomed jet radius at NLL*, *JHEP* **02** (2020) 054 [arXiv:1908.01783] [INSPIRE].

[88] M. Cacciari, G.P. Salam and G. Soyez, *The Catchment Area of Jets*, *JHEP* **04** (2008) 005 [arXiv:0802.1188] [INSPIRE].

[89] A.E. Ferdinand and A. Pathak, *On impact of underlying event on groomed jet mass*, (2023).

[90] P. Cal, D. Neill, F. Ringer and W.J. Waalewijn, *Calculating the angle between jet axes*, *JHEP* **04** (2020) 211 [arXiv:1911.06840] [INSPIRE].

[91] G. Bell, R. Rahn and J. Talbert, *Two-loop anomalous dimensions of generic dijet soft functions*, *Nucl. Phys. B* **936** (2018) 520 [arXiv:1805.12414] [INSPIRE].

[92] A. Ferdinand, K. Lee and A. Pathak, *Field-Theoretic Analysis of Hadronization Using Soft Drop Jet Mass*, arXiv:2301.03605 [INSPIRE].

[93] R.K. Ellis, W.J. Stirling and B.R. Webber, *QCD and collider physics*, Cambridge University Press (2011) [DOI:10.1017/CBO9780511628788] [INSPIRE].

[94] Z.-B. Kang, F. Ringer and I. Vitev, *The semi-inclusive jet function in SCET and small radius resummation for inclusive jet production*, *JHEP* **10** (2016) 125 [arXiv:1606.06732] [INSPIRE].

[95] Z.-B. Kang, K. Lee, X. Liu and F. Ringer, *The groomed and ungroomed jet mass distribution for inclusive jet production at the LHC*, *JHEP* **10** (2018) 137 [arXiv:1803.03645] [INSPIRE].

[96] P. Cal, F. Ringer and W.J. Waalewijn, *The jet shape at NLL'*, *JHEP* **05** (2019) 143 [arXiv:1901.06389] [INSPIRE].

[97] C.W. Bauer and A.V. Manohar, *Shape function effects in $B \to X_s\gamma$ and $B \to X_u\ell\bar{\nu}$ decays*, *Phys. Rev. D* **70** (2004) 034024 [hep-ph/0312109] [INSPIRE].

[98] S.W. Bosch, B.O. Lange, M. Neubert and G. Paz, *Factorization and shape function effects in inclusive B meson decays*, *Nucl. Phys. B* **699** (2004) 335 [hep-ph/0402094] [INSPIRE].

[99] M. Cacciari, G.P. Salam and G. Soyez, *The anti-k_t jet clustering algorithm*, *JHEP* **04** (2008) 063 [arXiv:0802.1189] [INSPIRE].

[100] M. Cacciari, G.P. Salam and G. Soyez, *FastJet User Manual*, *Eur. Phys. J. C* **72** (2012) 1896 [arXiv:1111.6097] [INSPIRE].

[101] A.E. Ferdinand et al., *JETlib: A C++ Package for Efficient Analyses with Monte Carlo Event Generators*, (2019).

[102] M.A. Ebert et al., *SCETlib: A C++ Package for Numerical Calculations in QCD and Soft-Collinear Effective Theory*, DESY-17-099 (2018).

[103] A. Pathak, *scetlib::sd: A C++ library for soft drop resummed observables in SCETlib*, (2022).

[104] G.P. Korchemsky and A.V. Radyushkin, *Renormalization of the Wilson Loops Beyond the Leading Order*, *Nucl. Phys. B* **283** (1987) 342 [INSPIRE].

[105] S. Moch, J.A.M. Vermaseren and A. Vogt, *The Three loop splitting functions in QCD: The Nonsinglet case*, *Nucl. Phys. B* **688** (2004) 101 [hep-ph/0403192] [INSPIRE].

[106] J.M. Henn, G.P. Korchemsky and B. Mistlberger, *The full four-loop cusp anomalous dimension in $\mathcal{N} = 4$ super Yang-Mills and QCD*, *JHEP* **04** (2020) 018 [arXiv:1911.10174] [INSPIRE].